Monte Carlo Simulation of Converging Laser Beams Propagating in the Skin Tissue Phantoms with Random Rough Surfaces

A Thesis

Presented to

the Faculty of the Department of Physics

East Carolina University

In Partial Fulfillment

of the Requirements for the Degree

Master of Science in Applied Physics

by

Ke Dong

June 1999

Abstract

Ke Dong MONTE CARLO SIMULATION OF CONVERGING LASER BEAMS PROPAGATING IN THE SKIN TISSUE PHANTOMS WITH RANDOM ROUGH SURFACES. (Under the co-direction of Drs. Xin-Hua Hu and Jun Qing Lu) Department of Physics, June 1998.

The purpose of this thesis is to study light propagation in highly scattering turbid media, such as biological tissues. A new method of Monte Carlo simulation is developed to numerically calculate the spatial distribution of photon density of a converging laser beam propagating in skin tissue phantoms with two-dimensional random rough surfaces. This method can be used to obtain both time-resolved and steady-state light distributions. In this thesis, we present results for light propagating in different skin tissue phantoms and study important features that uniquely related to converging beams propagating in such media. Two significant cases are studied: light propagation in a semi-infinite homogeneous tissue phantom with and without rough surfaces and in a multi-layered tissue phantom. The changes in the photon density distribution caused by different profiles of rough surface are also studied.

Monte Carlo Simulation of Converging Laser Beams Propagating in the Skin Tissue Phantoms with Randomly Rough Surfaces

by

Ke Dong

APPROVED BY:
DIRECTOR OF THESIS_____
XIN-HUA HU, Ph.D.

CO-DIRECTOR OF THESIS_____
JUN QING LU, Ph.D.

COMMITTEE MEMBER_____
JAMES M. JOYCE, Ph.D.

COMMITTEE MEMBER_____
GEORGE A. BISSINGER, Ph.D.

COMMITTEE MEMBER_____
MOHAMMAD SALEHPOUR, Ph.D.

CHAIR OF THE DEPARTMENT OF PHYSICS_____
MUMTAZ A. DINNO, Ph.D.

DEAN OF THE GRADUATE SCHOOL_____
THOMAS L. FELDBUSH, Ph.D.

Acknowledgements

First and foremost, I would like to take this opportunity to thank the physics department for their help and support throughout the course of this work.

I am indebted to my supervisors, Dr. Xin-Hua Hu and Dr. Jun Qing Lu, for the guidance and support they have provided since I started to work under their supervision, for their constant encouragement without which I would not have pursued a master's degree in applied physics. Their patience, despite my many, many questions, is greatly appreciated.

My acknowledgment is extended to Dr. Xiao-Ning Pan and Dr. Zhi Song for their invaluable advice both in research and in personality. Dr. Song's extensive help as a researcher, professor and friend was a priceless treasure in my whole life.

I am also grateful to Dr. Mumtaz Dinno, Chairperson of the Department of Physics, for sharing with me his wealth of knowledge in the area of biomedical physics. Many thanks to Dr. Bissinger, Dr. Joyce, and Dr. Salehpour for their serving on my thesis committee, reviewing this manuscript, and for making sure I met all the graduation requirements set by the department and the university. My classmates and friends in the Biomedical Laser Lab have encouraged me to go through this hard time and in this respect, I would like to express my appreciation to Yong Du, Qiyin Fang and Di Wu.

Finally, I owe my gratitude to my parents and my sister for their continuing support of my further education and to my wife Hairong Li, for her company and patience

throughout the year. Her faith in me and her selfless encouragement were more than any person could expect.

Numerical simulations were performed on the Cray T90 supercomputer through a grant from the North Carolina Supercomputing Center. Research assistantship has been provided through a research grant from the National Institute of Health (R15GM/OD55940-01).

Table of Contents

List of Tables

List of Figures

List of Symbols and Abbreviations

a……. Lateral Correlation Length of Randomly Rough Surface

δ……. Root Mean Square Height of Randomly Rough Surface

fs…… Femtosecond

g.…… Asymmetry Factor

LCG…… Linear Congruential Generator

LFG…… Lagged Fibonacci Generator

μm……. Micrometer

μ_a……... Absorption Coefficient

μ_s……... Scattering Coefficient

R…..……... Reflectance

RND.……. Random Number

SRG…… Shift Register Generator

T……..……... Transmittance

Chapter 1: Introduction

1.1. Background

The structural inhomogeneity and random fluctuation in the optical properties have posed many difficult problems in the studies of light interaction with turbid media such as the biological soft tissues. For example, it has remained as a fundamental challenge to precisely model the light propagation and distribution in turbid medium. Investigation of these problems requires that both the absorption and scattering of the light be taken into consideration. Many attempts have been made to provide reasonably accurate, and yet feasible, models of light propagation in turbid media. Among these, the radiative transport theory [Chandrasekhar, 1950] has served as the framework for many theoretical investigations. In this approach, the light or radiation is treated as a collection of classical particles without wave characterization, i.e., photons without optical phase and polarization. The neglect of the diffraction in the light field by the radiative transfer theory is justified by the fact that nearly all photons are multiply scattered and the coherence among the photons is quickly reduced to zero once entered into the media. Thereby the wave features of the light bears no importance in its propagation which is dominated by its energy transport aspect.

Within the framework of the radiative transfer theory, the photons undergo absorption and scattering processes in the biological tissues. Only in a few cases of simple geometry, however, can analytical solutions be obtained. Rather, numerical methods have to be resorted to in solving the radiative transport problems with practical boundary conditions.

A simple and effective approach to the radiative transfer problems can be realized using a statistical approach with Monte Carlo methods. The common feature of the Monte Carlo methods is the modeling of the absorption and scattering of photons in a turbid medium as random events whose statistical distributions are determined in the state space of a pre-constructed stochastic process.

1.2. The Goal and Significance of the Thesis Research

In many cases, such as the study of the effects of rough interfaces and propagation of converging laser beams, the algorithms adopted in the previous methods [Wilson *et al.*, 1983; Keijzer *et al.*, 1987; Wang *et al.*, 1997] loses its computational efficiency because of the requirements of the same boundary conditions for all photons injected at the boundary. No studies have been published on the effect of rough interfaces, such as those between the free-space and skin tissue and the epidermis-dermis junction in the skin tissue, on the measurement of optical properties of soft tissues and light distribution inside the skin dermis. Furthermore, recent research on treatment of skin lesions in the dermal layer with tightly focused laser beam of nanosecond pulses has pointed out the possibility of improving the current laser procedures with reduced collateral damage and compact laser systems.[Hu, 1995]

To answer these important questions, we set out to develop a new Monte Carlo method through this thesis research for efficient calculation of the light distribution of a converging laser beam in skin tissue phantoms which are closely related to realistic tissue conditions. Results obtained through these studies provide significant insights into light propagation through soft tissues which strongly scatter the light. For the first time, to the

best of our knowledge, we have numerically investigated the effects of the rough surface between free space and skin on the distribution of photon density in skin tissue phantoms using our new Monte Carlo method. We also studied the dependence of the light distribution for a converging laser beam in the skin tissue phantom on the bulk scattering coefficient and on the roughness of the boundary between the free space and tissue.

1.3. The Scope of the Thesis Research

The research project described in this thesis can be divided into two stages: the development of a new Monte Carlo method using the time-slicing technique and the study of the effect of the randomly rough interfaces on light propagation inside the skin tissue phantom. In the first stage a numerically efficient Monte Carlo simulation program of the photon migration is designed and implemented in FORTRAN codes for studies of light propagation with the non-uniform boundary condition. The Monte Carlo code was further developed in the second stage to investigate the effect of randomly rough interfaces on the light propagation inside the tissue phantom.

Chapter 2 provides the background information on the radiative transfer theory which forms the foundation of the Monte Carlo model. It also includes the description of the new Monte Carlo method and generation of randomly rough surfaces. Chapter 3 deals with the biological aspect of this research project by looking at the characteristic parameters of human skin tissues for our modeling. The algorithm development is included in Chapter 4 which also compares the performance of different random number generators used in the Monte Carlo simulation. Chapter 5 presents the numerical

simulation results and their implications. We discuss and summarize the numerical results in Chapter 6.

Chapter 2: Modeling of Light Propagation in Soft Tissues

Light (electromagnetic waves in general) interaction with condensed matter can be treated as wave based on the Maxwell's equations. This approach, however, encounters fundamental difficulties when applied to condensed media whose responses are of random nature in both space and time, such as the biological soft tissues. Furthermore, when the linear size of the biological cells in the soft tissues are comparable to the light wavelength, substantial elastic scattering may occur that need to be accounted for in any realistic models. In these cases, the radiative transfer theory often serves as a feasible framework that can be used to understand the light propagation in biological tissue. In this chapter we will first introduce the radiative transfer theory as the framework within which other the principle and other aspects of Monte Carlo simulation will be discussed.

2.1. Radiative Transfer Theory

In radiative transfer theory, the light, or photons, is treated as classical particles and the polarization and phase are neglected. This theory is described by an equation of energy transfer which can be expressed in a simple form [Chandrasekhar, 1950],

$$\frac{dI}{ds} = -\mu_t I + \mu_t \Im \qquad (2.1.1)$$

where I is the light radiance in the unit of $\frac{W}{m^2 \cdot steradian}$, $\frac{dI}{ds} = \vec{s} \cdot \vec{\nabla} I(\vec{r}, \vec{s})$, μ_t is the attenuation coefficient defined as the sum of the absorption coefficient μ_a and scattering coefficient μ_s, $\Im$ is a "source" function. The vector $\vec{r}$ represents the position and the unit

vector $\vec{s}$ the direction of a light energy quantum or photon. In highly scattering (or turbid) and source-free medium, such as the laser beam propagating in skin tissues, the source function $\Im$ can be written as:

$$\Im(\vec{r},\vec{s}) = \frac{1}{4\pi}\int_{4\pi}\Phi(\vec{s},\vec{s}')I(\vec{r},\vec{s}')d\Omega'. \qquad (2.1.3)$$

The phase function $\Phi(\vec{s},\vec{s}')$ describes the probability of light being scattered from the $\vec{s}'$ into the $\vec{s}$ direction and $d\Omega'$ denotes the element of solid angle in the $\vec{s}'$ direction. Then the equation of transfer becomes:

$$\vec{s}\cdot\vec{\nabla}I(\vec{r},\vec{s}) = -\mu_t I(\vec{r},\vec{s}) + \frac{\mu_t}{4\pi}\int_{4\pi}\Phi(\vec{s},\vec{s}')I(\vec{r},\vec{s}')d\Omega' \quad . \qquad (2.1.4)$$

If the scattering is symmetric about the direction of the incoming photon, the phase function will only be a function of the scattering angle θ between $\vec{s}'$ and $\vec{s}$, i.e., $\Phi(\vec{s},\vec{s}') = \Phi(\theta)$. A widely used form of the phase function was proposed by Henyey and Greenstein [Henyey *et al*, 1941], defined as,

$$\Phi(\theta) = \frac{\gamma(1-g^2)}{(1+g^2-2g\cos\theta)^{\frac{3}{2}}} \qquad (2.1.5)$$

where γ is the spherical albedo and g is the asymmetry factor. Their expressions are listed as follows

$$g = \frac{1}{4\pi\gamma}\int_{4\pi}\Phi(\theta)\cos\theta d\Omega' \qquad (2.1.6)$$

$$\gamma = \frac{1}{4\pi}\int_{4\pi}\Phi(\vec{s},\vec{s}')d\Omega' \qquad (2.1.7)$$

$$= \frac{\mu_s}{\mu_t} \tag{2.1.8}$$

The phase function is often normalized to describe the angular distribution of scattering probability, thus the phase function is represented by a new normalized function $p(\vec{s}, \vec{s}')$:

$$p(\theta) = \frac{\Phi(\theta)}{4\pi\gamma} = \frac{(1-g^2)}{4\pi(1+g^2-2g\cos\theta)^{\frac{3}{2}}} \tag{2.1.9}$$

$$\int_{4\pi} p(\vec{s}, \vec{s}')d\Omega' = 1 \tag{2.1.10}$$

Assuming that the scattering and absorbing centers are uniformly distributed in tissue and considering only elastic scattering, the radiance distribution in soft tissues may be divided into two parts, the scattered radiance I_s and the unattenuated radiance I_u [Lu *et al*, 1999],

$$I(\vec{r}, \vec{s}) = I_u(\vec{r}, \vec{s}) + I_s(\vec{r}, \vec{s}) \tag{2.1.11}$$

The reduction in the unattenuated radiance, i.e., the portion of the incident radiation which has never been scattered nor absorbed, is described by:

$$\frac{dI_u(\vec{r}, \vec{s})}{ds} = -\mu_t I_u(\vec{r}, \vec{s}) \tag{2.1.12}$$

Therefore, the scattered radiance in a turbid medium can be obtained through

$$\vec{s} \cdot \nabla I_s(\vec{r}, \vec{s}) = -\mu_t I_s(\vec{r}, \vec{s}) + \mu_s \int_{4\pi} p(\vec{s}, \vec{s}') I_s(\vec{r}, \vec{s}')d\Omega' + \mu_s \int_{4\pi} p(\vec{s}, \vec{s}') I_u(\vec{r}, \vec{s}')d\Omega' \tag{2.1.13}$$

where $I_s(\vec{r},\vec{s})$ is the radiance of scattered light. The first term on the right-hand side of (2.1.13) accounts for the attenuation by absorption and scattering. The second term on the right-hand side of (2.1.13) represents the radiance contributed by photons experienced multiple scattering in the medium, while the third term describes the radiance contributed by the single scattering of photons from the unattenuated part.

In principle, it is adequate to analyze the light propagation in turbid medium though (2.1.1)-(2.1.13) with proper boundary conditions. However, the general solutions are not available for the radiative transfer equation. Only a few analytical results have been obtained for cases of very simple boundary conditions. In many others, numerical methods have to be resorted to solve radiative transfer problems. Among these, the Monte Carlo simulation provides a simple and yet widely applicable approach to solve this type of problems.

Using a random walk model [Guttorp, 1995], the Monte Carlo simulation offers nearly exact solutions to three-dimensional (3-d) problems of radiative transport of arbitrary boundary conditions. Thus, it has significant advantages over other approximate methods to solve directly the radiative transfer equation such as the diffusion approximation of the radiative transport equation [Johnson, 1970; Ishimaru, 1978] and the more approximate Kubelka-Munk two flux theory [Wan *et al*, 1981]. The most important feature of the Monte Carlo simulation lies in its simple model of random walk that enables the method to be applied to problems with virtually any boundary conditions. In the past, the heavy demand of computation time of the Monte Carlo simulation to reduce statistical errors has hindered the wide applications of Monte Carlo method. With recent advent of

personal and other computers with high computation power, it appears that we are finally approaching to the threshold that the capacity of Monte Carlo simulation can be fully appreciated with a reasonable time frame and modest cost.

2.2. Monte Carlo Simulation -- Previous Methods

The efforts of applying statistical methods to solve mathematical and physical problems can be traced back to the 18^{th} century. In 1777, Comte de Buffon, a French mathematician, presented an experimental solution of a problem that is later Buffon's needle problem [de Buffon, 1777]. He successfully determined the value of π by throwing a needle onto a horizontal plane with ruled grid. Thereafter, Laplace, Rayleigh and Kelvin made advances to lay the foundation of Monte Carlo theory [de Laplace, M. P., 1886; Rayleigh, 1899; Kelvin, 1901].

In the 1930's, Enrico Fermi estimated the moderation of neutrons with adding machines. These numerical experiments have been acknowledged to be the first Monte Carlo calculations [Ostle *et al*, 1945; Kalos, 1986]. The great improvement of Monte Carlo Method may be partially attributed to the effort of several scientists, such as J. von Neumann, N. Metropolis and S. Ulam through the Manhattan project during the World War II. [Ulam, *et al*, 1947; Metropolis, 1949]. They soon realized the importance of the digital computer in the implementation of the Monte Carlo Method and their collaboration were mainly conducted in ENIAC, the first digital computer made up of 18,000 vacuum tubes; [Metropolis, 1987].

For a long time, the Monte Carlo method has been used to study the nucleons and other elementary particles propagating in various media [Forster, 1983]. In 1983, Wilson and

Adam first introduced Monte Carlo Simulation into the field of laser-tissue interactions to study the steady-state light distribution in biological tissues [Wilson *et al*, 1983]. Their remarkable works were conducted on a PDP 11/34 minicomputer. Since then, the Monte Carlo simulation has acquired considerable attention in the studies of interaction between the visible or near-infrared light and the biological tissues over the past decades. [Keijzer *et al*, 1989; van Gemert *et al.*, 1989; Schmitt *et al.*, 1990; Miller *et al.*, 1993; Wang *et al*, 1995; Garner *et al*, 1996; Wang *et al*, 1997]

Two distinctly different types of results in Monte Carlo simulation can be obtained in solving a general problem of radiation dosimetry in tissues. The first type of results relates to the distribution of the radiation energy deposited in the tissue that are most often needed in research such as the study of photodynamic therapy. Here the energy absorbed by the tissue is of primary concern. In other cases one may be interested in the second type of results that provide the spatial distribution of light, such as a laser beam, propagating in or through the tissue. These results are needed, for example, when considering the delivery of laser radiation inside the tissue for either diagnostic or therapeutic purposes.

Previous Monte Carlo simulations of the light-tissue interaction have provided mostly the energy distribution in a medium by absorption of light instead of the light distribution itself. Furthermore, only collimated or loosely focused beams in these studies. A method of spatial impulse-convolution has been adopted to enhance the computational efficiency [Keijzer, 1989; Wang *et al*, 1997]. The paths of photons contained in a spatial impulse beam, i,e, beam with “zero” diameter, are first followed individually until all the photons

are absorbed and the corresponding spatial distribution of the absorption events is recorded. On the grounds that all elements of a collimated beam of finite diameter have the same incident directions, only the trajectory of a small group of photons incident at one location of the tissue boundary need to be tracked. Then by the means of convolution integration, the spatial distribution of the absorbed light energy can be obtained for a collimated beam of arbitrary intensity distribution at the boundary.

Most photons experience multiple scattering when they propagate in the turbid medium of biological tissues. In the Monte Carlo modeling, the beam profile at the interface determines the initial directions and surface density of photons inside the tissue. After the photons migrate into the tissue, it will be scattered by scattering centers in tissue, due to the refraction index inhomogeneity, until it is absorbed or escapes from the considered region in the tissue. The trajectory of a photon in a turbid medium consists of steps of varying length between scattering sites at different scattering angles. The average free path length between two consecutive scattering events is given by $1/\mu_s$ and the average free path length before being absorbed for all photons is given by $1/\mu_a$. Here μ_s again is the scattering coefficient and μ_a is the absorption coefficient as discussed previously.

The Monte Carlo method simulates the scattering and absorption processes by random sampling of variables, such as the free path length between two consecutive scattering events and the scattering angle, from certain probability distribution functions (PDF) satisfying

$$\int_{-\infty}^{\infty} P(x)dx = 1 \qquad (2.2.1)$$

The probability distribution function for the free path length of scattering $P(L_s)$ can be assumed as [Keijzer, 1989]

$$P(L_s) = \mu_s e^{-\mu_s L_s} \tag{2.2.2}$$

The parameter L_s can be obtained from a uniformly distributed random number (RND) < 1 to satisfy the above equation through the following transformation:

$$L_s = -\ln(1 - RND) / \mu_s \tag{2.2.3}$$

Similarly, the total path length of a photon before absorption, L_a, is obtained from

$$L_a = -\ln(1 - RND) / \mu_a \tag{2.2.4}$$

Before a photon is injected at the boundary, its total path length L_a is determined from (2.2.4). Then the parameter L_s is determined each time before the tracked photon is allowed to travel before next scattering. Using the a Heyey-Greenstein distribution (2.1.9) as the phase function, the distribution functions of azimuthal and polar scattering angles are given by:

$$P(\cos\theta) = \frac{(1 - g^2)}{2(1 + g^2 - 2g\cos\theta)^{3/2}} \tag{2.2.5}$$

$$P(\phi) = \frac{1}{2\pi} \tag{2.2.6}$$

where ϕ is the azimuthal scattering angle ($0 \le \phi \le 2\pi$), and θ is the polar scattering angle ($0 \le \theta \le \pi$), g is the asymmetry factor given by the ensemble mean of $\cos\theta$: $g = \langle\cos\theta\rangle$.

2.3. Monte Carlo Simulation -- the New Time-Slicing Method

We consider a cylindrically symmetric problem in which a focused, monochromatic laser beam is incident on a tissue phantom from ambient medium at time t_0 with the central axis of the beam on the z-axis (Fig. 1). For simplicity, we discuss here a semi-infinite single-layer tissue model with an optically planar and smooth air-tissue interface. The tissue is assumed to be macroscopically homogeneous and occupy the half space of $z \geq 0$ with a finite region considered in the simulation. It is characterized by an index of refraction n, scattering coefficient μ_s and absorption coefficient μ_a. The air-tissue interface overlaps with the x-y plane ($z = 0$). The beam's initial configuration at t_0 is described by two parameters defined outside the tissue, the cone angle α of the light beam in the air and the distance *d* between its initial geometrical focal point before refraction and the air-tissue interface, as shown in Fig. 1. We assume that all photons are injected on the air side of the interface: $z = 0_-$. The angle with respect to the z-axis, at which a photon starts to propagate, is a function of the photon's distance ρ ($= \sqrt{x^2 + y^2}$) at the $z = 0$ plane according to specific beam profile, cone angle and the geometrical focal length before refraction. The photons experience refraction and reflection at the interface when they are transmitted through the tissue. Some of the photos are reflected back to air in accordance with Fresnel's formulae [Jackson, 1975] and will never enter the tissue bulk. The others changes their moving direction owing to refraction. The angle with respect to the z-axis of the photon at $z=0_+$, where is the starting point of its travel in tissue bulk, is yielded by the Snell's law [Jenkins *et al*, 1976]. To track the three-dimension

trajectories of photons contained in an incident beam, we have adopted a scheme similar to those previously used [Wilson *et al*, 1983; Keijzer *et al*, 1989].

The initial direction for each photon contained in the beam is first set according to its distance ρ from the z-axis and the given beam parameters. Before a photon is "released", its life-time, τ, is randomly chosen from Eq.(2.2.4) with an average value $<\tau> = 1/(v\mu_a)$, where μ_a is the absorption coefficient of the tissue, v the light speed in the tissue. Therefore, the total travel distance is predetermined to be $L_a = v\tau$. The photon then starts to propagate inside the tissue until scattered. The travel distance L_s between successive scattering events is again randomly chosen from Eq. (2.2.3). The new propagation direction of the photon in the 3-d space after the scattering is determined by two angles, θ and ϕ, with respect to the incident direction of the photon before scattering. The azimuthal angle ϕ and polar angle θ are randomly chosen from Eqs. (2.2.5) and (2.2.6) to determine the projection of the new direction in the plane perpendicular to the incident direction. Before the photon is allowed to propagate further after a scattering event, the total distance L traversed by the photon along its trajectory is calculated to test if it exceeds L_a predetermined by Eq. (2.2.4). If $L \geq L_a$, the photon is then eliminated as a result of absorption. Otherwise, the photon's position is further checked to determine if it is on the boundaries of the tracking region in the tissue. When the photon is on the air-tissue interface, it will be either internally reflected, with a probability equal to the Fresnel reflection coefficient, or eliminated for its escape into the air. The photon will also be eliminated if it travels beyond the other boundaries of the tracking region. If the photon survives these tests, it will be allowed to propagate further until one of the

eliminating conditions discussed above is met. The procedures are repeated until all the photons contained in the initial profile of the beam are depleted.

In order to obtain the light distribution inside the tissue, we use a "time-slicing" method [Song *et al*, 1999; Dong *et al*, 1999; Lu *et al*, 1999] based on the principle of discrete signal sampling [Stanley *et al*, 1984] to follow the photons in the time domain after its initial injection at t_0. In this method, the system is considered to be linear and time-invariant (LTI) because the light propagation is described by a linear differential equation with time-independent parameters. In a LTI system, if the response *g(t)* to an unit impulse *d(t)* is known, the output *G(t)* of the system to any arbitrary input signal *E(t)*, which may represent an incident laser beam, can be expressed in terms of the convolution integral of *g(t)* and *E(t)*,

$$G(t) = E(t) * g(t) = \int_{-\infty}^{\infty} E(\tau) g(t-\tau) d\tau \tag{2.3.1}$$

In the "time-slicing" method, a monochromatic laser beam is thought of as an ensemble of multiple independent photons and the process of light projection can thus be divided into a series of photon injection impulses. Since the laser beam was not incident on the tissue until $t=t_0$, Eq. (2.3.1) can be rewritten as

$$G(t) = \int_{t_0}^{\infty} E(\tau) g(t-\tau) d\tau \tag{2.3.2}$$

For numerical calculations, the above is often written in a discrete form,

$$G(t) = \sum_{k=0}^{[(t-t_0)/\Delta\tau]} E(t_0 + k\Delta\tau) g(t - t_0 - k\Delta\tau) \Delta\tau \tag{2.3.3}$$

In our simulation the injected photon number per unit time of a monochromatic laser beam at the air side of the interface z=0. (Fig. 1), is defined as the input signal *E(t)*. In order to get the temporal impulse response *g(t)*, we first consider a monochromatic laser beam of only one temporal unit impulse containing N_0 photons that is described by

$$d_{N_0}(t) = d(t) \cdot N_0 = N_0 F(\rho)\delta(t - t_0)\delta(z = 0_+) \tag{2.3.4}$$

$$2\pi \int_0^\infty F(\rho)\,\rho\, d\rho = 1 \tag{2.3.5}$$

where $F(\rho)$ provides the normalized beam profile in terms of the surface density of photon at the air-tissue interface. The initial directions of the injected photons are back-projected to the z=0 plane from a spherical wavefront of radius d centered at the focal point located on the z-axis at z=d. The considered region of the tissue is divided into a grid of cubic cells of volume b^3 with each side parallel to the *x*-, *y*- and *z*-axes. Using the scheme described above, the position of each tracked photon in the impulse along its 3-d trajectory inside the tissue is recorded according to which cell it traverses at time t_i ($i = 1, 2, \ldots m$). This sequence of time, $t_{i+1} > t_i > t_0$, separate the temporal course of the tracked photon during its lifetime into many small and equal segments which are called the "time slices". Each time slice has the same duration of $\Delta\tau = t_{i+1} - t_i = \frac{a}{v}$, where a is the travel distance of the photon which is chosen to be smaller than b and much smaller than $< L_s >$ and v is the light speed in the medium where the photon is traveling. After all the N_0 photons in the temporal impulse are tracked, the photon density per unit time at time t_i can be obtained by tallying the number of photons that traverse through the *j*th cell during

Δt, denoted as $\frac{W_j(t_i)}{b^3\Delta t}$, where Δt is the dwelling time of a photon inside a cell averaged over all N_0 photons and $W_j(t_i)$ is the number of photons in jth cell at time t_i. The function $\frac{W_j(t_i)}{b^3\Delta t}$ then provides the time evolution of the photon density per unit of time at the location of jth cell as a consequence of the initial injection given by the impulse $N_0F(\rho)\delta(t-t_0)\delta(z = 0_+)$. Therefore, the local response of the jth cell $g(t)$ to the temporal impulse is given by $\frac{W_j(t_i)}{b^3\Delta t}$. Any arbitrary input signal $E(t)$ could be conceived as the numerically equivalent of the superposition of multiple temporal impulses separated by $\Delta\tau$ with the requirement that $\Delta\tau << t$. For the input signal $E(t)$ as the injected photon number per unit time at the tissue boundary, the photon density per unit time at time t in the jth cell is thus given by

$$G_j(t) = \sum_{i=0}^{[(t-t_0)/\Delta\tau]} \frac{E(t_0 + i\Delta\tau)}{N_0} \frac{W_j(t_i - t_0 - i\Delta\tau)}{b^3\Delta t}\Delta\tau \qquad (2.3.6)$$

In (2.3.6), N_0 is used as a denominator to normalize the result for the impulse $d_{N_0}(t)$ we considered previously consisting of N_0 photons. The input $E(t)$ can also be transformed to $E(t)\hbar\omega$ as a expression of power, where $\hbar\omega$ is the photon energy. Similarly the energy flux of the jth cell can also be easily expressed as $G_j(t)\hbar\omega$. For the continuous-wave laser beam with constant power, $E(t)\hbar\omega$ equals to the power of the laser beam. It is straightforward to obtain light distributions in time-resolved forms from the set of the functions $\{W_j(t_i)\}$ according to (2.3.6).

The information embodied in $\{W_j(t_i)\}$ can also be organized in the following fashion to efficiently obtain a steady-state distribution of the photon density for a laser beam of arbitrary spatial profiles at the boundary. During the tracking of photons, the maximum slice number, m_{max}, which is the m of the longest-lived photon among all of the tracked photons, is recorded. Therefore, the steady-state distribution of light can be achieved after $m_{max}\Delta\tau$ and can be calculated as the photon density during the dwelling time Δt in the jth cell with the following time summation:

$$E_j(t) = \sum_{i=0}^{m_{max}} \frac{E(t_0 + i\Delta\tau)}{N_0} \frac{W_j(t_i - t_0 - i\Delta\tau)}{b^3 \Delta t} \Delta\tau \qquad (2.3.7)$$

Obviously, the simulation of steady-state distributions demands much less computer memory than the time-resolved simulations by not keeping the middle results $\{W_j(t_i)\}$ during the photon tracking.

We would like to point out that m_{max} varies slightly due to the random nature of the maximum lifetime τ of the tracked photons among different simulations with identical parameters. However, the probability distribution of lifetime varies in accordance with the exponential function, so the small error caused by the fluctuation of m_{max} could be neglected.

2.4. Boundary Conditions

2.4.1. Effect of Different Beam Profiles at Smooth Interfaces

In order to investigate the effect of boundary conditions, we conducted the simulations with different beam profiles. Both "Top-hat" beam and Gaussian beam were investigated. The "top-hat" beam has an ideally flat profile with a uniform photon distribution in the transverse plane while the Gaussian beam has a beam profile described by the Gaussian function, as shown in Fig. 2. In general a beam profile at the interface between ambient medium and tissue phantom can be described by a function F(x, y) at z=0.

2.4.2. Effect of Surface Roughness

Extensive research in the past decade has proved that the surfaces with roughness of same orders of magnitude as the light's wave length can significantly affect the light propagation. [Maradudin, 1990; Tran, 1992, 1993, 1994] Therefore, any serious investigations to model the light propagation in skin tissues have to take the surface roughness of skin into consideration. To the best of our knowledge, none of the previous studies has included the effect of rough surface and interfaces on light propagation in soft tissues due to the difficult boundary conditions that need to be dealt with. Therefore, we proceed to establish a rough surface model to study its effect on light distribution.

In accordance with the spatial characteristics of the human skin surface, a surface profile function $\zeta(\vec{R})$ is introduced to describe the elevation of a rough interface along the z-axis between ambient medium and tissue phantom, where $\vec{R} = (x, y)$ indicates the

Cartesian coordinate of the point at the interface. The function $\zeta(\bar{R})$ is assumed to be a stationary, Gaussian stochastic process [Maradudin, 1990; Tran, 1992, 1993, 1994]. The major effect of the surface roughness is the variation in the reflection and refraction as a result of the mismatch of refractive index and random nature of the surface normal. For a smooth interface, the normal vector of any point on the interface remains the same. However, when the roughness of the interface is taken into consideration, the normal vector of different points on the interface varies randomly, which leads to the different reflection and refraction coefficients because of the variation in the incident angle. Using Fresnel's formulae, [Jackson, 1975] we calculate the locally reflection and refraction coefficients on the medium-tissue interface once the surface normal and incident angle are determined.

Chapter 3: Modeling of the Human Skin Tissues

In this chapter we will deal with the biological aspects of modeling of light propagation in human skin tissues and the mathematical tools that are needed to investigate the effect of rough surfaces.

3.1. Human Skin Structure

Skin is considered the largest and heaviest organ of the human body. It has 16% of the total body weight and an area of 1.6 to 1.9m^2. Its functions include thermoregulation, protection, excretion, sensation, fat storage, synthesis and communication of emotions. Human skin is composed of two primary layers––epidermis and the underlying dermis. Epidermis consists of multiple surface layers that are keratinised. The dermis layer consists of the dense fibro-elastic connective tissues containing glands and hair [Anothony, *et al*, 1983].

Skin can be classified according to its epidermis thickness although epidermis is very thin compared to the total skin thickness. In average, the dermis is 3 mm thick, while the thickness of epidermis varies between 50 and 150 μm [Anderson *et al*, 1981]. The epidermis is the most superficial layer of the skin and forms the interface between skin tissue and ambient environment. Therefore, the epidermis structure determines the surface roughness of the skin tissues. The epidermis can be divided further into five sublayers from the skin surface to the inside: stratum corneum, stratum lucidum, stratum granulosum, stratum spinosum, and stratum germinativum or the stratum basale (Fig. 3). The principal cells of the epidermis are keratinocytes which gradually migrate from the

deepest stratum to the surface exposed to the ambient environment and is sloughed off in a process called desquamation. The desquamation period from basal to superficial ranges from 25 to 50 days [Anothony, *et al*, 1983].

The outermost sublayer of the epidermis, the stratum corneum, is composed of 15 to 20 layers of flattened, non-nucleated, keratinized cells called corneocytes which are filled with filaments of keratin. These cells are dead, dehydrated and flat. The roughness of the skin surface is mainly determined by the stratum corneum. The thickness of this sublayer is approximately 10μm [Anderson *et al*, 1981], which implies that the average size of the dead cells in the direction normal to the skin surface is roughly 1 μm. The lateral cell diameters range from 40 to 50μm [Fig. 4 and Fig. 5]. Since the corneocytes are arranged in vertical columns that resemble stacks of pie plates [Moschella *et al*, 1992], the fluctuation of surface height is expected to be about the cell thickness in the normal direction or about 1 μm. The average peak-valley distance in the surface plane of the skin tissue is expected to be similar to the lateral cell diameters near 50 μm.

3.2. Modeling of the Skin Surface

In order to model the effect of the surface roughness on light propagation, we employed a statistical technique to simulate the random surface with a stochastic process. A stochastic process means one process in which a sequence of values is drawn from a corresponding sequence of jointly distributed random variables. The method of generating a rough surface has been used to study the multiple scattering of

electromagnetic waves from random rough surfaces [Garcia *et al*, 1984; Maradudin *et al*, 1990; Tran *et al*, 1992, 1993, 1994]. In our model, results from individual realizations of rough surfaces are averaged to obtain the statistical properties of skin surface.

Before getting into the detail of modeling, some background knowledge will be necessary. A stochastic process, which is also called a random process, is a collection of random variables $\{A(\alpha), \alpha \in T\}$, indexed by a parameter α taking values in the parameter set T. The random variables, $A(\alpha)$, take values in a set S which is called the state space of the stochastic process [Kulkarni 1995]. Among all the random processes, the wide sense stationary (WSS) process is most often used to model practical random phenomena for its simplicity. If we denote $C(m,n)= \langle X_m X_n \rangle$ as the correlation between two variables X_m and X_n in a stochastic process, the WSS processes can be defined as the process satisfying the following two conditions. First, the mean value $\langle X_n \rangle$ must be independent of n. Secondly the correlation of the set elements X_n, C(m,n), depends only on the difference m-n. In WSS process, C(n,n-k) is defined as the autocorrelation sequence $C_X(k) = \langle X_n X_{n-k} \rangle$. A stationary, Gaussian process means that the random variables in a stationary process follow a Gaussian (normal) distribution [Dym, 1976; Kendall *et al*, 1987].

The stochastical modeling of the skin tissue surface adopted in this research project employs an ensemble of randomly rough surfaces. The rough skin surface is described by an elevation function $\zeta(\vec{R})$ which forms the interface between the ambient medium, such as air or water, and the skin tissues, which are assumed to be macroscopically homogeneous. The function $\vec{R} = (x, y)$ is defined to be the Cartesian coordinates of a

point at the interface. Thereby, the probability distribution function (PDF) of the surface elevations $\zeta(\vec{R})$ at any single point is a Gaussian function which is required to possess the following properties

$$< \zeta(\vec{R}) >= 0 , \tag{3.2.1}$$

$$< \zeta(\vec{R})\zeta(\vec{R}^{'}) >= \delta^2 W(\left|\vec{R} - \vec{R}^{'}\right|) = \delta^2 \exp[-(\vec{R} - \vec{R}^{'})^2 / a^2] \tag{3.2.2}$$

where the angle brackets denote an average over the ensemble of realizations of the surface profile. The Gaussian PDF $W(|\vec{x}|)$ contains two parameters: δ is the rms height of the interface indicating the vertical fluctuation of the interface and a is the lateral correlation length of the surface roughness describing the average lateral distance between the peak and valley in the surface profile. The ratio δ/a represents the average slope of the surface fluctuations and remains much smaller than 1 in our model which is consistent with previously described surface profiles of human skin.

Since $\zeta(\vec{R})$ is assumed to be a stationary, Gaussian process and usually only uniform random number generators are provided in computer codes, we are not able to generate the random variables of Gaussian distribution directly in the codes. Thus, we first introduce an uncorrelated Gaussian distribution function $X(\vec{R})$ indexed by the position vector $\vec{R}$, and $X(\vec{R})$ has zero mean value as well as a standard deviation described by the Dirac δ-function:

$$< X(\vec{R}) >= 0 \tag{3.2.3}$$

$$< X(\vec{R})X(\vec{R}') >= \delta(\vec{R} - \vec{R}') \quad . \tag{3.2.4}$$

To obtain a Gaussian correlated function $\zeta(\vec{R})$ required in Eq. (3.2.2), the function $X(\vec{R})$ is transformed into a Gaussian distribution function $G(\vec{R}) = \delta(\frac{a^2}{16\pi})^{-\frac{N}{4}} e^{-\frac{2\vec{R}^2}{a^2}}$ though a convolution integration:

$$\zeta(\vec{R}) = X(\vec{R}) * G(\vec{R}) = (2\pi)^{-\frac{N}{2}} \delta(\frac{a^2}{16\pi})^{-\frac{N}{4}} \int_{-\infty}^{\infty} X(\vec{R}') e^{-\frac{2(\vec{R}-\vec{R}')^2}{a^2}} d\vec{R}' \qquad (3.2.5)$$

where N is the number of dimension of the vector $\vec{R}$. Although the equations from (3.2.1) to (3.2.5) are sufficient to obtain $\zeta(\vec{R})$, it is much more efficient numerically to accomplish the above procedures in the frequency domain with the Fast Fourier Transform. For this purpose, two new functions are introduced to represent the inverse Fourier transforms of $X(\vec{R})$ and $G(\vec{R})$ respectively.

$$x(\vec{Q}) = \frac{1}{(2\pi)^{\frac{N}{2}}} \int d\vec{R} \cdot e^{-i\vec{Q}\vec{R}} X(\vec{R}) \qquad (3.2.6)$$

$$g(|\vec{Q}|) = \frac{1}{(2\pi)^{\frac{N}{2}}} \int d\vec{R} \cdot e^{-i\vec{Q}\vec{R}} G(\vec{R}) = \delta(a^2\pi)^{\frac{N}{4}} e^{-\frac{a^2\vec{Q}^2}{8}} \qquad (3.2.7)$$

Thus, $\zeta(\vec{R})$ can be calculated as the following

$$\zeta(\vec{R}) = \frac{1}{(2\pi)^{\frac{N}{2}}} \int g(\vec{Q}) \cdot x(\vec{Q}) \cdot e^{i\vec{Q}\vec{R}} d\vec{Q} \qquad (3.2.8)$$

Since $\vec{R}$ is a two-dimensional vector in our case and insert Eq. (3.2.7) into Eq. (3.2.8), we obtain

$$\zeta(\vec{R}) = \frac{\delta a\sqrt{\pi}}{2\pi} \int e^{-\frac{a^2\vec{Q}^2}{8}} \cdot x(\vec{Q}) \cdot e^{i\vec{Q}\vec{R}} d\vec{Q} \qquad (3.2.9)$$

for the surface elevations at location $\vec{R}$ once the Fourier components of random Gaussian distribution function $X(\vec{R})$ are determined.

3.3. Rough Surface Generation

In numerical calculations, $\zeta(\vec{R})$, $X(\vec{R})$ and $G(\vec{R})$ are treated as functions of discrete serie of points: $\alpha_k=k\Delta x$, $\beta_l=l\Delta y$ where k, l =0, ±1, ±2, … for x, y coordinates, respectively. The function $X(\vec{R})$ is expressed as the following according to our earlier discussion,

$$< X_{i,j} >= 0 \qquad (3.3.1)$$

$$< X_{i,j} X_{i',j'} >= \delta_{ii',jj'} \qquad (3.3.2)$$

where $\delta_{ii',jj'}$=1, (if i=i' and j=j'); otherwise, $\delta_{ii',jj'}$=0.

In order to implement Fast Fourier Transform in a computer, $<\zeta(\alpha_k,\beta_l)>$ is assumed to be a perodic function of k and l with period 2M and 2N, $<\zeta(\alpha_k,\beta_l)>$ = $<\zeta(\alpha_{k+2M},\beta_l)>=<\zeta(\alpha_k,\beta_{l+2N})>$, where 2M and 2N are large integers. We can obtain a representation of $<\zeta(\alpha_k,\beta_l)>$ with this property by requiring that $G(\alpha_k,\beta_l)$ and $X_{i,j}$ also possess this periodicity, and Eqs. (3.2.6) and (3.2.7) can be written as

$$g(q_{1i},q_{2j}) = \frac{1}{2\sqrt{MN\Delta x\Delta y}} \sum_{l=-N}^{N-1} \sum_{k=-M}^{M-1} G(\alpha_k,\beta_l) \exp[I2\pi(q_{1i}\alpha_k + q_{2j}\beta_l)] \qquad (3.3.3)$$

$$x_{ij} = \frac{1}{2\sqrt{MN}} \sum_{l=-N}^{N-1} \sum_{k=-M}^{M-1} X_{kl} \exp[\, I2\pi(\frac{ki}{2M} + \frac{lj}{2N})] \qquad (3.3.4)$$

where $I = \sqrt{-1}$. In the limit as M, N$\rightarrow\infty$, we have Δx, $\Delta y \rightarrow 0$, if $\lambda_1 = 2M\Delta x$, $\lambda_2 = 2N\Delta y$, and $q_{1i} = 2\pi i/\lambda_1$, $q_{2j} = 2\pi j/\lambda_2$ remain constants. Therefore, $g(q_{1i}, q_{2j})$ can be obtained as

$$g(q_{1i}, q_{2j}) = \delta(a^2\pi)^{\frac{1}{2}} e^{-\frac{a^2(q_{1i}^2+q_{2j}^2)}{8}}. \qquad (3.3.5)$$

It follows that

$$\zeta(\alpha_k, \beta_l) = \frac{1}{2\sqrt{MN\Delta x\Delta y}} \sum_{i=-M}^{+M} \sum_{j=-N}^{+N} x_{i,j}\, g(\sqrt{q_{1i}^2 + q_{2j}^2}) \exp[I(q_{1i}\alpha_k + q_{2j}\beta_l)]. \qquad (3.3.6)$$

According to Eq. (3.3.5), we thus get

$$\zeta(\alpha_k, \beta_l) = \frac{\delta}{2\sqrt{MN\Delta x\Delta y}} \sum_{i=-M}^{+M} \sum_{j=-N}^{+N} x_{i,j}\, a\sqrt{\pi} \exp[-\frac{a^2(q_{1i}^2 + q_{2j}^2)}{8}] \exp[I(q_{1i}\alpha_k + q_{2j}\beta_l)] \qquad (3.3.7)$$

Since Eq. (3.3.7) is equivalent to (3.2.9) only when M, N$\rightarrow\infty$, the result yielded by Eq. (3.3.7) may be different from those given by Eq. (3.2.9) which is called an edge effect. However, if M, N are chosen to be larger than the sample size this edge effect can be reduced. As a result, we always cut the inner center square of a large surface generated by the codes as the surface sample.

To calculate the surface normal, we obtain the partial derivatives of the surface elevation function at ($x=\alpha_k$, $y=\beta_l$) by taking differentiation of the Eq. (3.3.7) with respect to α_k, β_l.

$$\zeta_x'(\alpha_k, \beta_l) = \frac{\delta}{2\sqrt{MN\Delta x\Delta y}} \sum_{i=-M}^{+M} \sum_{j=-N}^{+N} x_{i,j}\, g(\sqrt{q_{1k}^2 + q_{2l}^2}) I q_{1k} \exp[I(q_{1k}\alpha_k + q_{2l}\beta_l)]$$

(3.3.8)

$$\zeta_y'(\alpha_k,\beta_l)=\frac{\delta}{2\sqrt{MN\Delta x\Delta y}}\sum_{i=-M}^{+M}\sum_{j=-N}^{+N}x_{i,j}g(\sqrt{q_{1k}^2+q_{2l}^2})Iq_{2l}\exp[I(q_{1k}\alpha_k+q_{2l}\beta_l)]$$

(3.3.9)

The normal vector, pointing outward from the skin tissue phantom, at any point on the skin surface is then given by:

$$\hat{n}=\frac{(-\zeta_x'\hat{x}-\zeta_y'\hat{y}+\hat{z})}{\sqrt{\zeta_x'^2+\zeta_y'^2+1}} \qquad (3.3.10)$$

where $\hat{x},\hat{y}$ and $\hat{z}$ are the unit vectors along respective axes. The information on the surface normal vector $\hat{n}$ will be used in photon tracking when photons reflect or refract from a location on the rough surface. An example of a rough surface generated in the above approach is displayed in Fig. 6 with the sample size given by 1.0mmx1.0mm. The cross-section view is also manifested by Fig. 7. We verified the auto-correlation of the surface sample, a dashed curve in Fig. 8 represents the result as the ratio of auto-correlation to the mean square height δ^2 versus the ratio of distance to the lateral correlation length a. Another curve of the Gaussian distribution is plotted in Fig. 5 for reference. In comparison with the curve of the Gaussian distribution, it turns out our result is consistent with the Gaussian distribution as expected.

3.4. The Two-layer Model of Human Skin Tissue

The epidermis and dermis layers in the human skin can be further divided into many sublayers according to their physiology conditions. We start by considering a two-layer

model in this research project as the first step toward developing a realistic model of human skin to study light propagation. In this model, the epidermis and dermis layers are assumed to be infinite in the transverse x-y plane. The optical properties of each layer is described its own refractive index n, the absorption coefficient μ_a, the scattering coefficient μ_s, and the asymmetry factor g. The epidermis-dermis junction is simulated in the same fashion as a rough surface similar to the ambient medium-tissue interface with a different surface elevation function.

The geometry of the two-layer model is mainly depicted by the following parameters: layer thickness, the rms height δ and the lateral correlation length *a* for the two randomly rough surfaces which represent the interfaces of the epidermis layer with the ambient medium and with the dermis layer. The dominant absorber to the near-infrared light at wavelengths near 1 μm in the epidermis is melanin and we choose $\mu_s = 6.0\ mm^{-1}$, $\mu_a = 5.0\ mm^{-1}$ and g = 0.9 [Schmitt *et al*, 1990]. In the dermis layer the principal absorber is hemoglobin which absorbs the near-infrared light weakly. Therefore, the bulk absorption coefficient of the dermis is chosen to be smaller than that of the epidermis: $\mu_s = 4.0\ mm^{-1}$, $\mu_a = 0.5\ mm^{-1}$ and g = 0.9 [Schmitt *et al*, 1990].

Similar to the medium-epidermis interface, the epidermis-dermis junction is also treated as a rough surface with the surface elevation and lateral correlation length given by those of the epidermis-dermis junction, larger than the air-epidermis interface. Referring to the data cited in §3.1, we choose the thickness of the epidermis to be 100μm, rms height δ of the medium-epidermis interface to be near 1 μm and lateral correlation

length *a* to be 10 μm. For the epidermis-dermis interface, we set δ to be 20 μm and *a* to be 30μm according to the cross-section EM photograph in Fig. 9 [Marchesini, 1992].

3.5. Photon Refraction and Reflection at the Interfaces

Reflection and transmission will occur when light is incident on an interface between the ambient medium and tissue or different tissue layers. In our model, we treat these phenomenon locally with the Fresnel's formulation [Jackson, 1975] averaged in both polarization directions for the incident photons. Assuming the refractive indices of the ambient medium and the tissue as n_1 and n_2, respectively, the relationship between the angle of incidence ϕ_1, the angle of transmission ϕ_2 given by the Snell's law [Jenkins, 1976]:

$$n_1 \sin\phi_1 = n_2 \sin\phi_2 , \qquad (3.5.1)$$

and the reflectance R and transmittance T can be written as:

$$R = \frac{1}{2}\left[\left\{\frac{\tan(\phi_1-\phi_2)}{\tan(\phi_1+\phi_2)}\right\}^2 + \left\{\frac{\sin(\phi_1-\phi_2)}{\sin(\phi_1+\phi_2)}\right\}^2\right] \quad (\text{when } \phi_1 \neq 0) \qquad (3.5.2)$$

$$R = \left(\frac{n_2-n_1}{n_2+n_1}\right)^2 \qquad (\text{when } \phi_1 = 0) \qquad (3.5.3)$$

$$T = 1 - R . \qquad (3.5.4)$$

For smooth and flat surface the surface normal vector remains the same at all locations. It is fairly straightforward to calculate the probability for photon to be either reflected or refracted, using the Fresnel coefficients given in Eqs. (3.5.2) and (3.5.4), once the photon

travel direction is known. For rough surfaces, however, the direction of the surface normal depends on the location at the surface. Both the photon direction and the surface normal direction are required to calculate the incident angle to obtain the reflection and transmission coefficients.

Since we know the incident unit vector $\hat{i}$ and the normal unit vector $\hat{n}$ from Eq. (3.3.10), which is defined to point from interface toward ambient medium, the unit vector of the reflected ray $\hat{r}$ and the unit vector of the refracted ray $\hat{t}$ can be obtained from the following simple geometry shown in Fig. 10.

The relations between $\hat{i}$, $\hat{n}$, $\hat{r}$, $\hat{t}$ are given by

$$\hat{r} = \alpha\hat{n} + \hat{i} \tag{3.5.5}$$

$$\hat{t} = -\beta\hat{n} + \gamma\hat{i} \tag{3.5.6}$$

where α, β, γ are positive constants. Using the proportional relations between the sine functions of the angles and the side lengths of a triangle, we can obtain from the above equations:

$$\frac{\sin\phi_1}{1} = \frac{\sin(\pi - 2\phi_1)}{|\alpha|} \ , \tag{3.5.7}$$

$$\frac{\sin\phi_2}{|\gamma|} = \frac{\sin(\phi_1 - \phi_2)}{|\beta|} = \frac{\sin(\pi - \phi_1)}{1} \ . \tag{3.5.8}$$

It follows that

$$\alpha = 2\cos\phi_1 , \tag{3.5.9}$$

$$\beta = \frac{\sin(\phi_1 - \phi_2)}{\sin\phi_1} , \tag{3.5.10}$$

$$\gamma = \frac{\sin\phi_2}{\sin\phi_1} = \frac{n_1}{n_2}. \tag{3.5.11}$$

From Eqs. (3.5.9)-(3.5.11), we conclude that,

$$\hat{r} = 2\cos\phi_1\hat{n} + \hat{i}, \tag{3.5.12}$$

$$\hat{t} = \frac{\sin(\phi_2 - \phi_1)}{\sin\phi_1}\hat{n} + \frac{n_1}{n_2}\hat{i}, \tag{3.5.13}$$

Therefore, with the help of equations from (3.5.1) to (3.5.13), we can calculate the reflectance and transmittance at any point of the medium-tissue boundary once the surface normal and photon direction are determined. In implementing the photon reflection and transmission in our codes, when the photon reaches to the interface a uniformly distributed random number RND ($0 \le RND \le 1$) is generated to determine the fate of the photon. If RND is smaller than the reflectance R, the photon will be reflected. Otherwise it will transmit though the interface.

When the photon transmits through an interface, it will either be counted as escape into the free space or migrate into the neighboring tissue layer with different μ_s, μ_a and g. If the photon escapes into the free space, we will not trace it any longer because no scattering is assumed there. If it goes into the neighbor layer, we convert its remaining trajectory using the following equations:

$$L_{s2} = \frac{L_{s1} \cdot \mu_{s2}}{\mu_{s1}} \tag{3.5.13}$$

$$L_{a2} = \frac{L_{a1} \cdot \mu_{a2}}{\mu_{a1}} \tag{3.5.14}$$

where the L_{s2}, L_{a2} are the new scattering and new absorption step sizes, L_{s1} and L_{a1} are the current scattering and absorption step sizes, μ_{s1}, μ_{a1} correspond to the scattering and absorption coefficient of the layer before tranmission and μ_{s2}, μ_{a2} are the scattering and absorption coefficient of the layer after transmission, respectively.

Chapter 4: Development of the Algorithm

We have introduced the principles and the various aspects of the Monte Carlo method to model light propagation in skin tissue phantom in Chapters 2 and 3. This chapter discusses the algorithmic details that are important to implement the previously discussed principles into the FORTRAN90 codes.

4.1. The General Structure of the New Monte Carlo Codes

To achieve satisfactory precision in the program output, all floating-point variables are of double precision. Because the large computing power required and multiple computer platforms used for these simulations, extensive efforts are made to produce highly efficient and portable source codes without commercial mathematical library subroutines. The main section of the FORTRAN codes is listed in Appendix C.

4.1.1. The Photon Density Calculation in 2-d Planes

The light distribution for a converging laser beam in a tissue phantom is calculated in terms of photon density, i.e., the photon number per unit volume in the considered region. A Cartesian coordinate system (x, y, z) is used for the calculation of the photon density distribution, as shown in Fig. 1, with z-axis as the laser beam axis. We adopt a 3-d grid in our codes in which each grid cell is a cube with sides along the x, y and z axes for photon tracking. Since the simulated problem possesses cylindrical symmetry, the light distributions in x-z, x-y planes and along the z-axis are sufficient to present simulation

results. The 2-d presentation, or the photon density in a monolayer of the 3-d grid, of the final results significantly reduces the size of the computer memory required for data storage. The following segment of the codes shows the implementation of the 2-d calculation.

```
parameter(x0=1., y0=1., z0=1.5, R0=0.2985,F=0.7092)          !semi/gauss-beam
parameter(NX=501, NY=nx, NZ=750)
integer, ALLOCATABLE, target::DEPOSIT(:,:)
!Deposit() is a two-dimensional array at y=0 plane.
      integer, pointer::pDeposit(:,:)
ALLOCATE(DEPOSIT(1:NX,1:NZ))
pDeposit=>Deposit(1:NX,1:NZ)
do I=-10,NZ,1
do J=1,NX,1
deposit(J,I)=0
enddo
enddo
```

The real-type 2-d array DEPOSIT is mapped to one monolayer of the 3-d grid in the tissue phantom in the x-z lane at y = 0. Each element in the DEPOSIT array is a counter to count the photon number within the corresponding grid cell. The parameters x0, y0, and z0 are used to define the size of the 3-d grid in millimeters and NX, NY, NZ are the number of grid cells along each axis, respectively. It is easy to recognize from the values of the above parameters that each grid cell is a cube with 2μm side. The elements in DEPOSIT is accessed by indices NI and NJ, which are related to the Cartesian coordinates of photons:

$$NI = ROUND(x \cdot x0/(NX-1)) + [(NX+1)/2] \qquad (4.1.1)$$

$$NJ = [z \cdot z0/(NZ-1)] \qquad (4.1.2)$$

where x and z are the coordinates of a photon and [ ] takes the integral part of a number.

Before starting to count the photon density, the y coordinate of the photon along its 3-d trajectory is checked to ensure that the photon is dwelling in the considered monolayer at

y = 0 during a time of photon counting (see discussion on time-slicing method in Chapter 2). If $-1\mu m < y < 1\mu m$, the photon will be added to the corresponding counter in DEPOSIT for density calculation. Otherwise, the program ignores the coordinate information. For instance, if a photon is at the position (0.5μm, 0 μm, 0.5μm) during the time of photon counting, the element, DEPOSIT(251, 375), will be increased by 1. Instead, if the photon is at a position (0.5μm, 5μm, 0.5μm) where is out of the defined region then the program will not change the DEPOSIT element.

A "time-slicing" method is used to directly record the spatial distribution of photon density inside the tissue phantom. In order to obtain the steady-state light distribution, we record every photon's temporal trajectory as well as the longest trajectory of photons injected into the tissue. A subroutine called snap_shot() is used for this purpose:

```
subroutine snap_shot(p_Photon,p_Bulk, p_layer, pDeposit)
implicit real(8) (a-h, o-z)
real(8) x,y,z,oy
integer(4), pointer::pDeposit(:,:)
logical(1) l_nshot
type(PhotonStruct), pointer:: p_Photon
type(BulkStruct), pointer:: p_Bulk
type(LayerStruct), pointer:: p_Layer
common/const/Pi,zero_p,one_m,hPis,coszero,cos90d
x=p_Photon%x
y=p_Photon%y
z=p_Photon%z
ux=p_Photon%ouN(1)
uy=p_Photon%ouN(2)
uz=p_Photon%ouN(3)
ox=p_Photon%ox
oy=p_Photon%oy
oz=p_Photon%oz
ols=p_Photon%ols
lshot=p_Photon%lshot
fnx=p_Bulk%fnx
fny=p_Bulk%fny
fnz=p_Bulk%fnz
nxhp=p_Bulk%nxhp
nz=p_Bulk%nz
deltaD=p_Layer%deltaD
```

```
        aindex=p_Layer%aindex_mid
        delta_y=1./p_Bulk%fny
        testy1=dabs(y)-delta_y
        testy2=dabs(oy)-delta_y
        L_nshot=.false.
        if((y*oy.le.0.).or.(testy1.le.0.).or.(testy2.le.0.))then
                L_nshot=.true.
        end if
        if(l_nshot) then
                ishot=0
                ds=lshot/aindex
                if(ols.eq.0) then
                        ds=-deltaD
                endif
                do while(ds.le.ols)
                        ishot=ishot+1
                        Ds=Ds+deltaD
                        Xi=oX+DS*ux
                        Yi=oY+Ds*uy
                        Zi=oZ+Ds*uz

        !CC***DEPOSITE
                        MX=NINT(fnx*Xi)
                MY=NINT(fny*Yi)
                MZ=INT(fnz*Zi)
                IF((MY.EQ.0).AND.(Iabs(MX).Lt.nxhp).AND.(MZ.Le.nz).and.(mz.ge.(-10)))then
                                Nsnapx=int(1/(1+iabs(mx)))
                                Nsnapz=int(1/(1+iabs(mz)))
                                mx=mx+nxhp
                                pDEPOSIT(MX,MZ+11)=pDEPOSIT(MX,MZ+11)+1
                        end if
80              end do
                p_Photon%nshot=p_Photon%nshot+ishot
                p_Photon%lshot=(dsqrt((xi-ox)**2+(yi-oy)**2+(zi-oz)**2)-ols)*aindex
        endif
        return
        end subroutine
```

The constant “deltaD” in the codes is the traveling distance in any arbitrary medium of the light within the duration of one "time slice". We adjust the snapshot interval though controlling the value of “deltaD”. The subroutine is named “snap_shot” after the fact that the time slicing procedure resembles taking snap shots in film making. The program tests whether the trajectory penetrates through the considered monolayer by an efficient

method of multiplying the variables y1 and y2 in the codes. If the trajectory penetrates the monolayer, the product of y1 and y2 will yield a non-positive value.

4.1.2. Photon Injection at the Boundary

The photons contained in a laser beam are incident at the tissue phantom boundary, or the interface between the ambient medium and the tissue, and enter into the tissue according to their incident angle. This process is called photon injection in this thesis and is described in the following subroutine:

```
        subroutine Inc_pst(p_Beam, NN, Xinc, Yinc)
        implicit real(8) (a-h, o-z)
        integer(4) NR0,NN
        type(BeamStruct), pointer:: p_Beam
        real(8) fr0,Xinc(p_Beam%maxNN),Yinc(p_Beam%maxNN), rsq, x, y
        common/const/Pi,zero_p,one_m,hPis,coszero,cos90d
NN=0
        fr0=p_Beam%fr0
        nr0=p_Beam%nr0
        DO I=1,2*nr0+1,1
        Y=nr0-(I-1)
DO J=1,2*nr0+1,1
X=nr0-(J-1)
rsq=x*x+y*y
        if ( rsq.LE.(nr0**2) ) then
NN=NN+1
Xinc(NN)=fr0*x
Yinc(NN)=fr0*y
end if
ENDDO
ENDDO
        return
        end subroutine
```

The ambient medium side of the interface, the x-y plane at $z = 0_-$, in the considered region can be visualized as a sieve with $\pi(NR0)^2$ meshes, where the parameter NR0 is used to control the number of injected photons.. Each photon will be injected though one of these meshes with the x, y coordinates of the mesh stored in the arrays Xinc() and Yinc(), respectively. The distribution of the photons injected at the sieve will be varied

according to the profile of the laser beam. For a "top-hat" beam, in which the transverse light distribution follows a rectangular shape as a function of distance from the beam center, the number of photons injected though each mesh inside the beam radius will be a constant. For a Gaussian beam, the number of photons injected at different interface locations will vary according to a Gaussian function. An additional subroutine Gauss_beam() will be resorted to calculate the number of injected photons at different meshes. The following codes are used for injecting a converging laser beam of Gaussian profile on a rough interface between the ambient medium and the tissue phantom:

```
subroutine Gauss_beam(x1,y1,ax1,ay1,Ir,aIr,p_Beam, p_Seed,bni,bnr,Z)
implicit real(8) (a-h, o-z)
integer(4) ir
real(8) x1,y1,ax1(140),ay1(140),U(3), aN(3), aIr
real(8),  pointer::Z(:)
type(SeedStruct), pointer:: p_Seed
type(BeamStruct), pointer:: p_Beam
common/const/Pi,zero_p,one_m,hPis,coszero,cos90d
r0=p_Beam%Radius
xpls_w=p_Beam%xpls_w
aIr=exp(hPis*(1.-(x1*x1+y1*y1)/(R0*R0)))
F=p_Beam%Focus
r1=1/dsqrt(x1*x1+y1*y1+(F-z(1))*(F-z(1)))
U(1)=-x1*r1
U(2)=-y1*r1
U(3)=(F-z(1))*r1
rs=1.0/dsqrt(z(2)*z(2)+z(3)*z(3)+1.0)
aN(1)=z(2)*rs
aN(2)=z(3)*rs
aN(3)=-rs
call Cal_Refficient(aN, U, bni, bnr, reff)
Ir=Nint(aIr*1-aIr*reff)
ic=0
irsqrt=int(sqrt(float(ir)))
if(irsqrt.ge.1) then
        dx1=xpls_w/Irsqrt
        do iy=1,irsqrt
        y1i=y1+dx1*(iy-irsqrt/2-1)
        do ix=1,irsqrt
                ic=ic+1
                ax1(ic)=x1+dx1*(ix-irsqrt/2-1)
                ay1(ic)=y1i
        end do
end do
```

```
endif
do ix=ic+1,ir
        ax1(ix)=x1+xpls_w*(0.5-ran2(p_Seed%iseed_hash))
        ay1(ix)=y1+xpls_w*(0.5-Ran2(p_Seed%iseed_hash))
end do
return
end subroutine
```

This subroutine starts by calculating the photon distribution at the medium side of the interface using a Gaussian function. Then the light transmittance within each mesh is obtained through the determination of the incident angle and using the Fresnel formulae. The photon injection is further improved with a "hash" procedure to acquire smooth distribution of photons at the ambient medium side of the interface. In this procedure multiple discrete x and y coordinates are used for photons passing through the same mesh to simulate the continuous distribution of photon at the medium-tissue interface for a practical laser beam.

4.1.3. Photon Tracking in 3-d Space

After the photons are injected through the "sieve", the trajectory of a tracked photon is determined by a series of changes in its position and direction as a result of scattering before absorption or escape. Typically a cylindrical coordinate system is adopted in tracking analysis, due to the symmetry of the problem, for the ease of analytical solutions with trigonometric functions. However, numerical calculations of trigonometric functions are time consuming because these calculations require computing series with many terms. Therefore, we use only one Cartesian coordinate system (see Fig. 1) which is fixed with the tissue phantom in the codes to calculate the trigonometric relations in individual

photon tracking [Wang, 1995]. In the codes, a data structure is generated to store the photon tracking information:

```
type PhotonStruct
        real(8)   ox, oy, oz
        real(8) x, y, z
        real(8)   ouN(3), uN(3)
        real(8)   ls_left, la_left, ols, lshot
        integer(4) nscatt, nshot
        integer(4) layer_index
        logical(1) b_alive, not_hit
end type PhotonStruct
```

The coordinate variables ox, oy, oz and x, y, z represent the coordinates of a photon before (old) and after a scattering event, respectively. The length variables, ls_left and the la_left, label the remaining distances to the next scattering site and to the end of life, i.e., be absorbed, for a photon, respectively. The current direction of the photon is specified by a unit vector variable uN(3). The last scattering length is stored in the variable ols. The direction of the photon before last scattering is specified by the other unit vector ouN(3). The variables ols and ouN(3) are specially useful in the events of reflection and refraction at interfaces. Since both reflection and refraction cause the deflection of the photon from the initial direction, variables ols and ouN(3) are necessary to record the extra information from the event. When the tracked photon hits a boundary of the considered region in the tissue, ols is used to record the scattering length from the last scattering site to the hitting point at the boundary and ouN(3) is used to store the incident direction before reflection and refraction. The flag b_alive indicates the life status of the photon and the flag not_hit indicates whether the photon hits any interface since last scattering. Each time a photon travels to a new site, the program will call subroutine "snap_shot" to slice the scattering trajectory into many slices, resembling many snap shots of the

photon's motion along its trajectory. These temporal photon density distributions are then accumulated into the array DEPOSIT. During this procedure, the data structure pointer of PhotonStruct is utilized to transfer the photon tracking information to subroutine "snap_shot". Because the snapshot time is a fixed time interval, the variable "lshot" is used to specify any residual optical path since the last snapshot and will be used in the first snapshot before the next scattering event ensure equal time intervals. The implementation in code is display in the snap_shot() subroutine previously discussed.

4.1.4. Two-layer model of the Skin Tissue

In the two-layer model of skin tissue, two interfaces have to be considered: one between the ambient medium and the tissue and the other between the two neighboring layers. Including the ambient medium and the skin tissue beyond the considered depth as additional layers, an ascending layer index (Layer_index) is used to label which region or layer the tracked photon is located: 0 for ambient medium, 1 for epidermis, 2 for dermis within the considered depth and 3 for rest of the dermis out side of the considered region. Again we employ data structures for layers and interfaces to cluster different parameters for efficient programming. Pointers are used to access these structures in the computer memory for minimizing overhead when calling the functions or subroutines. These structures are displayed as follows:

```
type LayerStruct
        real(8) amuS, amuA, g, deltaD
        real(8) aindex_up, aindex_mid, aindex_down
        real(8) z_sfc, z_btm
        real(8) cos_critsfc, cos_critbtm
        integer(4) sfctype, btmtype
        integer(4) irfr_sfc,intref_sfc,idead
        integer(4) irfr_btm,intref_btm
```

```
end type LayerStruct

type SurfaceStruct
        real(8) Deltl, Al
        real(8) x,y,fl
        real(8) vx0,vy0
        real(8) fnx,fny
        integer(4) nx,ny,nxhp,nyhp
        integer(4) nfx, nfy
end type SurfaceStruct
```

The constants amuS, amuA and g in LayerStruct are scattering coefficient, absorption coefficient and asymmetry factor, respectively. The refractive indices of the upper layer, the current layer and the lower layer are stored in aindex_up, aindex_mid and aindex_down, respectively. The constants z_sfc and z_btm specify the z coordinates of upper interface and lower interface. Parameters sfctype and btmtype define whether the upper and lower interfaces are rough or smooth surfaces. SurfaceStruct includes Deltl and Al which describes the rms height and transverse correlation length of rough surface. The x, y are the length and width of the rough surface considered in the simulation with Nx and Ny being the dimensions of the array holding the rough surface information.

4.1.5. Treatment of Photon Escape from the Considered Region

In the one-layer model for the skin tissue which is assumed infinitely thick, only one interface exists between the ambient medium, such as water or air, and the tissue. When a photon moves toward the interface from inside the tissue, a random number (RND) with $0 < RND < 1$ will be generated to treat the Fresnel reflection statistically. If $RND > R$, the photon transmits through the interface and is considered lost from the considered region, otherwise it reflects back and continue to migrate in the tissue. For those reflected photons, the direction is the reflection direction and the new position is obtained by

mirroring the predetermined next scattering site with respect to the interface plane. The corresponding flow chart is displayed in Appendix A.

In the same fashion, the two-layer model also uses "roulette" to determine if a photon transmits or not when it is incident on an interface with the photon's new position set at the incident point at the interface. As we discussed before, in the codes two additional layers are included for the ambient medium and the dermis outside the consider region. In general, the layer index will increase by 1 if the photon transmits through a lower interface and will decrease by 1 when transmit through an upper interface. If the layer index becomes 0 (ambient medium) or 3 (deep dermis) the photon tracking is terminated for its escape from the considered region and next photon will be injected. If the photon transmits through the epidermis-dermis junction, the new direction is determined by the Snell's law and the scattering length L_s and absorption length L_a are modified according to Eqs. (3.5.13) and (3.5.14). The procedure for the multi-layer model is described by the flow chart in Appendix B.

4.2. Comparison of Random Number Generators

We quote the following definition to commence our discussion on random number (RND) generator: "A loose definition of a random number is a numerical value resulting from a process or experiment whose value cannot be predetermined by the initial condition" [Hammond *et al*, 1994]. According to this definition, RNDs are unpredictable in their values and not correlated to each other. No algorithm could yield sets of truly random numbers. Although one can use the outputs of some intrinsically random physical

processes to generate RNDs, such as the elapsed time of decaying radioactive elements, they are inefficient and inconvenient to use. An alternative approach is to use a pseudo-RND generator, which is a predefined algorithm producing a periodic sequence of hashed numbers. Nearly all the RNDs used in computer codes are obtained by this means. We tested several pseudo-RND generators in search for a most efficient routine with uniformly distributed RNDs and longest period for our codes.

Generally, RND generators can be categorized into four classes with respect to their algorithms: linear congruential generator (LCG), lagged fibonacci generator (LFG), shift register generator (SRG) and combined generators.[Marsaglia, 1985]

The most commonly used RND generator is LCG, which was first proposed by D. H. Lehmer.[Lehmer, 1949] LCGs are widely used in subroutines with C codes. LCGs generate a sequence X_i of random integers based on the following iterative algorithm:

$$X_i=(aX_{i-1}+c) \bmod M \qquad (4.2.1)$$

where *a* is the multiplier, c is the additive constant and M is the modulus. *Xi* is also called seed in the RND generator. The initial X_1 is called initial seed. The initial seed determines the whole random sequence. The three parameters a, c and M must be chosen meticulously in order to reach the maximum period of the random number sequence, which amounts to the modulus M. LCGs work well in many applications, but they have some inherent drawbacks. The major two are the low-bit correlation and the consequent spectral problem. However, these can be solved by "warm-up" and "shuffle" methods [Press, 1992].

LFGs are becoming popular recently because of their long period, high computation speed and simple methodology. They were proved to be very good uniform pseudo-RND generators through the Marsaglia's tests [Marsaglia, 1985]. The core algorithm can be summarized as follows,

$$X_i = X_{i-p} + X_{i-q} \ (mod\ M) \qquad (4.2.2)$$

where X_i is the RNDs generated by this recursive scheme, i is the index number of the set members of random sequence X, p and q are integers representing lags (p>q>0). The current X_i is determined by the values of X from p and q places before I in the sequence. To obtain periods as long as $(2^p-1)2^{m-1}$ in the LFGs, one has to use power of 2 as the value of M ($M=2^m$) and to choose appropriate values for p, q and the first p initial values of sequence X.

SRG is mentioned here to emphasize its historical contribution because it is nearly phased out in scientific calculations. SRG was firstly proposed by Tausworthe [Tausworthe, 1965] in 1965 and improved by Golomb and Lewis [Golomb, 1967; Lewis, 1973]. The general form for SRG is

$$X_{i+k} = \sum_{m=0}^{k-1} a_m X_{i+m} \pmod 2 \qquad (4.2.3)$$

where the a_m's are either 0 or 1. SRGs have been very popular for they are comparatively speedy. Nevertheless, the randomness among the pseudo-RND is not as good as the other two RND generators which seriously impedes their progress.[Knuth, 1998; Marsaglia, 1985]

In general, an ideal RND generator should produce RNDs which are uniformly distributed, uncorrelated and reproducible. In addition, it should be portable and efficient in terms of calculation speed and memory usage. These requirements are especially important to the Monte Carlo simulations employing an enormous quantity of RNDs. In our search for an optimal RND generator, the generator must survive such basic tests as the correlation test, spectral test and standard deviation test [Fisherman, 1996]. Preliminary tests are conducted on some pseudo-RND generators readily available from the book *Numerical Recipe* [Press *et al*, 1992] and the IMSL mathematical library package. In this test, we set up 10^5 bins to collect the random numbers fall into the bin, and the sample number of random numbers is 10^8. The average number falls into each bin is 10^3. The results are listed in Table 1.

From the results, we chose Ran2 as our random number generator, because it has a long period, short computing time and availability of its source codes for portability. We randomly select the initial seeds for each of a random process so as to decrease the correlation and increase the period. Firstly, the current time from the computer is retrieved as a RND using a subroutine Init_seed(). This step ensures that the seed to be randomly different at different time. Then the random number generator ran4() is used to generate another RND for different random processes by another subroutine swap_seed(). Since ran4() is different kind of generator from ran2(), the RND will be uncorrelated with those produced by ran2(). The multiplication of the two RND is then passed through a high-low bit swapping process by recursive shifting to obtain a random number seed. The

new seed will be checked to see if it is of negative value to satisfy the initial seed requirement in ran2(). The following code is the implementation of the seed initiation.

```
subroutine Init_seed(p_Seed)
        type(SeedStruct), pointer:: p_Seed
        integer iseed
        iseed=time()
        call swap_seed(p_Seed%iseed_ls, iseed)
        call swap_seed(p_Seed%iseed_la, iseed)
        call swap_seed(p_Seed%iseed_phi, iseed)
        call swap_seed(p_Seed%iseed_psi, iseed)
        call swap_seed(p_Seed%iseed_ref, iseed)
        call swap_seed(p_Seed%iseed_rrs, iseed)
        call swap_seed(p_Seed%iseed_hash, iseed)
        return
end subroutine

subroutine swap_seed(iseed, iseed_ran4)
        integer i, iseed
        iseed=time()*ran4(iseed_ran4)
        do i=32, 2, -1
                iseed=ishftc(iseed, -1, i)
        enddo
        iseed=-iabs(iseed)
        return
end subroutine
```

In the future, we plan to test more RND generators to improve our current RND acquisition process.

4.3. Time-resolved Simulation

In addition to calculating the steady-state results in light distribution, the new Monte Carlo method can also be used to obtain time-resolved results. For this purpose, the photon density can only be obtained before a specific time T by accumulating the time slices along a photon's temporal trajectory up to T. In the code we listed above, the time slicing process is conducted in the snap_shot(). A parameter "nshot" is used in the photon data structure to record how many snap shots the photon has experienced since launched.

Suppose a photon is injected at time t = T_0 and we need to calculate its contribution to the photon density at time t = T, a parameter "iframe" will be obtained:

$$iframe = \frac{T - T_0}{\tau} \tag{4.3.1}$$

where τ is the width of a time slice or the interval between two consecutive snap shots. The "nshot" will be compared with "iframe" after each snap shot. When nshot > iframe, the photon will not be tracked and the next photon will be injected and tracked. Using this approach, we can obtain the time-resolved light distribution in terms of photon density at time T.

4.4. The Handling of Rough Surfaces and Interfaces

With the expression of surface elevation given by Eq. (3.3.6), the modeling of the interfaces as rough surfaces is conducted numerically. The parameters in Eq. (3.3.6) are set at the beginning of the program except X_{ij}. Because X_{ij} needs to be a Gaussian random number and usually uniform pseudo-random number generator is easier to implement in the computer, we adopted the Marsaglia and Bray modification of the Box-Muller transformation to obtain the Gaussian random numbers from uniform random numbers [Marsaglia, 1961; Kendall, 1987]. To reduce the edge effect caused by the finite Fourier series, usually only the inner center square is cut out from a bigger sample. For instance, we generate a randomly rough surface sample with a dimension of 1024x1024 and take out the center square with the dimension of 501x501.

A dynamic memory allocation scheme is adopted in our method to save the memory usage and to increase the computational efficiency. For instance, a few temporary data arrays are allocated to store the information of the generated surface since we need only part of the generated surface. After the randomly rough surface is obtained, the center square will be pasted into a new smaller array and the old temporary arrays will be deallocated to save the resources. The following few lines display the FORTRAN code used to implement this procedure.

```
        allocate(CFFT(1:NFX*NFY*2),CFFTX(1:NFX*NFY*2))
allocate(CFFTY(1:NFX*NFY*2),SZ(1:NsX*NsY*3))
!CFFT contains surface elevation, SZ contains the center square
!CFFTX CFFY contains the partial derivative with respect to x and y.
        call RANDMS(CFFT, cfftx,cffty, ISEED_rrs, NFY,NFX,NsY,NsX,SZ)
        deallocate(cfft,cfftx,cffty)
        allocate(surface(1:NsX*NsY*3))
        !reorder the information
        DO J=0,NsY-1,1
                DO I=1,NsX,1
                        surface(J*NsX*3+(I-1)*3+1)=SZ(J*NsX+I)
                        surface(J*NsX*3+(I-1)*3+2)=SZ(J*NsX+I+NsX*NsY)
                        surface(J*NsX*3+(I-1)*3+3)=SZ(J*NsX+I+NsX*NsY*2)
enddo
enddo
deallocate(SZ)
```

The real type arrays CFFT, CFFTX, CFFTY are the temporary arrays used for the bigger surface sample to store the surface elevation, the partial derivative of surface elevation with respect to x and y coordinates, respectively. The real type array SZ is the temporary array holding the information such as surface elevation $<\zeta(x,y)>$, the partial derivative $<\zeta_x^{'}(x,y)>$ and $<\zeta_y^{'}(x,y)>$ of points on the center square that is cut from the bigger surface sample. Since the three parameters for each point at the surface are located in three reciprocally remote memory locations, a real type array SURFACE is used to move the three parameters of the same point in the neighboring locations. The

above method is used to implement the pointer transfer based on the locality of memory reference [Stone, 1987]. When the information of the specific point on the rough surface is requested, a pointer associated with the memory cells containing the three parameters will be passed. The use of pointer efficiently reduced the overhead of parameter transfer between functions.

From our test results, an interesting phenomenon draws our attentions and consequently leads to the using of large number of surface samples. Fig. 11 displays a gray scale bitmap image of the photon distribution with single surface sample in x-z cross-section showing the asymmetry of z-axis due to the fluctuation of the surface elevation. In this case the curvatures of the interface act as many convex and concave microlenses, resulting in the random “streaks” displayed in the image. The effect of “streak” will be reduced as the sample number of the randomly random surfaces is increased. The use of large number of random surfaces is justified by the fact that the optical properties of biological tissues are not only randomly distributed in space but also in time. With 100 samples of the random surfaces and all other parameters unchanged, the Fig. 12 shows the bitmap image of the photon distribution with streaks nearly removed.

Chapter 5: Results and Discussion

Based on the framework of radiative transfer theory, we developed a new Monte Carlo method to simulate light distribution of a focused laser beam propagating inside skin tissue phantoms of various optical properties in near-infrared region. Both steady-state and time-resolved distributions of the photon can be obtained using the new "time-slicing" method. More importantly, the effect of rough surfaces on the light distribution is investigated. Several new features of the propagation can be observed from our simulations for a converging beam in a turbid medium of skin tissues. The first two sections present the steady-state results from the one-layer and two-layer model of the skin tissues and the last section provide the time-resolved results with the two-layer model.

5.1. One-layer Model with a Smooth Surface [Song *et al.*, 1999]

In the one-layer skin model, we assume that both the epidermis and the dermal tissues of human skin posses the same optical properties with an optical index of n=1.41. For simplicity, we further assume that interface between the ambient medium, air in this model, and the skin tissue phantom is optically smooth and flat and the photons are injected on the tissue side of the interface at $z = 0_+$. This will enable us to concentrate our investigations on the effects of the beam profile, scattering coefficients and asymmetry factor on the light distribution inside the skin tissue phantom.

5.1.1. The Effect of Beam Profile

First, we verify that the boundary conditions, which are determined in our cases by the beam profile F(x, y) at $z = 0_+$, influence mostly the photon density distribution near the air-tissue interface. This is manifested by comparing the contour diagrams of the photon density in the cross section of the laser beams of different profile near the interface in the y-z plane. Fig. 13 and Fig. 14 exhibit such a comparison for the beams of gaussian and "top-hat" profiles with the same radius of 0.268 mm. The cone angle of the converging beam is given by $\alpha = 30^o$ and proceeds as a spherical wave toward the geometric focal point at d = 1mm below the surface, as shown in Fig. 15. The following values of the optical parameters are chosen for the tissue: $\mu_s = 10$ (mm^{-1}), $\mu_a = 0.01$ (mm^{-1}) and g=0.9. The total number of the photons simulated is $N = 5.6\times10^{11}$ with $N_1 = 1.4\times10^7$ individually tracked, where N_1 is corresponding to the N_0 in §2.3 and N is the product of N_1 and m_{max}. From these figures we can recognize that the effect of the beam profile on the light distributions is most prominent near the interface.

For both cases, the maxima of the photon density distributions occur on the z-axis between the interface and the geometrical focal point with the "top-hat" beam's maximum penetrating deeper. To show this clearly, we plot the photon density in Fig. 16 as a function of z on the z-axis for each of the two beams. It demonstrates that the curve of the photon density between the photon entrance and the peak for the gaussian beam is steeper than that of the "top-hat" beam because the former has most of the photons concentrated near the z-axis.

5.1.2. The Effect of Scattering Coefficient

The wavelength of the laser beam in our simulation is in the near-infrared region or about 1 μm. For the spectral region concerned here, it is well known that scattering dominates the light-tissue interaction and is peaked strongly in the forward direction [van Gemert *et al*, 1989]. For this reason, the asymmetric factor of scattering $g = \langle \cos\theta \rangle$ is chosen to be 0.9 in all the cases. However, the experimental determination of optical parameters, μ_s and μ_a, in the near infrared region has been scarce and results vary significantly for the skin tissues [van Gemert *et al*, 1989; Marchesini *et al*, 1992; Graaff *et al*, 1993]. Different values of μ_s have been used in our simulations to investigate the dependence of the light propagation on the scattering coefficient. For results presented in this section, we chose $\mu_a = 0.1$ (mm^{-1}). Fig. 17 and Fig. 18 display the 3-d distributions N(0,y,z) of the number of photons per grid cell in the y-z plane for a beam of gaussian profile with e^{-2} radius of 0.188 mm at the optically smooth boundary z=0 with $\mu_s = 6$ (mm^{-1}) in Fig. 17 and $\mu_s = 10$ (mm^{-1}) in Fig. 18. The total number of the tracked photons is given by $N_1 = 1.41\times10^7$ and the size of the recording region is given by 1mm in x- and y-directions and 1.5mm in z-direction. The tracking region has each of the three sides increased from the sides of the recording region by a factor of 3 so that the errors in the photon density distribution, owing to the backscattered photons from the outside of the tracking region, are negligible.

The effect of the scattering coefficient on the distribution of photon density can be clearly seen in Fig. 19 in which the number of photons per unit volume, N(0,0,z), is

plotted as a function of z on the z-axis for different values of μ_s. From Fig. 19, we can see that the photon density either increases slightly higher for small μ_s or decrease for large μ_s as the beam penetrate into the tissue until reaching a peak at the focal spot near z = 1.0mm. The photon density can be calculated at the entrance of the tissue phantom, N_e, by averaging N(0,0,z) over the region of 0.0mm < z < 0.1mm near the air-tissue boundary and the corresponding peak value at the focal spot. The ratio of the photon densities, given by N_f / N_e, then provides the information on the distribution of laser radiation that is of concern in applications using converging laser beam to treat skin lesions under the skin surface. For this purpose, the ratio of N_f to N_e is shown as a function of μ_s in Fig. 20.

For tissue phantoms with optically smooth interfaces, it is clear from Fig. 18 that even for the large scattering coefficient $\mu_s = 10mm^{-1}$, the initially focused laser beam remains partly converging inside the tissue. As shown in Fig. 19, a local peak can be identified at the focal spot, 1mm under the air-tissue boundary, for a wide range of attenuation coefficient $\mu_t = \mu_s + \mu_a$ from 4.1 mm^{-1} to 12.1mm^{-1}. Furthermore, the spread of the photon density near the focal spot along the z-axis in Fig. 19 is due to the refraction of the converging laser beam at the air-tissue boundary. While the photon density at the entrance of the tissue phantom, N_e, remains virtually as a constant because it is determined mainly by the total tracked photon number N_0, the peak photon density at the focal spot normalized by N_e, or N_f / N_e, decrease exponentially as the μ_s increases for $\mu_s \leq 8mm^{-1}$. Since the ratio of the unattenuated photons to the total photon number obeys the same exponential dependence on the attenuation coefficient μ_t ($\approx \mu_s$) according to the radiative transfer theory, we can immediately identify N_f as the unattenuated photon

density plus a background contributed by the scattered photons. As the scattering coefficient increases to μ_s >8 (mm^{-1}) with negligible μ_a, shown in Fig. 20, the photon density ratio approaches to a plateau representing the scattered light background. Two comments may worth mentioning here on the results displayed in Fig. 20. First, for simple phantoms we are considered in this thesis, the laser irradiance (proportional to the photon density calculated here for monochromatic laser radiation) delivered at the focal spot can be ten times or larger than the irradiance elsewhere inside the tissue if μ_s ($\approx \mu_t$) < 7 (mm^{-1}). These situations are desired for treatment of dermal lesions using a converging beam of short laser pulses to reduce collateral tissue damage [Hu, 1995]. Secondly, the exponential dependence of the unattenuated photon density on the attenuation coefficient requires accurate determination of these coefficients for optimal use of laser radiation in dermatology and plastic surgery.

5.2. One-Layer Model with Rough Surface

Several subroutines are added to the previous Monte Carlo codes to simulate and study the effect of rough surface on the light distribution of a converging laser beam in the same one-layer model as described in §5.1. When we consider the effect of rough surface, the refraction of light through the surface has to be considered. Therefore, the photons are injected from the ambient medium side of the interface z = 0., as indicated in Fig. 1. A beam of gaussian profile at z = 0. is assumed with initial cone angle in the ambient medium given by $\alpha = 30^o$ and the e^{-2} radius r = 0.188mm, which is defined at e^{-2}

of the central peak radius of the beam. Two different surface profiles are generated with the different rms height δ = 0.125μm and 0.250μm while the lateral correlation length is kept as a constant a = 10.0μm to simulate the packed cells in the stratum corneum of the skin [Schatzlein *et al*, 1998].

Two cases have been investigated with air (refraction index n_0 = 1.00) or water (n_0 = 1.33) as the ambient medium outside of the tissue phantom which assumes a refraction index n 1.41. For the case of air, we plot the z-dependence of the photon density N(0,0,z) in Fig. 21 with μ_s = 4.0(mm^{-1}), μ_a = 0.1(mm^{-1}), g = 0.9. The result of smooth surface (δ = 0) is included for comparison. A set of 20 realizations of the rough surface has been used to obtain the results for rough surface cases. All the curves of the photon density reach a peak value at the geometric focal spot z = 1mm. For the case of water as the ambient medium, the radius of the beam at the water side of the interface is changed to r = 0.3902mm to ensure that the cone angle remains 30^o and the focal spot z = 1mm. As we expect, the refractive index of the ambient medium plays an important role in the reduction of the magnitude of the photon density at the focal spot. This is illustrated by the z-dependence of the photon density N(0,0,z) in Fig. 22.

In determining the optical parameters, μ_s, μ_a and g, of the skin tissues, indirect methods have to be used by fitting the transmittance and reflectance measurements to calculations based on an analytical or numerical model [Gemert *et al*, 1989;Graff *et al*, 1993]. The effect of rough interfaces between tissue sample and the holder (typically made of glass) has never been considered in the *in vitro* measurements. According to our experience in tissue experiments, it is very difficult to avoid trapping of air bubbles between the tissue

and the holder. Therefore, modeling of the glass-air-tissue boundary of a tissue slab sample with thickness typically less than 1mm as a rough interface has practical implications. The results in Fig. 21 and Fig. 22 clearly indicate that the peak photon density at the focal spot can be significantly reduced by the roughness of the air-tissue boundary even for surface profiles with very small δ/a ratio, which approaches to zero as the roughness disappears. As shown in Fig. 21, as the rms height of the surface fluctuation δ increases beyond the values of 0.25μm, the photon density peak completely disappears owing to the refraction of the light at the rough surface. The reduction of the photon density at the focal spot is significantly moderated if the ambient medium is replaced by water - the peak exists until δ is larger than 1 μm, as displayed in Fig. 22. The difference between Fig. 21 and Fig. 22 is due to the much reduced refraction index mismatch between the two sides of the interface.

An important conclusion can be drawn from our preliminary results concerning the effect of rough surface on light distribution. The bulk scattering coefficient can be significantly overestimated if the roughness of the air-tissue boundary is not appropriately controlled or taken into consideration. We should point out here that the validity of considering refraction at micrometer scales in the framework of radiative transfer theory has not been fully justified. Further investigations are currently in progress and will be published elsewhere.

5.3. Two-Layer Model with Rough Surfaces

The two-layer skin model is more complicated than the one-layer model for both refracted and reflected photons at the epidermis-dermis junction, which is treated as another rough surface, have to be tracked. The variation of refractive indices and the rough surface profiles affects the light distribution in several aspects. For the skin tissue model, the surface elevations and lateral correlation lengths of the superficial interface between the ambient medium and the epidermis as well as the epidermis-dermis junction have been well documented.[Anderson *et al*, 1981; Marchesini, 1992; Schatzlei et al, 1998] The refraction index of the skin dermis is found to be 1.41 from literature.[Schatzlei et al, 1998] However, the data for the refractive index of the epidermis has been scarce. The only published data, to the best of our knowledge, are the index of stratum corneum given by 1.55 [Anderson *et al*, 1981]. The stratum corneum consists of the dehydrated cells and has less water than other layers in epidermis. So we expect that index of epidermis is between the index of stratum corneum and that of the dermis. Two different values of refraction index, n=1.45 and n=1.55 and two different absorption coefficients μ_a=5.0 mm^{-1} and μ_a=0.5 mm^{-1}, are used to model epidermis. The other optical parameters of the skin tissue phantom are μ_s=6 mm^{-1}, g=0.9 for the epidermis and μ_s=4 mm^{-1}, μ_a=0.5 mm^{-1}, g=0.9 for the dermis [Schmitt *et al*, 1990]. The results of the four cases are displayed by Fig. 23, Fig. 24, Fig. 25, Fig. 26 and Fig. 27. The photon density N(0,0,z) along the optical axis with respect to z is plotted in Fig. 23. The result obtained with the optical index of n = 1.55 and μ_a=5.0 in epidermis shows that the photon density decreases almost continuously along the z-axis. When the absorption

of the epidermis layer is decreased by adjusting μ_a to be 0.5, a hump will appear in the dermis layer. However, the maximum is greatly left-shifted than the expected focal spot of the beam. For the case of n = 1.45 and μ_a=5.0 in the epidermis, the curve kept dropping in the epidermis layer due to the high absorption. The curve will also form a hump in the dermis layer but less left-shifted than the former one. The maximum of this curve is also less than the case with n = 1.55 and μ_a=5.0 in epidermis since the absorption in the epidermis layer dominates and reduces the survived photons. The solid black curve represents the case with n = 1.45 and μ_a=0.5 and a peak in photon density is located at the focal spot of the beam. However, the peak is not as sharp as the peaks in Fig. 21 as a result of imposing one more rough interface at z=0.1 to model the dermis-epidermis junction. Note that the ratio δ/a of the rough surface at the epidermis-dermis junction is much larger than the superficial rough surface. Hence the roughness of the junction causes severe deflection of the photons from their initial direction if the refraction index mismatch remains about the same at the two interfaces. As a result, not all of the unattenuated photons reach to the geometrical focal spot and the deflection by refraction hashes the unattenuated photons around the focal spot like displayed in the solid line. If the difference of refractive indices of the optical matters beside the rough interface is large enough, the attenuated photons overwhelms the unattenuated photons such that the peak disappears as shown in the lines with n=1.55. Consequently, we draw a conclusion that in a two-layer model, both absorption of the superficial layer and the mismatch of the refractive indices between layers could affect the photon density distribution in tissue phantom. The mismatch of the refractive indices could affect decrease the peak and shift

the peak. The effect of absorption in the first layer is expanding the width of the peak. Fig. 24, Fig. 25, Fig. 26 and Fig. 27 plot the contour plots of the photon density distribution for the four cases mentioned above respectively. In Fig. 24 and Fig. 25, it is evident that the photon density's maxima are located in different positions of z coordinate. Comparing Fig. 26 and Fig. 27, we can find the light energy will penetrate deeper with less difference of refractive indices at the water-tissue interface and epidermis-dermis interface. Besides, another characteristic is worthy to be noticed, the close contours are "eroded" at the dermis-epidermis junction. From the empirical point of view, the measurement of light distribution near the junction should take this fact into consideration.

5.4. Time-Resolved Results with the Two-Layer Model

As to the time-resolved light distribution, some time-resolved results of two-layer skin model with rough interfaces are presented to display the migration of photons and the local responses of tissue phantom.

The time-resolved result of photon migration has been discussed in the form of a single laser pulse [Jacques, 1989], which concentrates the tissue response of a single laser pulse. We investigated the time-resolved result for a laser beam with constant power supply to observe the evolution of light distribution in the tissue phantom with respect to time. By using the time-slicing method, we conducted a time-resolved tracking of the photon migration in two-layer skin models with the same configuration as mentioned in §5.1.3. Fig. 28, Fig. 29 and Fig. 30 manifest the results for the model with refractive index of

dermis layer n = 1.55 and μ_a=0.5. Fig. 31, Fig. 32 and Fig. 33 are the results for the model with n = 1.45 and μ_a=0.5. Fig. 34, Fig. 35 and Fig. 36 display the results for the model with n = 1.45 and μ_a=0.5. And the results for the model with n = 1.45 and μ_a=0.5 are plotted in Fig. 37, Fig. 38 and Fig. 39. In Fig. 28, Fig. 31, Fig. 34 and Fig. 37, the twelve curves represent the photon distribution at t=300fs, 600fs, 1000fs, 2000fs, 3000fs, 4000fs, 5000fs, 6000fs, 10000fs, 20000fs, 30000fs and steady-state light distribution. The curve for light distribution with t ≥ 10ps overlaps with the steady-state results, indicating that the system's response reaches a steady state when t ≥ 10ps. This fact verifies that the steady-state results practically will not vary with the fluctuation of m_{max} in §2.3. The rightmost part with larger value of Z in each curve describes the motion of photons in the wavefront. During the first short period before the wavefront reaches a position deep under the medium-tissue surface in the tissue phantom, the photon density will remain zero. After the first few photons migrating into this position, the photon density will increase until reaching to a plateau. This is illustrated in Fig. 29-33, Fig. 35-36 and Fig. 38-39. Fig. 29, Fig. 32, Fig. 35 and Fig. 38 display the evolution of photon density at z=1.0 on z-axis. Fig. 30, Fig. 33, Fig. 36 and Fig. 39displays the evolution of photon density at z=0.1 on z-axis where the epidermis-dermis junction locates. These are essentially the locally responses in Section 3.3. In Fig. 29, Fig. 30, Fig. 32, Fig. 33, Fig. 35, Fig. 36, Fig. 38 and Fig. 39 , we can find that the time needed to reach the steady state is not same for both cases. For the cases in Fig. 30, Fig. 33, Fig. 36 and Fig. 39, the time is only less than 3000fs, while it will take more than 6000fs to reach a steady state for the cases in Fig. 29, Fig. 32, Fig. 35 and Fig. 38. From the above, it turns out that the time to

reach to a steady state is dependent on the position of the point investigated. For a tissue phantom as a system, the size of the tissue phantom will decide the lag time to reach a steady state.

Chapter 6: Summary

Through this research project, we have developed an efficient method of Monte Carlo simulation to numerically investigate the propagation of converging laser beams in different skin tissue phantoms. This method has enabled us to directly obtain photon density inside the tissue phantom for laser beams of different profiles, different boundary conditions and tissue geometry. Most importantly, we investigated the effect of rough surfaces between ambient medium and the epidermis and between the epidermis and the dermis on the light propagation in the tissues. Both steady-state results and real-time results are presented in this thesis. These studies provide insights on the feasibility of using converging laser beam of nanosecond pulse in the near-infrared region to treat lesions in the dermis layer [Hu, 1995] and point out the importance of surface roughness on determination of the bulk scattering properties of tissue samples.

The simulations of steady-state distribution of photon density have revealed several new features concerning the propagation of converging laser beams in the turbid media of tissues. (1) For one-layer model of skin tissue, the laser irradiance delivered at the focal spot can be much larger than the irradiance elsewhere inside the tissue for $\mu_s d < 10$, where d is the depth of the focal spot below the surface. These situations are desired for treatment of dermal lesions using a converging beam of short laser pulses to reduce collateral tissue damage. (2) The exponential dependence of the unattenuated photon density on the attenuation coefficient requires accurate determination of the coefficients for optimal use of laser radiation in dermatology and plastic surgery. (3) The effect of

surface roughness should be taken into consideration in optical characterization of skin tissues. The simulations of time-resolved distribution of photon density provide the time dependence of the propagation of laser beams with constant power and become useful for study of the transient response of the tissue phantom to a short laser pulse.

The results presented are only an initial part of a long-term research project to investigate and model the propagating of light in turbid media of biological tissues. Further progress remains to be made in the near future: (1) To extend the current limit of simulation on the number of tracked photons, the FORTRAN codes need to be optimized and modified for large-scale parallel computing. This will aid the study of tissue phantoms of large scattering coefficient for imaging applications. (2) The current LCG pseudo-random number generator should be replaced by a scalable parallel LFG pseudo-random number generator to both enhance the performance of the pseudo-random number generator and facilitate the portability of the code. (3) The simulations of light beams with other configurations or with other incident angles are to be conducted in the future. (4) Further development of the tissue model should be conducted for investigation of the interaction between light and various structures inside the tissue and their application in medical imaging.

Figures and Tables

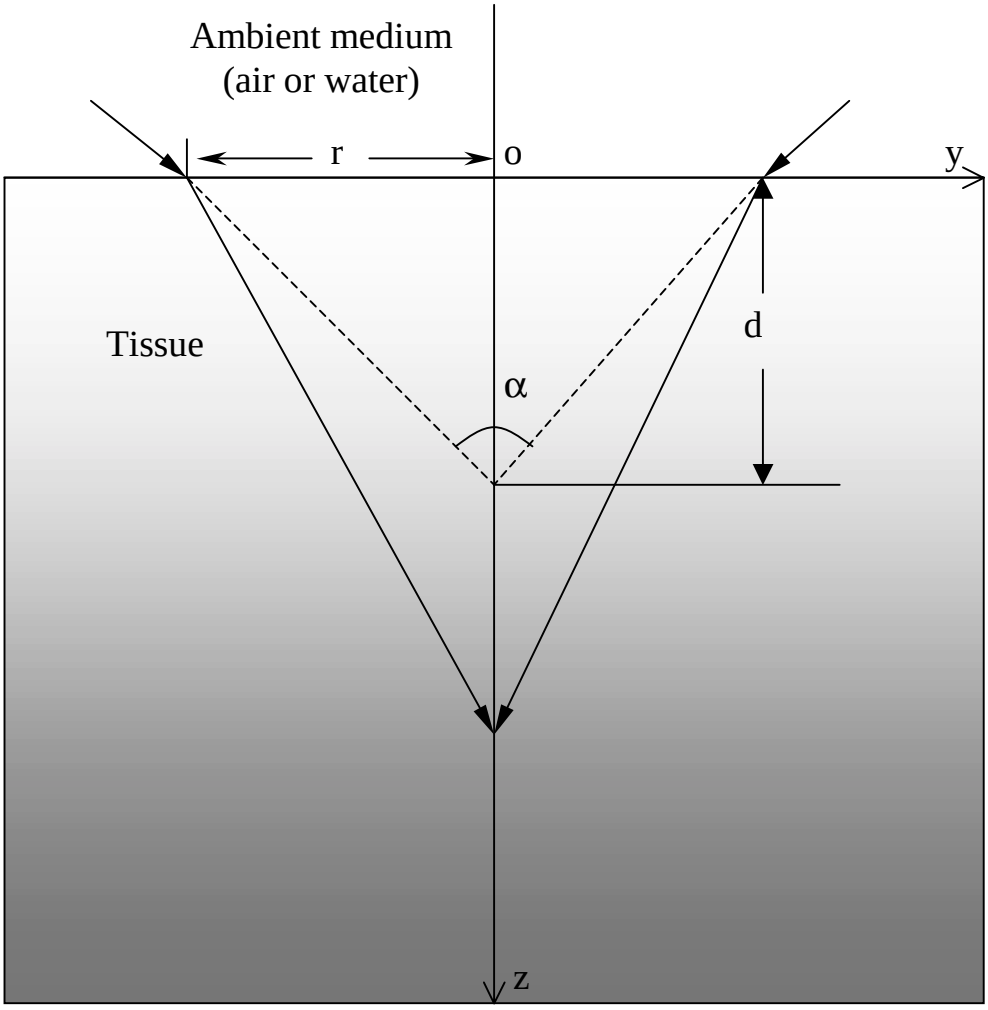

Fig. 1: The geometric configuration of a converging laser beam incident on a skin tissue with $\alpha = 30°$, the e^{-2} radius r = 0.188mm, which is defined at e^{-2} of the central peak, and refractive index of the tissue n = 1.41. All the results of two-layer models and single layer model with rough surface presented in this paper are obtained using this beam configuration with a Gaussian profile and a recording region in the tissue given by $-0.5\text{mm} \le x \text{ (or } y) \le 0.5\text{mm}$ and $0 \le z \le 1.5\text{mm}$.

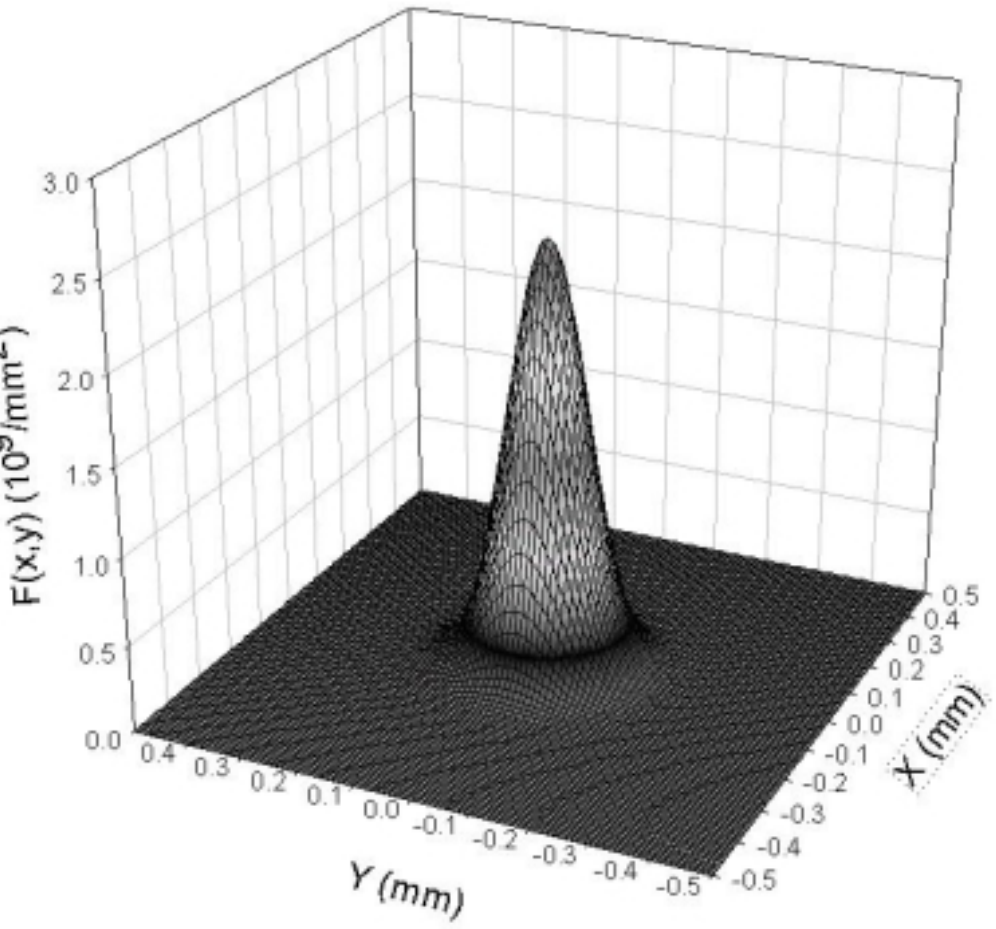

Fig. 2: The 3-d distribution F(x, y) of Gaussian beam in the x-y plane at z=0, the interface between tissue and ambient medium with the e^{-2} radius r of 0.188mm. F(x, y) is counted by photon number per grid cell of volume $8\mu m^3$. with the presumption that the photon number per grid cell of volume $8\mu m^3$ to be 1 at coordinate (x, y) with $\sqrt{x^2 + y^2} = w$.

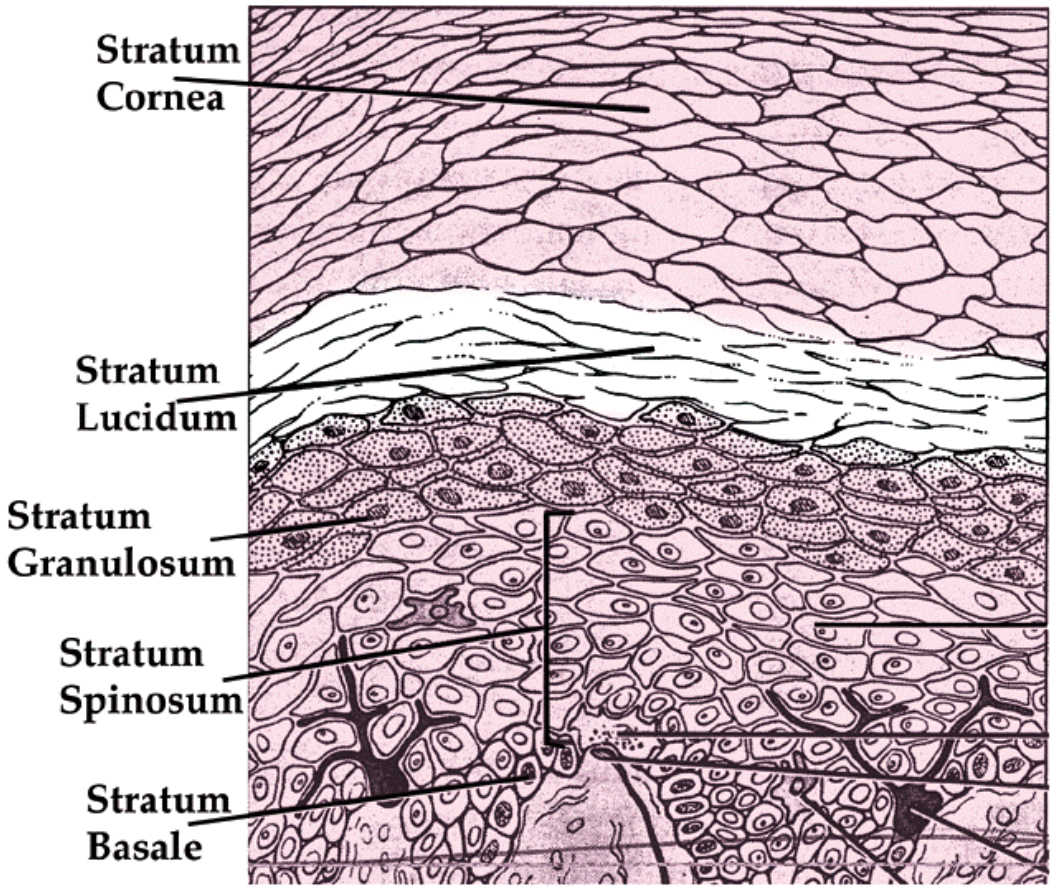

Fig. 3: The cross-section of five sublayers in epidermis layer.

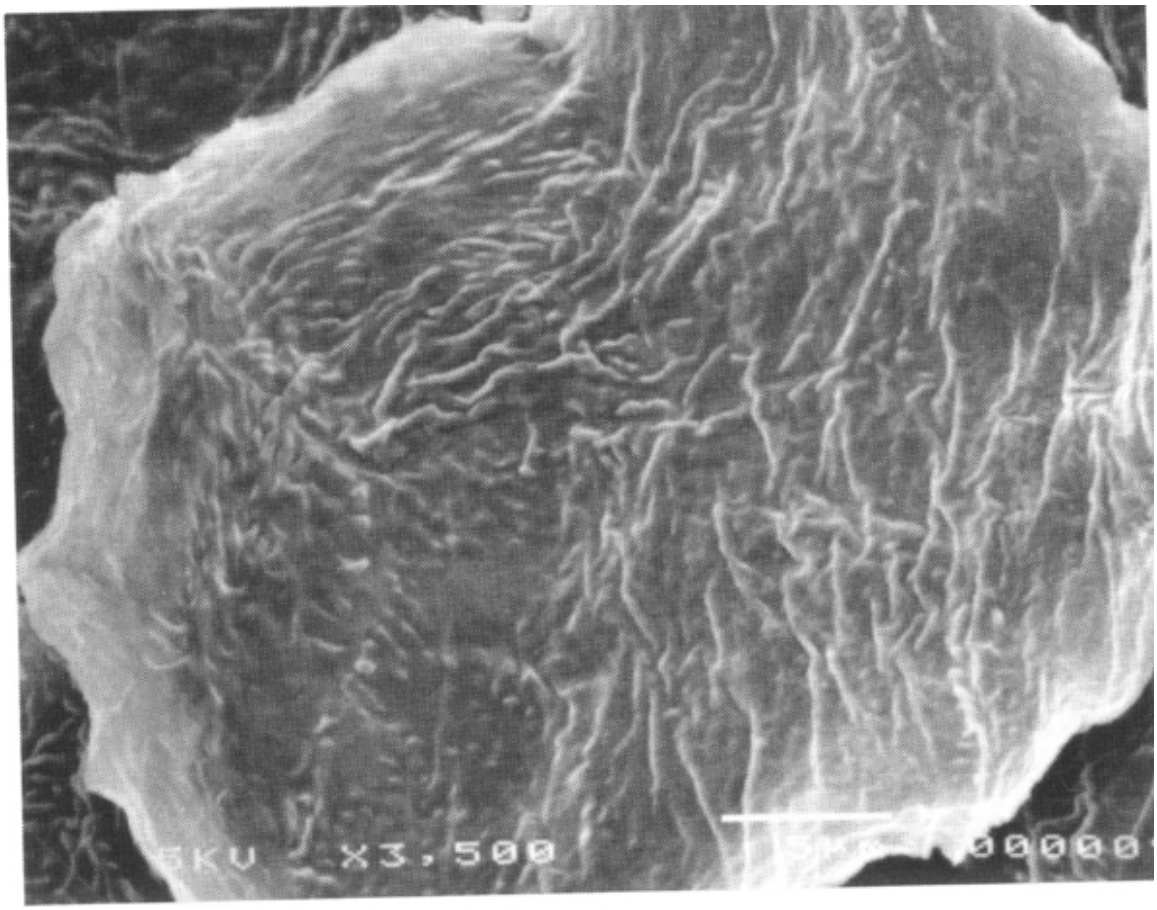

Fig. 4: The 3500x SEM image of single corneocyte in upper stratum corneum of normal human skin.

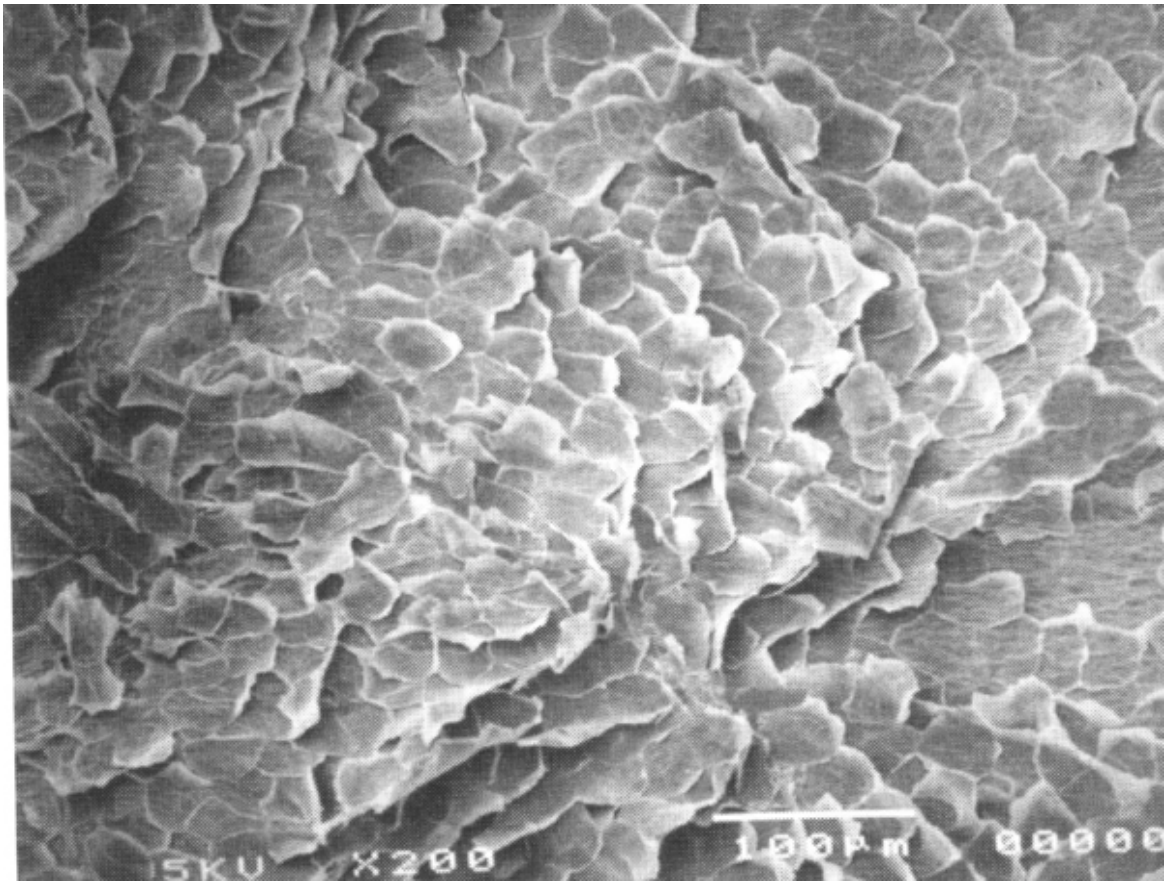

Fig. 5: The 200x SEM image of stacked corneocytes in upper stratum corneum of normal human skin.

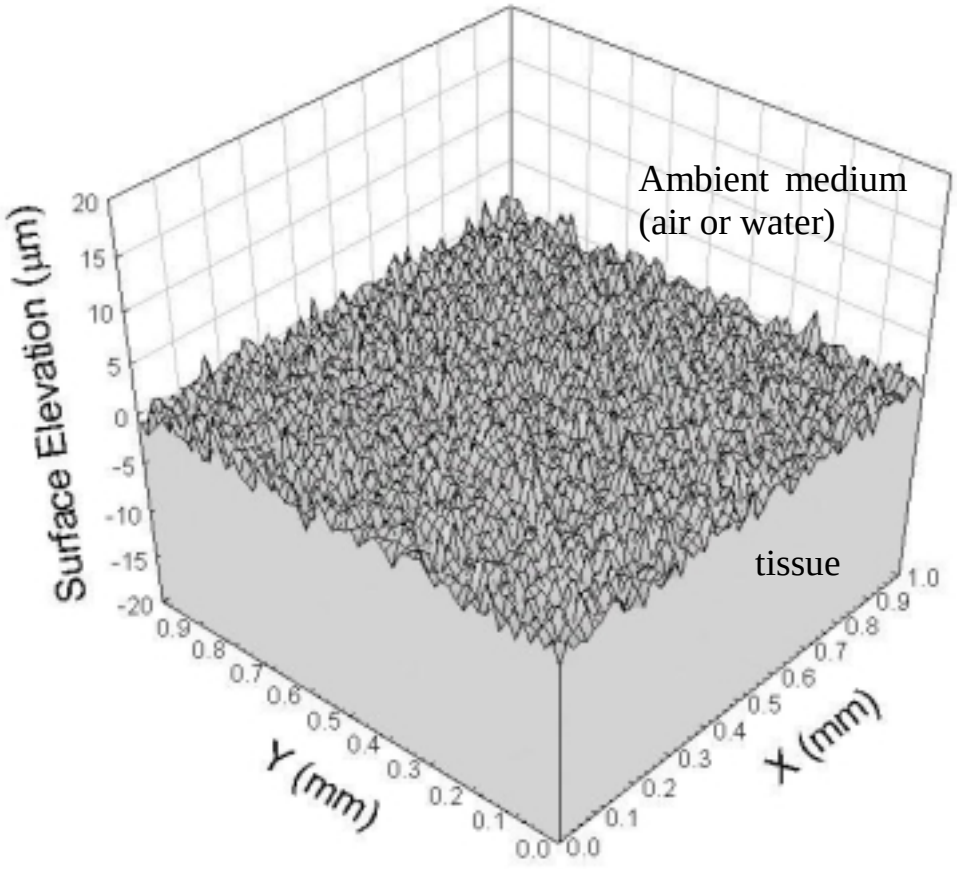

Fig. 6: The profile of rough surface generated at the medium-tissue interface in the x-y plane with the rms height of the surface δ=1μm and the lateral correlation length a=10μm.

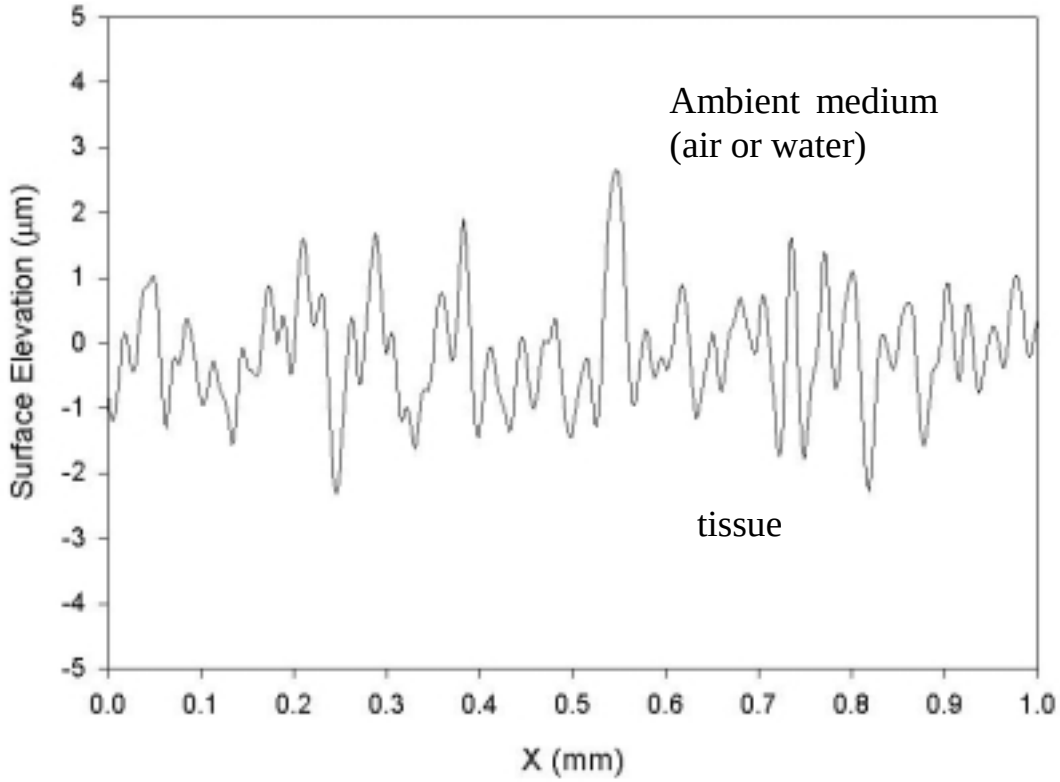

Fig. 7: The cross-section view of the rough surface along the x-axis with the rms height of the surface δ=1μm and the lateral correlation length a=10μm.

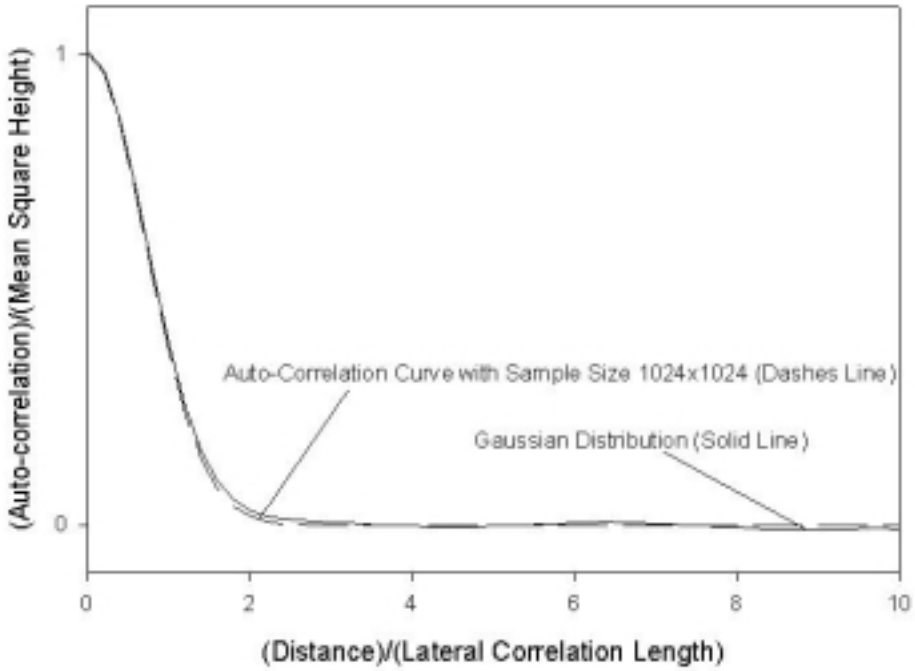

Fig. 8: The comparison of the Gaussian distribution curve to the auto-correlation curve of a rough surface with δ=1μm, a=10μm and sample size is 1024x1024. For the description of the auto-correlation curve, please refer to §3.3.

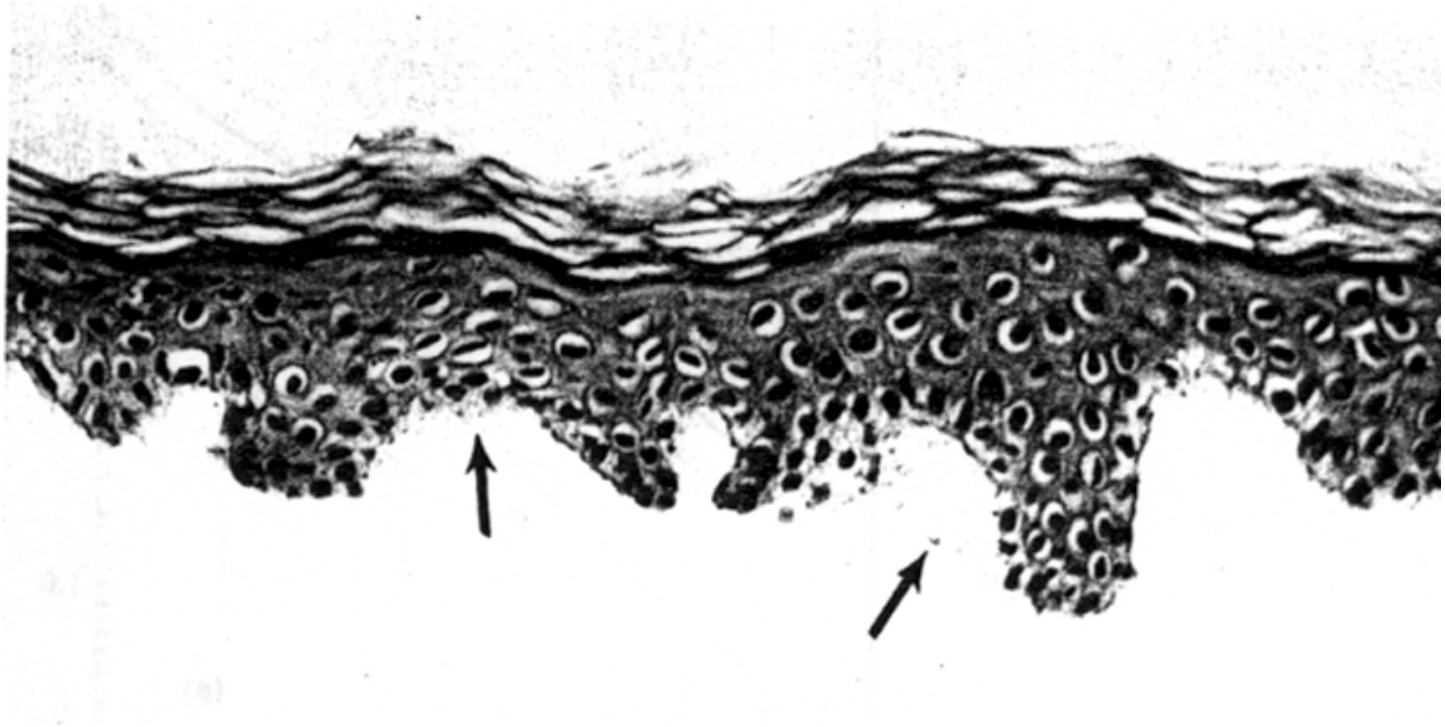

Fig. 9: A typical sample of epidermis after detachment from dermis. (250X)

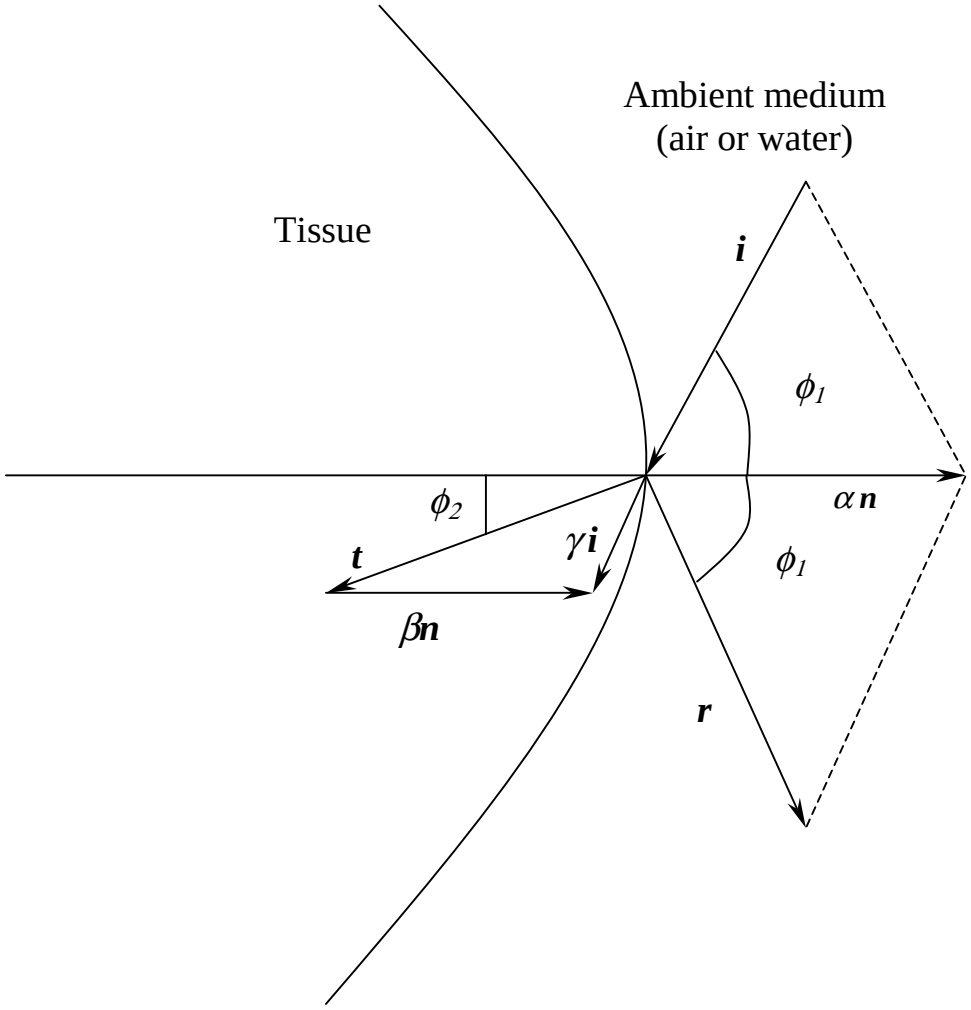

Fig. 10: The illustration of light reflection and refraction at the rough surface. In this plot, ***i*** is the unit vector of incident ray, ***n*** is the unit normal vector of the surface at the incident point of medium-tissue interface, ***r*** is the unit vector of the reflected ray and ***t*** is the unit vector of the refracted ray. The vectors ***i*** and ***r*** are symmetric with respect to ***n*** because of the reflection law with ϕ_1 as the angle of incidence and ϕ_2 as the angle of refraction. The constants α, β, γ are used to represent the proportional relations among the vectors according to geometrical optics.

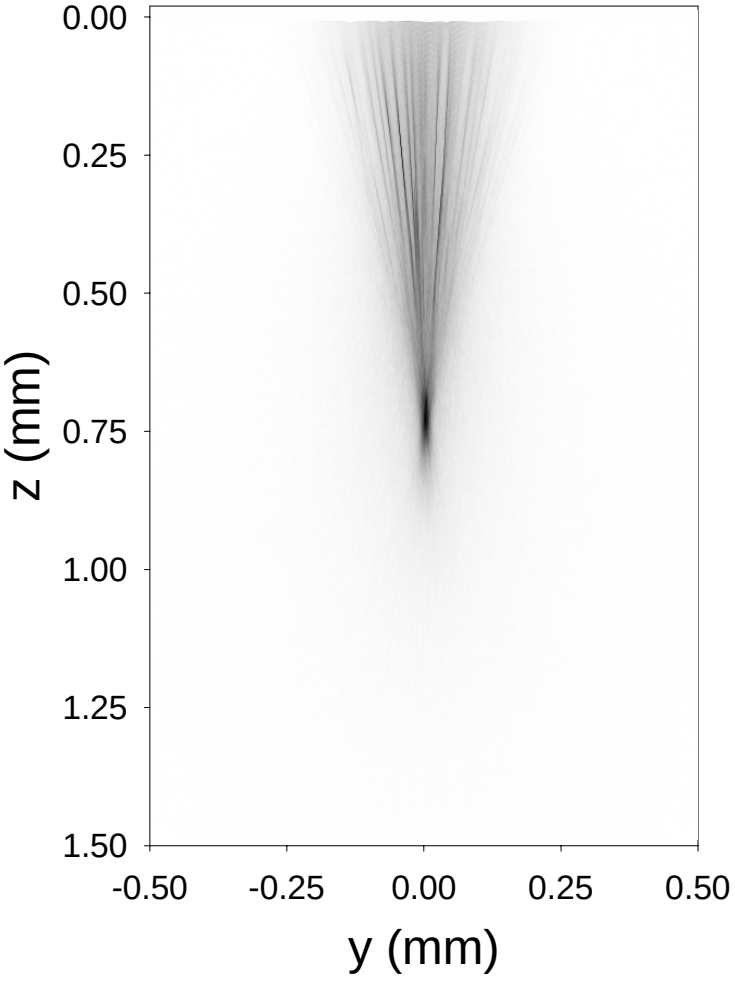

Fig. 11: The gray-scale bitmap image of light distribution in a tissue phantom with rough surface where the gray-scale is linearly proportional to the photon density. Only one randomly rough surface sample is generated to investigate the effect of surface roughness. The rms height of the surface δ=1μm and the lateral correlation length *a*=10μm. For the tissue phantom μ_s=6mm^{-1}, μ_a=0.1mm^{-1}, g=0.9. The simulations were performed on Cray T90 computer.

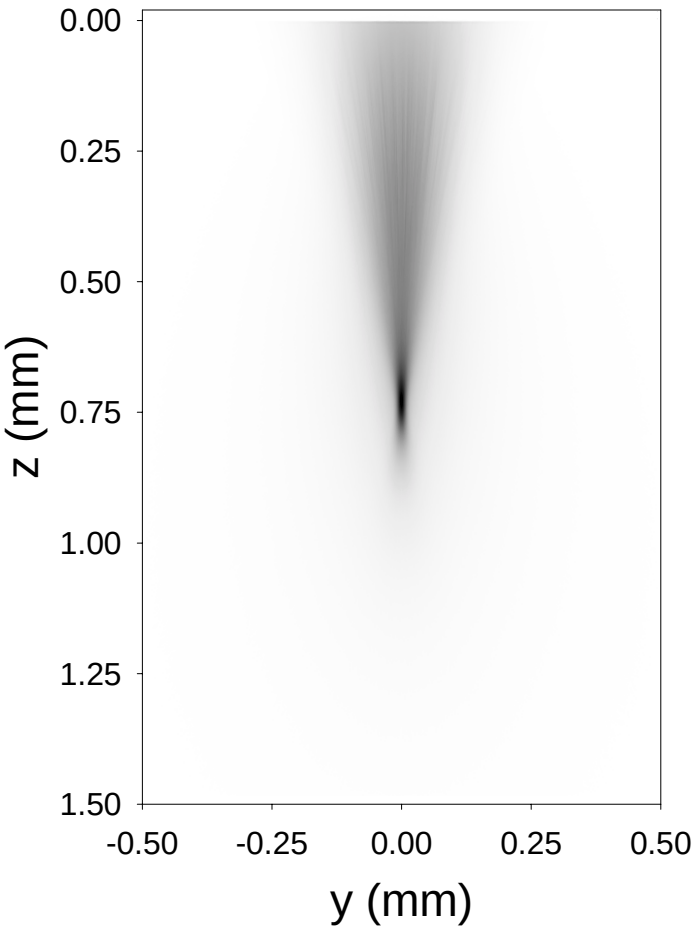

Fig. 12: The gray-scale bitmap image of light distribution in a tissue phantom with rough surface where the gray-scale is linearly proportional to the photon density. One hundred randomly rough surface samples are generated and the results are averaged to investigate the effect of surface roughness. The rms height of the surface δ=1μm and the lateral correlation length a=10μm. For the tissue phantom μ_s=6mm^{-1}, μ_a=0.1mm^{-1}, g=0.9. The simulations were performed on Cray T90 computer.

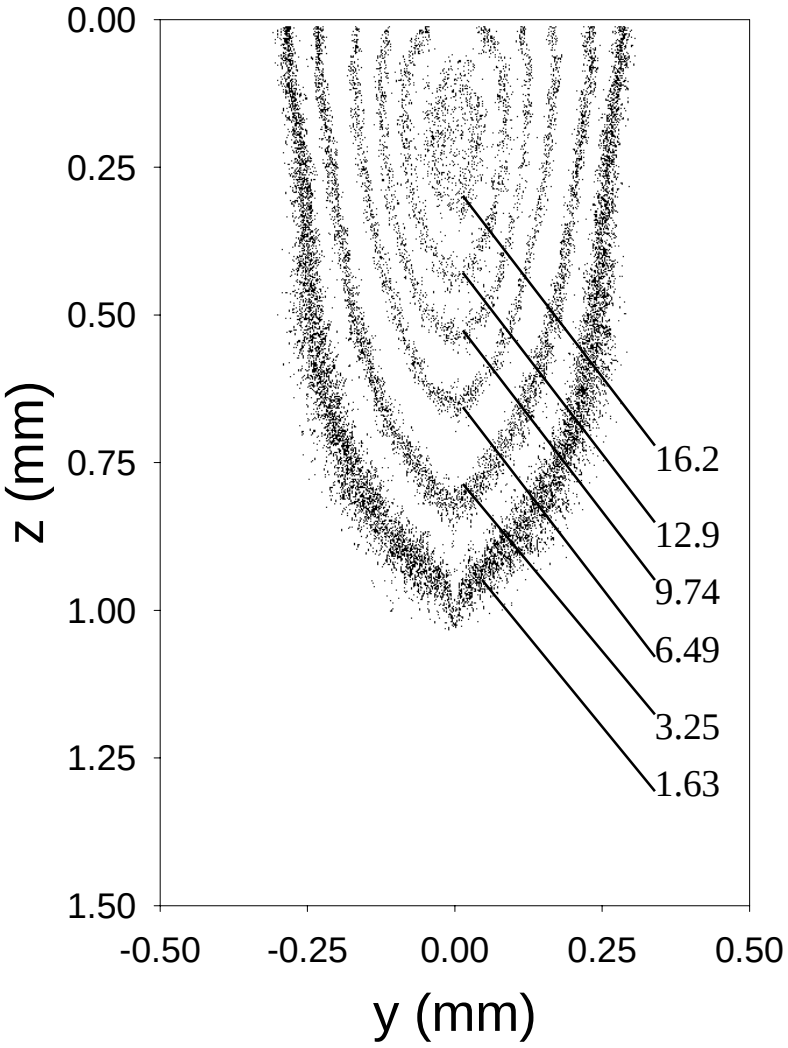

Fig. 13: The contour plot of steady-state light distribution in terms of photon density in the y-z plane of Gaussian beam profile with $\mu_s = 10\text{mm}^{-1}$, $\mu_a = 0.5\text{mm}^{-1}$, g = 0.9 and n=1.41. The photon density of each contour is indicated by the attached number with a standard deviation of ±0.06 in the unit of ($10^{10}/\text{mm}^3$). The simulations were performed on CRAY T90 computer.

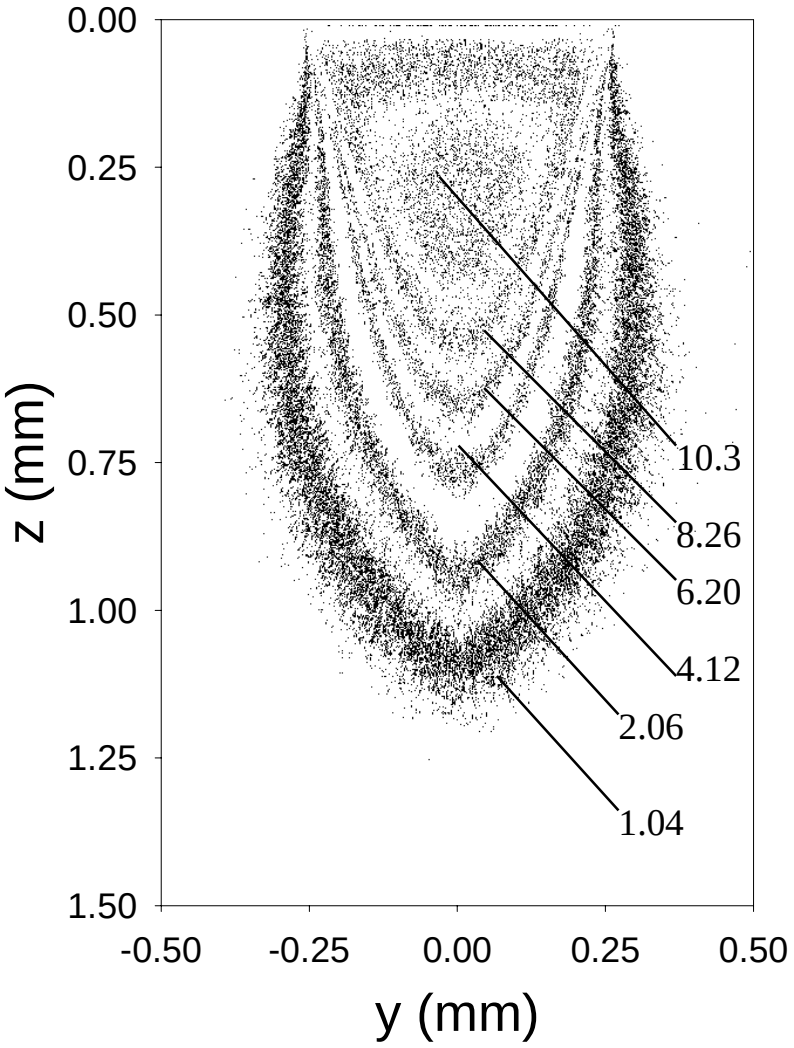

Fig. 14: The contour plot of steady-state light distribution in terms of photon density in the y-z plane of top-hat beam profile with $\mu_s = 10\text{mm}^{-1}$, $\mu_a = 0.5\text{mm}^{-1}$, g = 0.9 and n=1.41. The photon density of each contour is indicated by the attached number with a standard deviation of ±0.06 in the unit of ($10^{10}/\text{mm}^3$). The simulations were performed on CRAY T90 computer.

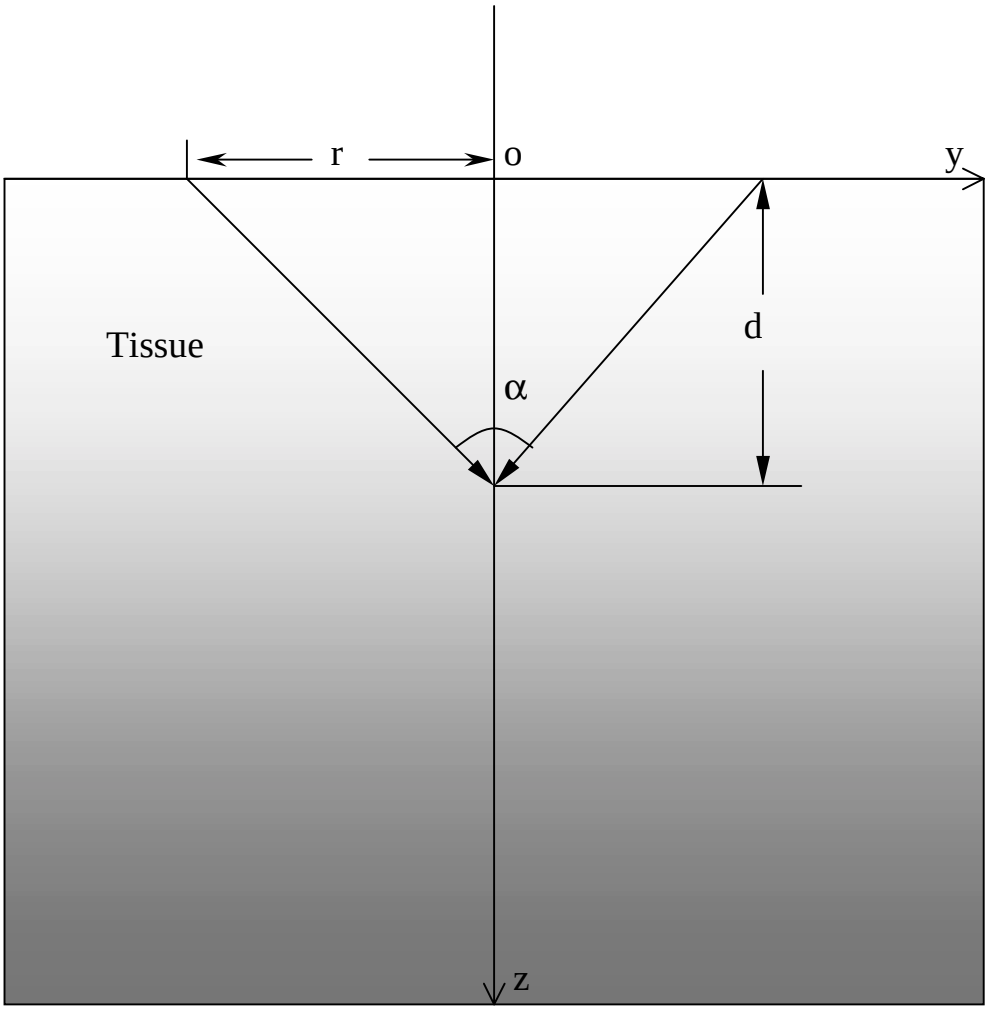

Fig. 15: The geometric configuration of a converging laser beam incident on a skin tissue with $\alpha = 30°$, the e^{-2} radius r = 0.268mm and refractive index of the tissue n = 1.41. The results in Figs. 12 and 13 are obtained using this beam configuration with a Gaussian profile and a recording region in the tissue given by $-0.5 \text{ mm} \le x \text{ (or } y) \le 0.5 \text{ mm}$ and $0 \le z \le 1.5$ mm.

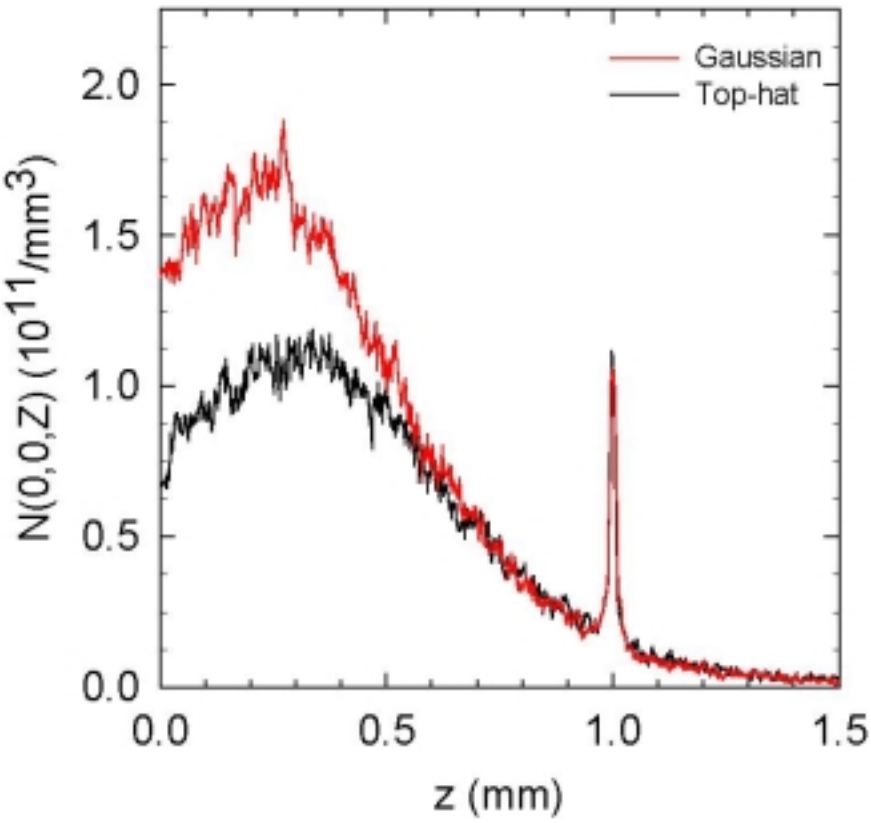

Fig. 16: Comparison of the photon density along the z-axis in a linear plot for Gaussian beam profile and top-hat beam profile with the e^{-2} radius r = 0.268mm. The simulations were performed on Cray T90 computer.

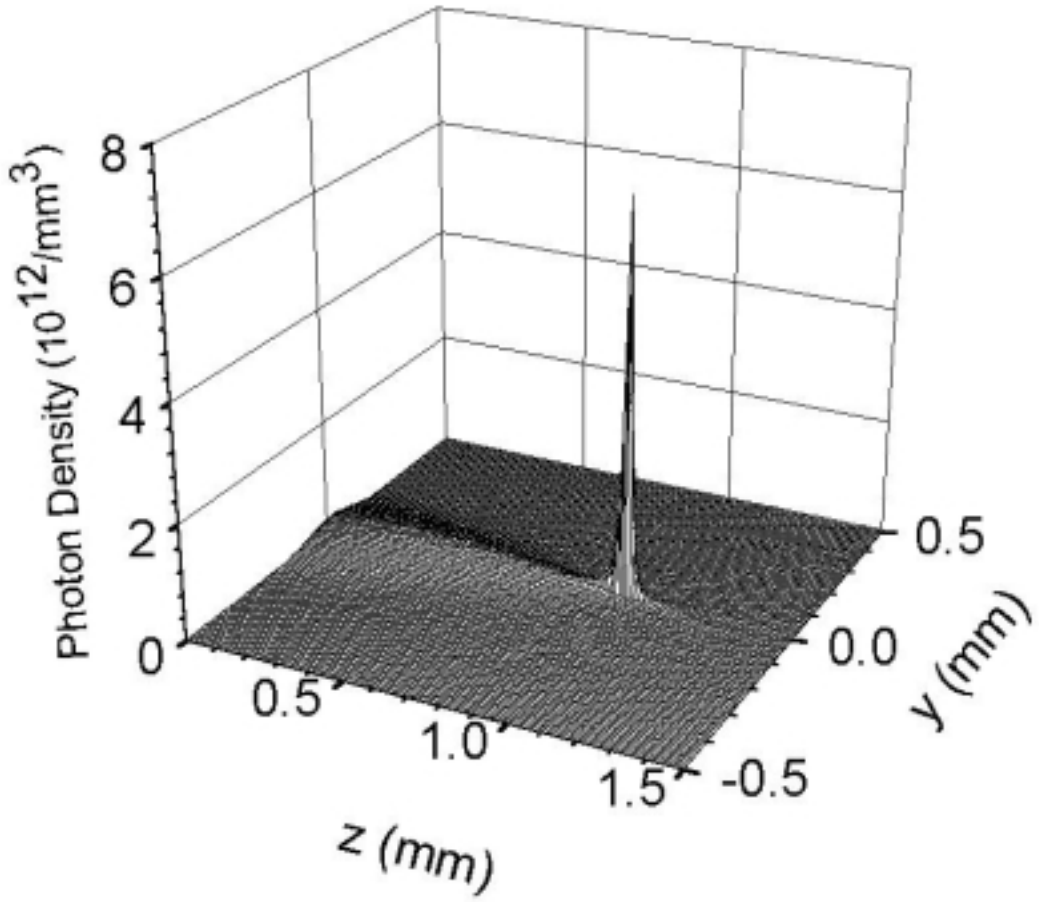

Fig. 17: The photon density is plotted in the y-z plane inside the tissue phantom with μ_s = 6mm^{-1}, μ_a = 0.1mm^{-1}, g = 0.9 and n=1.41. The simulations were performed on Cray T90 computer.

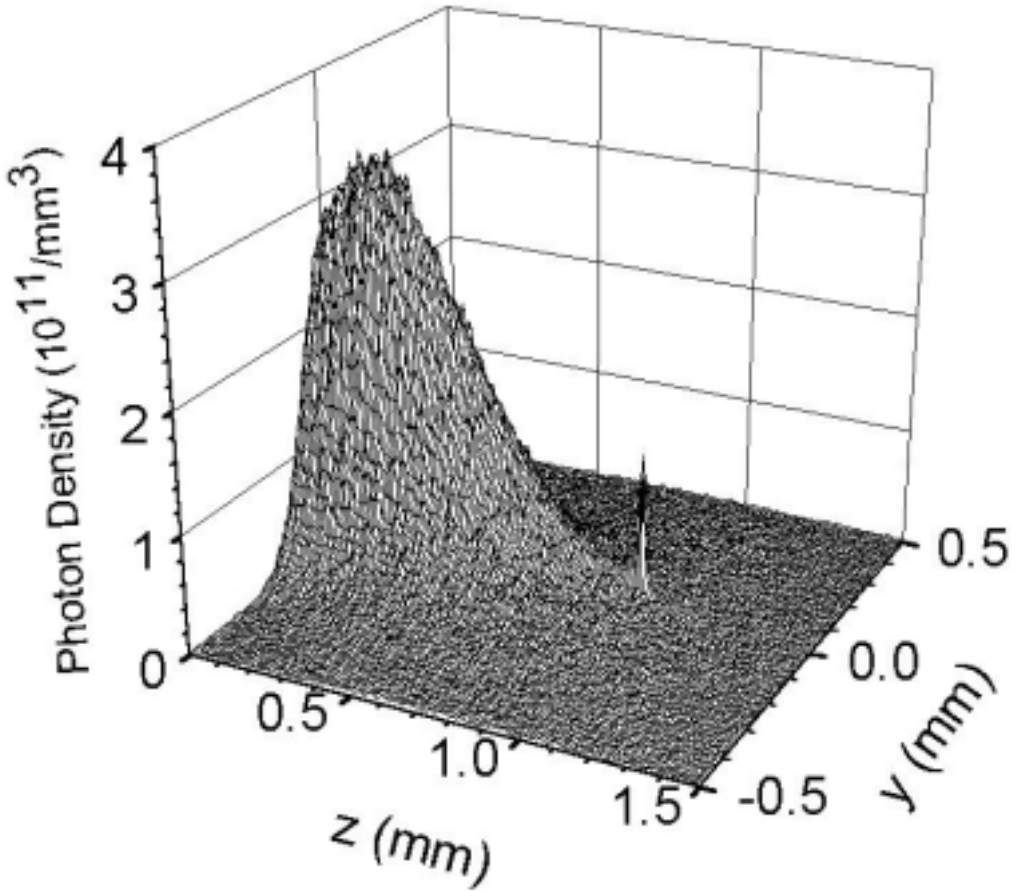

Fig. 18: The photon density is plotted in the y-z plane inside the tissue phantom with μ_s = 10mm^{-1}, μ_a = 0.1mm^{-1}, g = 0.9 and n=1.41. The simulations were performed on Cray T90 computer.

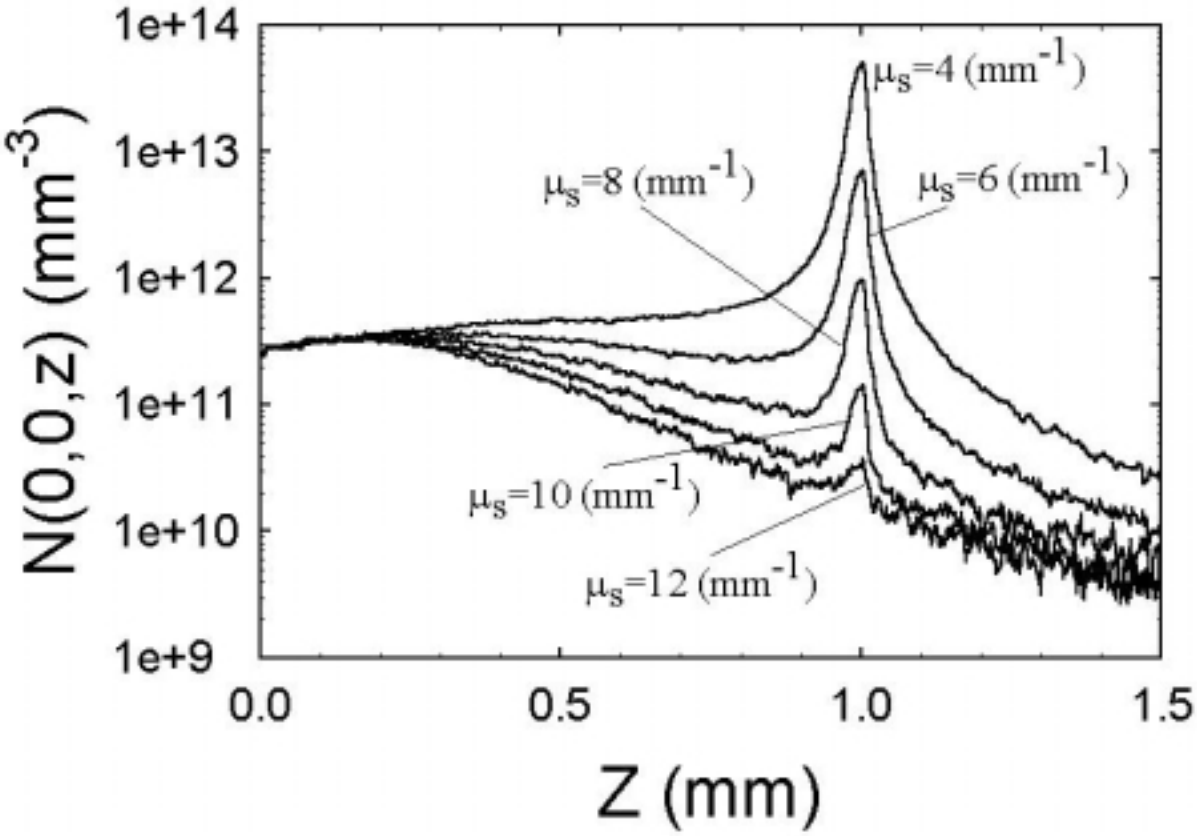

Fig. 19: The photon density distribution along the z-axis in a semi-log plot for different values of μ_s with $\mu_a = 0.1 mm^{-1}$, g = 0.9 and n=1.41. The simulations were performed on Cray T90 computer.

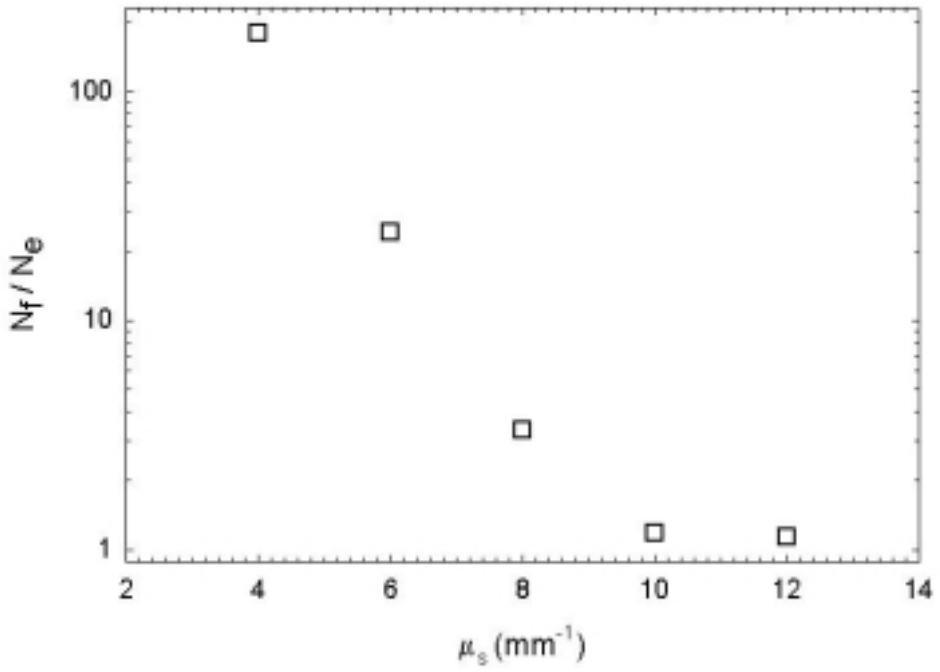

Fig. 20: The ratio of N_f / N_e is shown as a function of μ_s with $\mu_a = 0.1\text{mm}^{-1}$, g = 0.9 and n=1.41. The simulations were performed on Cray T90 computer.

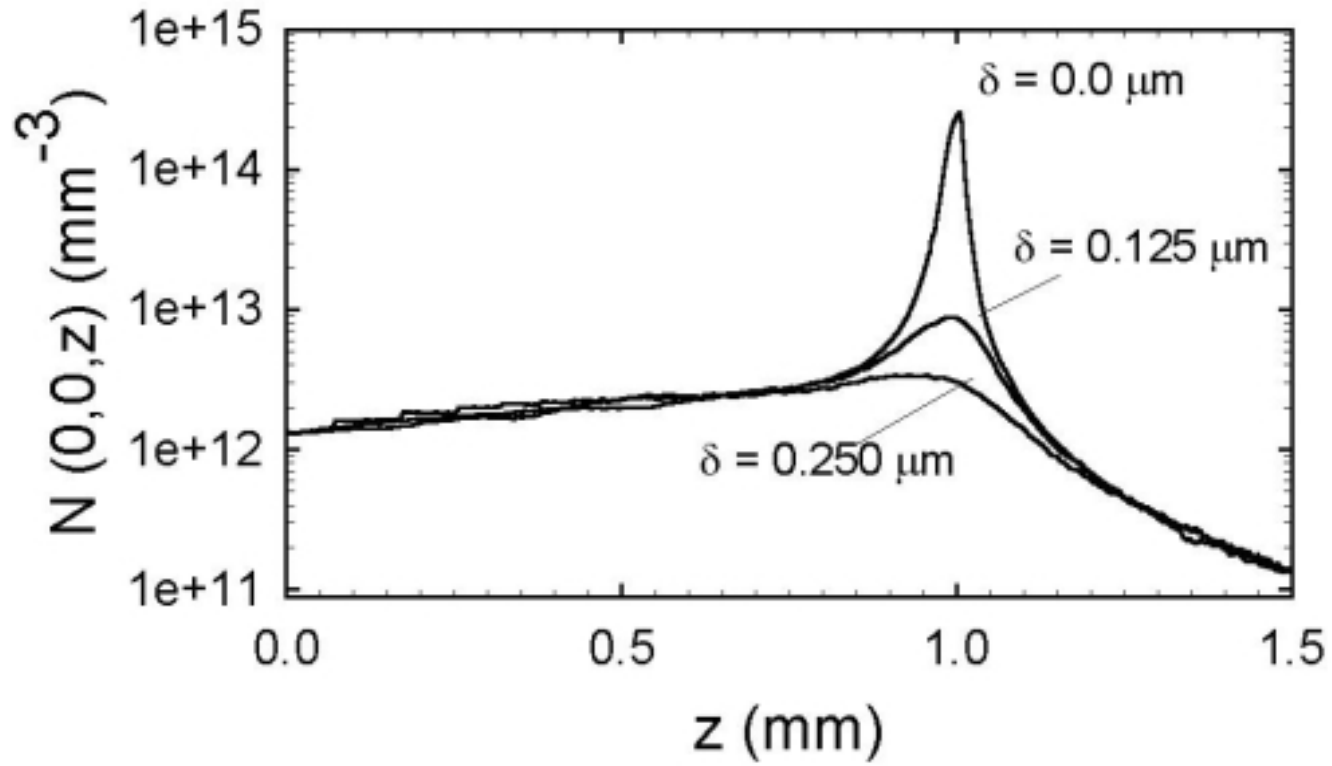

Fig. 21: The photon density distribution along the z-axis in a semi-log plot for different values of surface elevation δ with $\mu_a = 0.1 mm^{-1}$, g = 0.9 and n=1.41. The profile of the rough air-tissue interface is characterized by δ = 0.125μm and 0.250μm with the same *a* = 10.0 μm. The simulations were performed on Compaq Desktop2000 computer.

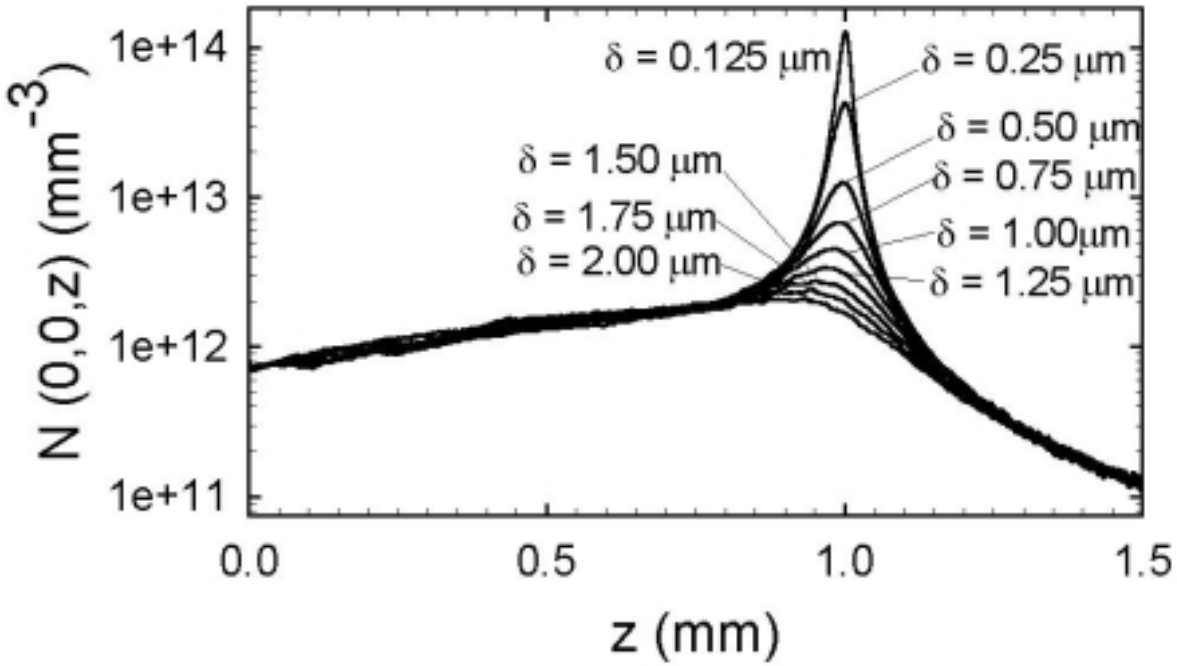

Fig. 22: The photon density distribution along the z-axis in a semi-log plot for different values of surface elevation δ with μ_a = 0.1mm^{-1}, g = 0.9 and n=1.41. The profile of the rough water-tissue interface is characterized by ranging δ from 0.125μm to 2.00μm with the same *a* = 10.0μm. The simulations were performed on Compaq Desktop2000 computer.

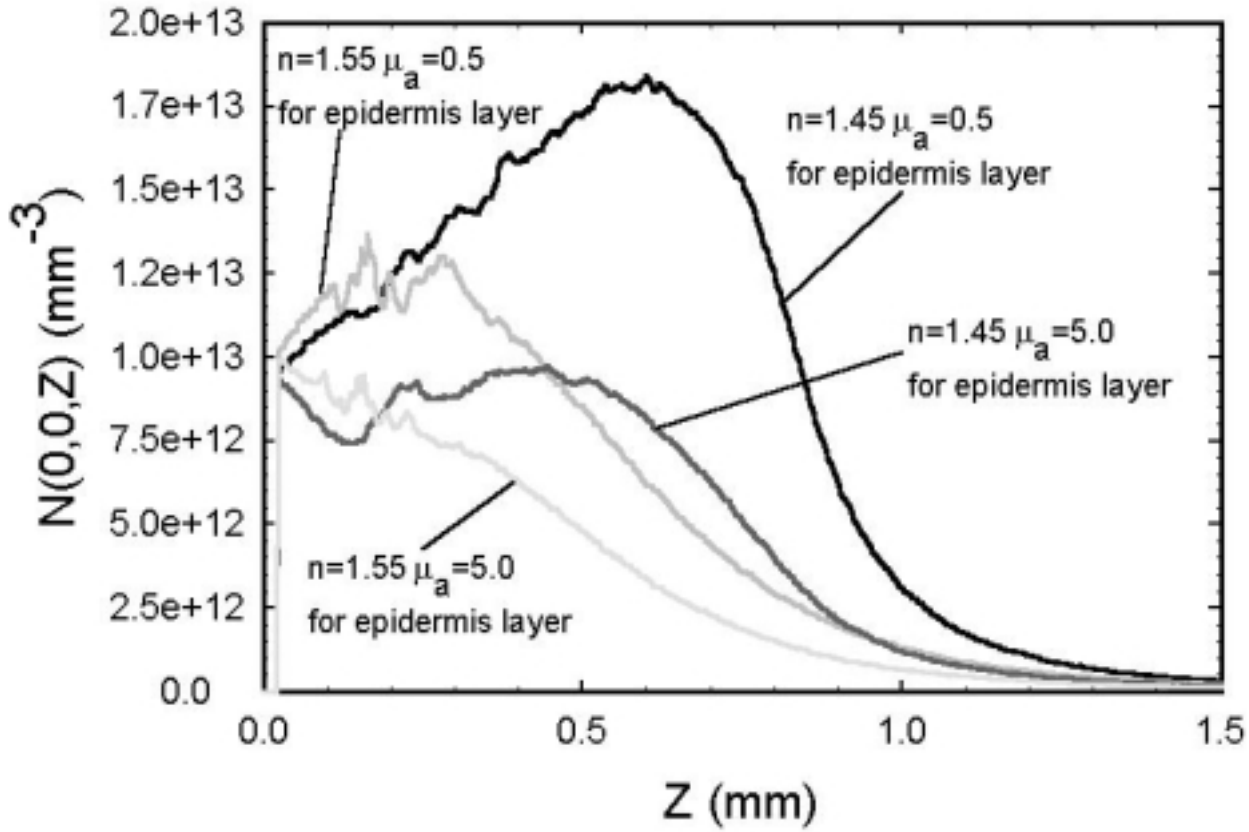

Fig. 23: The photon density distribution along the z-axis in a linear plot for different values of n=1.41 and n=1.55 and different values of μ_a=5.0 and μ_a=0.5 for epidermis layer. The simulations were performed on SGI Origin 2000 computer.

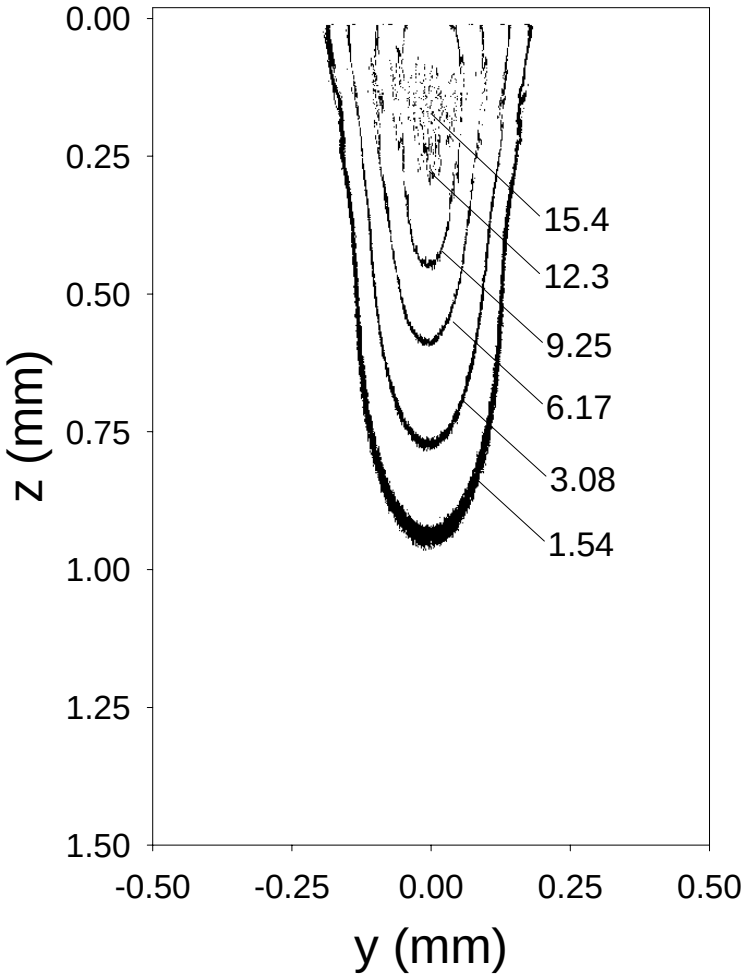

Fig. 24: The contour plot of light distribution in terms of photon density in the y-z plane inside the two-layer tissue phantom with $\mu_s = 6mm^{-1}$, $\mu_a = 0.5mm^{-1}$, g = 0.9 and n=1.55 for the epidermis layer, and $\mu_s = 4mm^{-1}$, $\mu_a = 0.5mm^{-1}$, g = 0.9 and n=1.41 for the dermis layer. The photon density of each contour is indicated by the attached number with a standard deviation of ±0.06 in the unit of ($10^{12}/mm^3$). The simulations were performed on SGI Origin 2000 computer.

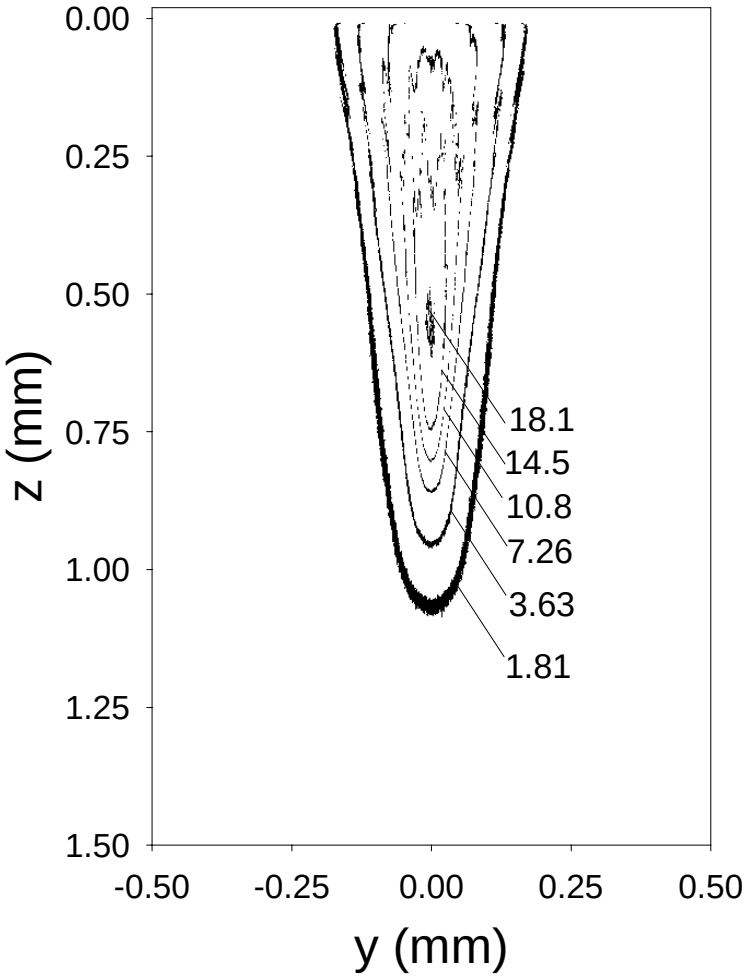

Fig. 25: The contour plot of light distribution in terms of photon density in the y-z plane inside the two-layer tissue phantom with $\mu_s = 6mm^{-1}$, $\mu_a = 0.5mm^{-1}$, g = 0.9 and n=1.45 for the epidermis layer, and $\mu_s = 4mm^{-1}$, $\mu_a = 0.5mm^{-1}$, g = 0.9 and n=1.41 for the dermis layer. The photon density of each contour is indicated by the attached number with a standard deviation of ±0.06 in the unit of ($10^{12}/mm^3$). The simulations were performed on SGI Origin 2000 computer.

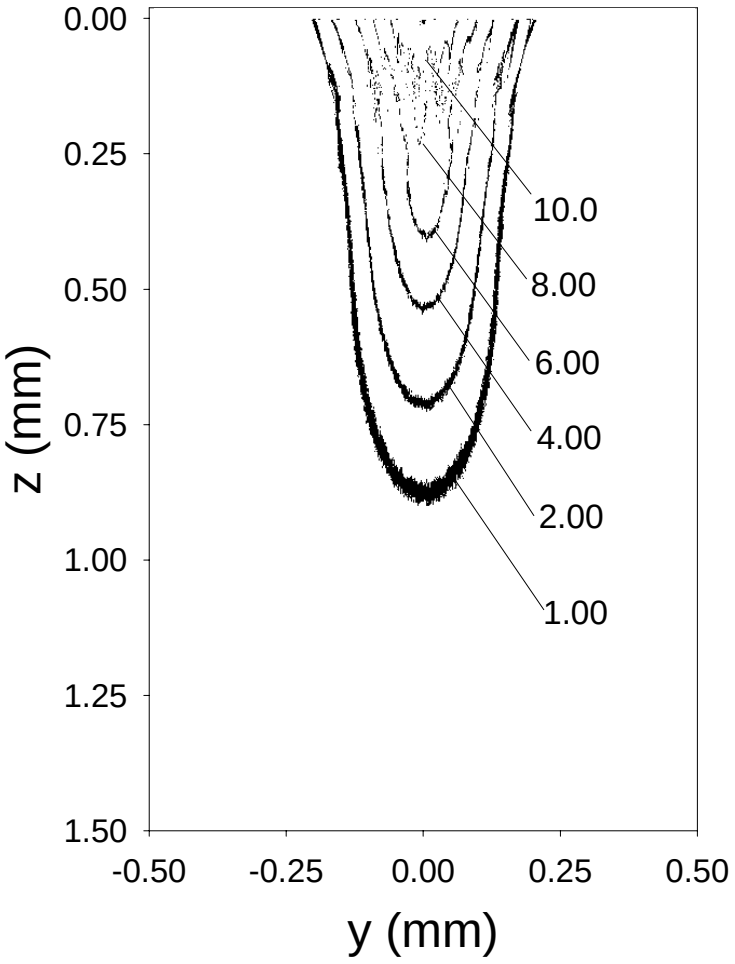

Fig. 26: The contour plot of light distribution in terms of photon density in the y-z plane inside the two-layer tissue phantom with $\mu_s = 6mm^{-1}$, $\mu_a = 5.0mm^{-1}$, g = 0.9 and n=1.55 for the epidermis layer, and $\mu_s = 4mm^{-1}$, $\mu_a = 0.5mm^{-1}$, g = 0.9 and n=1.41 for the dermis layer. The photon density of each contour is indicated by the attached number with a standard deviation of ±0.06 in the unit of ($10^{12}/mm^3$). The simulations were performed on SGI Origin 2000 computer.

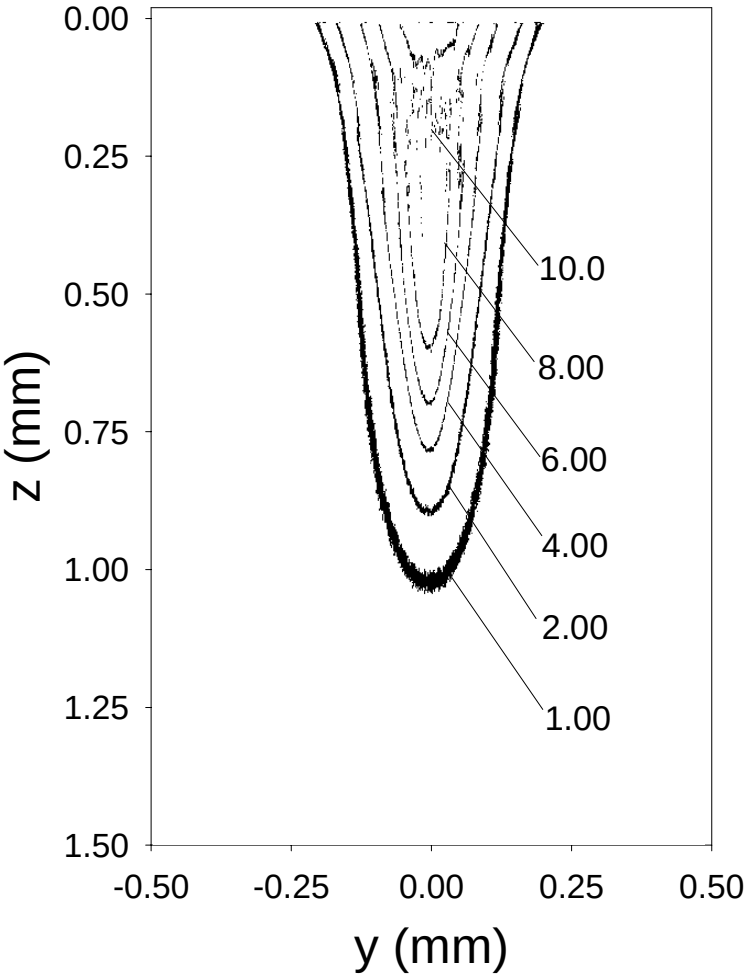

Fig. 27: The contour plot of light distribution in terms of photon density in the y-z plane inside the two-layer tissue phantom with $\mu_s = 6mm^{-1}$, $\mu_a = 5.0mm^{-1}$, g = 0.9 and n=1.45 for the epidermis layer, and $\mu_s = 4mm^{-1}$, $\mu_a = 0.5mm^{-1}$, g = 0.9 and n=1.41 for the dermis layer. The photon density of each contour is indicated by the attached number with a standard deviation of ±0.06 in the unit of ($10^{12}/mm^3$). The simulations were performed on SGI Origin 2000 computer.

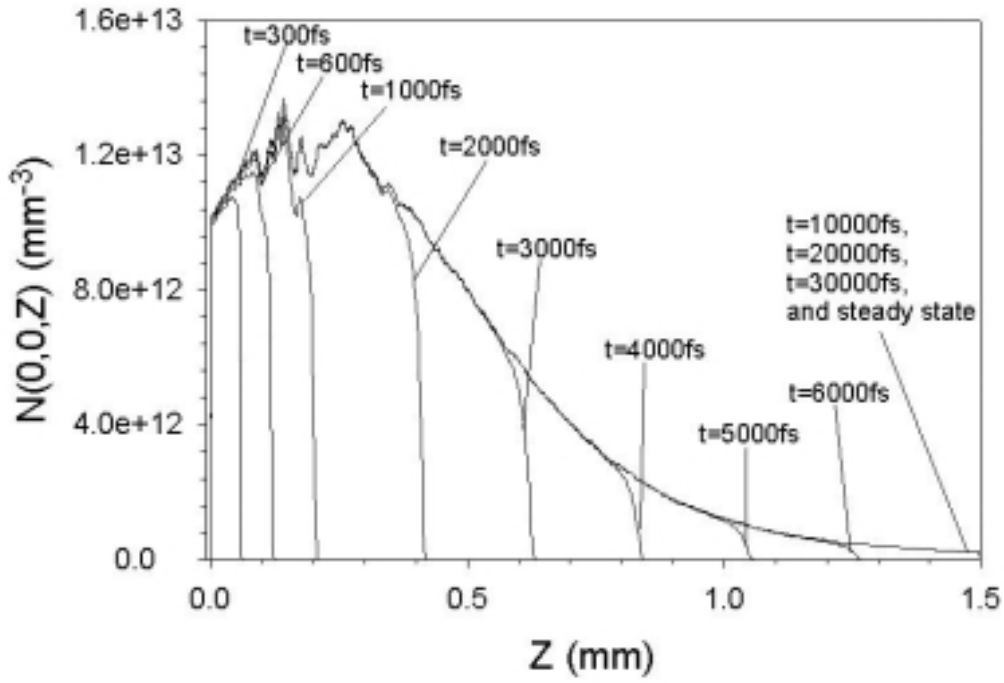

Fig. 28: The time-resolved distribution of photon density N along the z-axis at different time after the photon is injected a constant rate starting from t=0fs. The total tracked number of photons was kept the same in all results and given by $N_0 = 3.8\times10^8$. The configuration for tissue layers is $\mu_s = 6mm^{-1}$, $\mu_a = 0.5mm^{-1}$, g = 0.9 and n=1.55 for the epidermis layer, and $\mu_s = 4mm^{-1}$, $\mu_a = 0.5mm^{-1}$, g = 0.9 and n=1.41 for the dermis layer. The simulations were performed on SGI Origin 2000 computer.

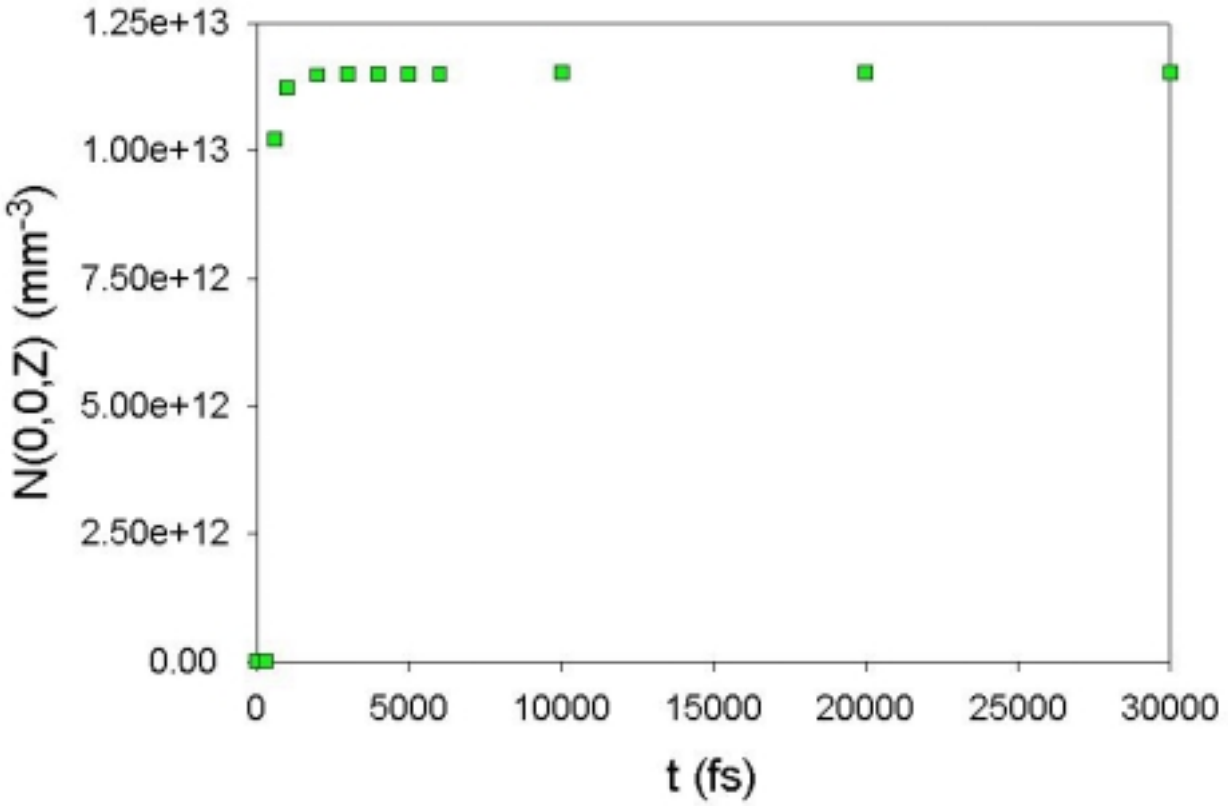

Fig. 29: The time evolution of photon number on the z-axis at z=0.1mm, where the epidermis-dermis junction is located. The total tracked number of photons was kept the same in all results and given by $N_0 = 3.8\times10^8$. The tissue configuration is the same as Fig. 28. The simulations were performed on SGI Origin 2000 computer.

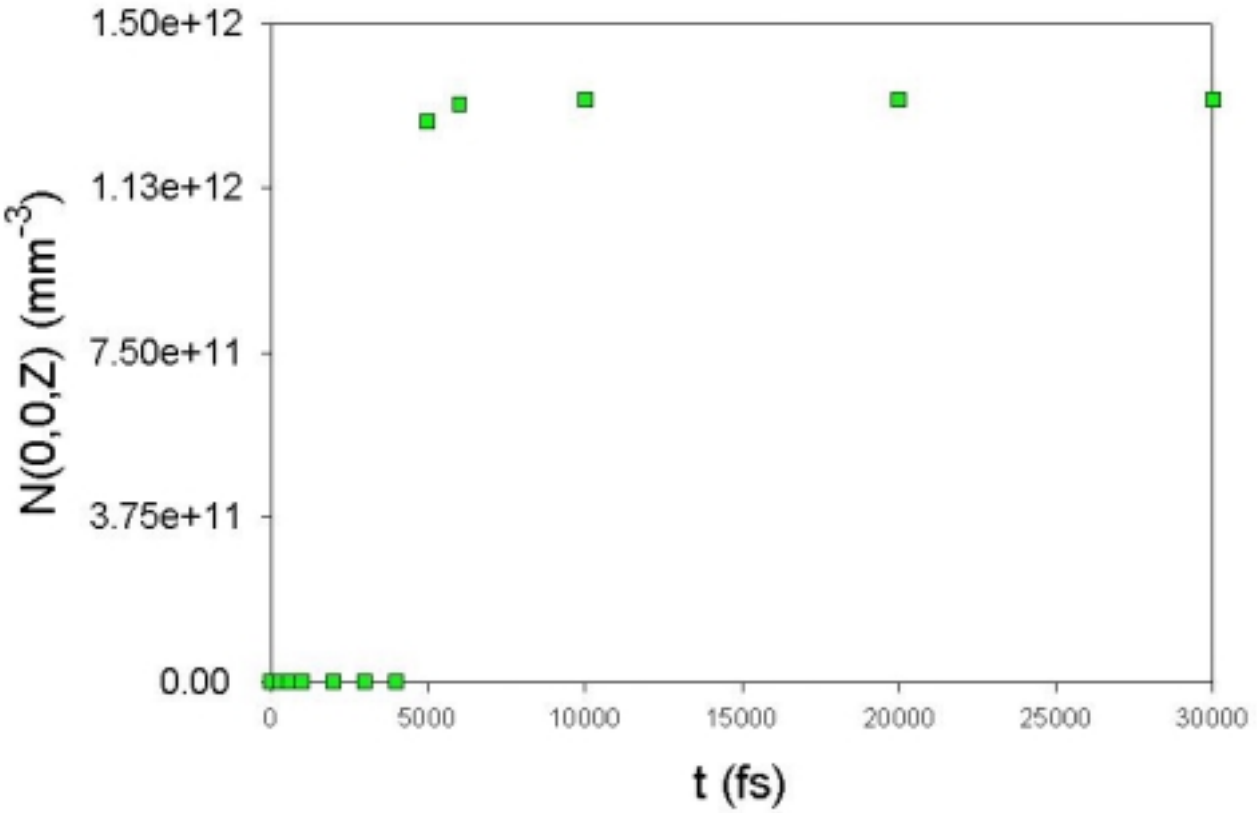

Fig. 30: The time evolution of photon number on the z-axis at z=1.0mm. The total tracked number of photons was kept the same in all results and given by $N_0 = 3.8\times10^8$. The tissue configuration is the same as Fig. 28. The simulations were performed on SGI Origin 2000 computer.

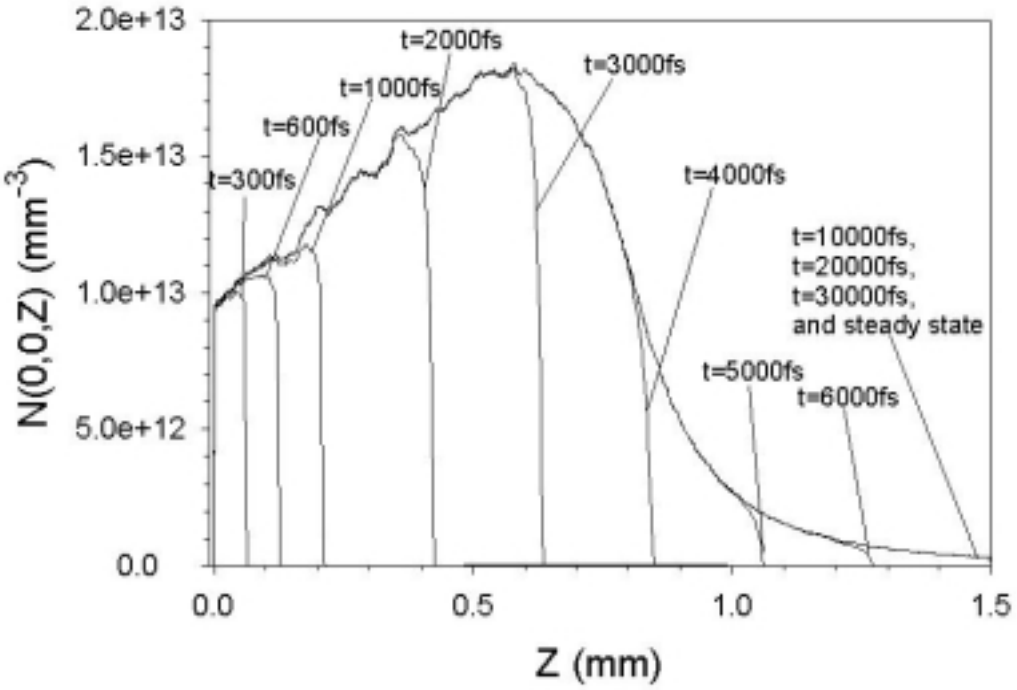

Fig. 31: The time-resolved distribution of photon density N along the z-axis in a linear plot for different time point after the photon is injected at a constant rate starting from t=0fs. The total tracked number of photons was kept the same in all results and given by $N_0 = 3.8\times10^8$. The configuration for tissue layers is $\mu_s = 6mm^{-1}$, $\mu_a = 0.5mm^{-1}$, g = 0.9 and n=1.45 for the epidermis layer, and $\mu_s = 4mm^{-1}$, $\mu_a = 0.5mm^{-1}$, g = 0.9 and n=1.41 for the dermis layer. The simulations were performed on SGI Origin 2000 computer.

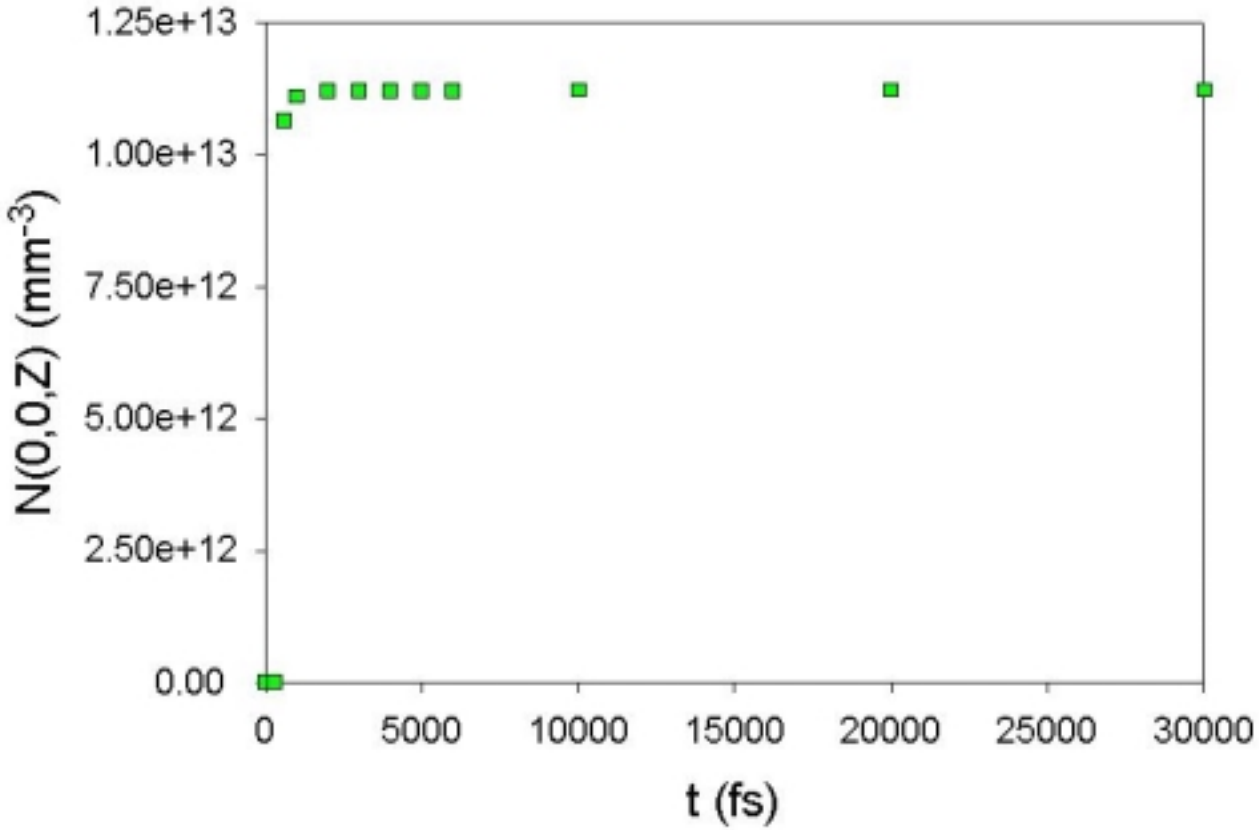

Fig. 32: The time evolution of photon number on the z-axis at z=0.1mm, where the epidermis-dermis junction is located. The total tracked number of photons was kept the same in all results and given by $N_0 = 3.8\times10^8$. The tissue configuration is the same as Fig. 31. The simulations were performed on SGI Origin 2000 computer..

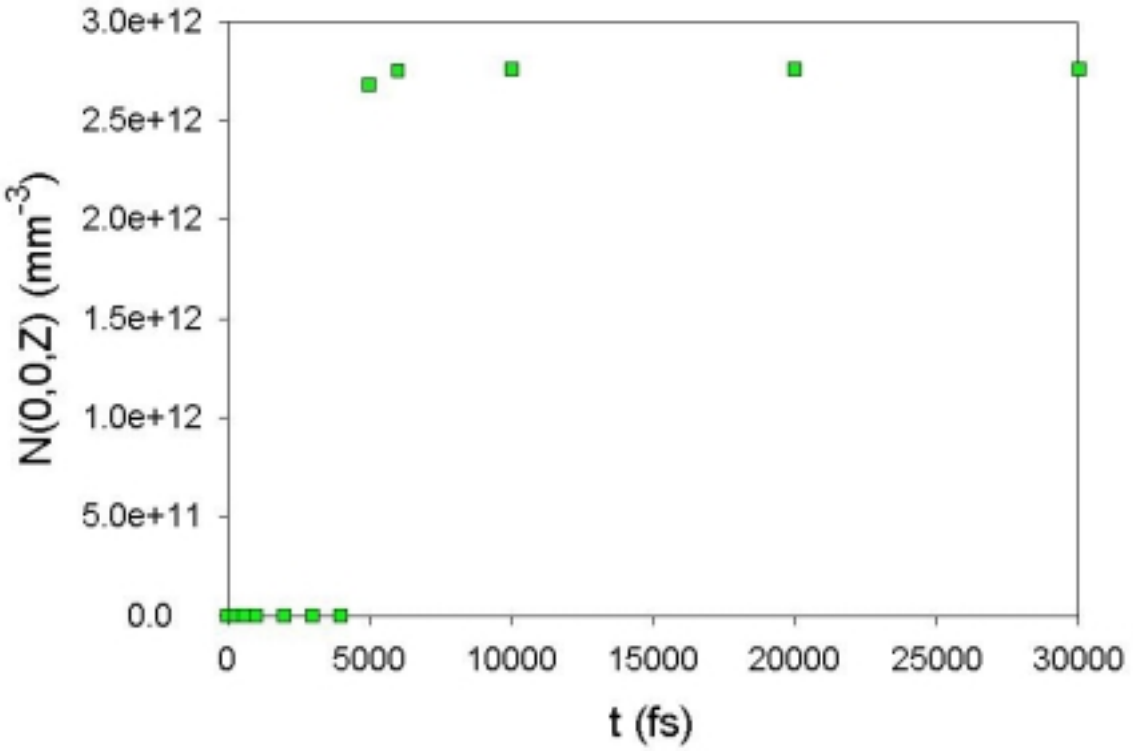

Fig. 33: The time evolution of photon number on the z-axis at z=1.0mm. The total tracked number of photons was kept the same in all results and given by $N_0 = 3.8\times10^8$. The tissue configuration is the same as Fig. 31. The simulations were performed on SGI Origin 2000 computer.

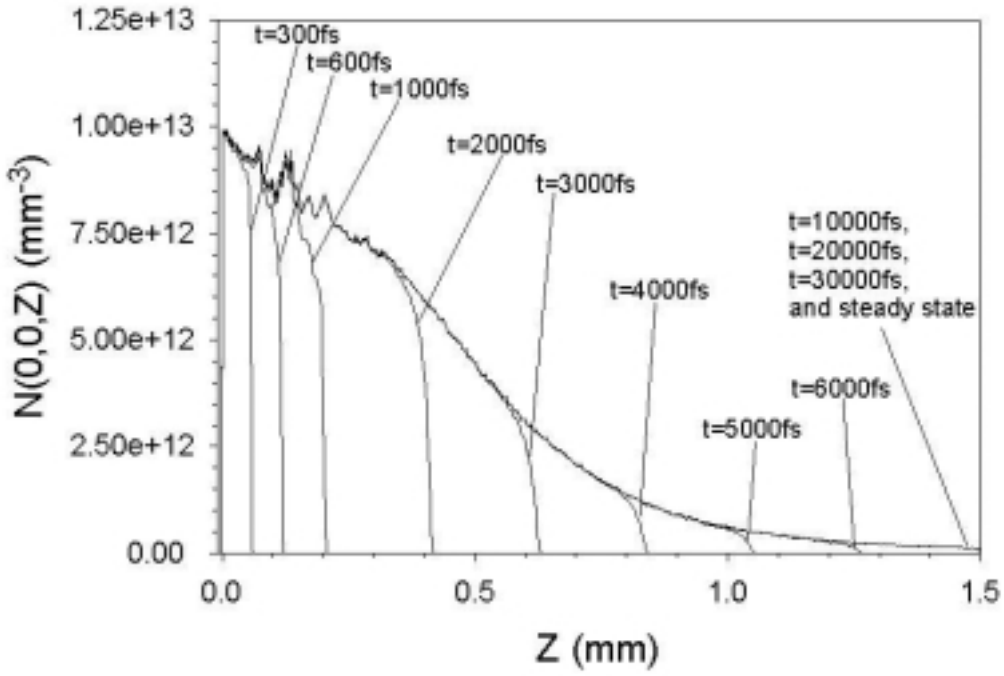

Fig. 34: The time-resolved distribution of photon density N along the z-axis in a linear plot for different time point after the photon is injected at a constant rate starting from t=0fs. The total tracked number of photons was kept the same in all results and given by $N_0 = 3.8\times10^8$. The configuration for tissue layers is $\mu_s = 6mm^{-1}$, $\mu_a = 5.0mm^{-1}$, g = 0.9 and n=1.55 for the epidermis layer, and $\mu_s = 4mm^{-1}$, $\mu_a = 0.5mm^{-1}$, g = 0.9 and n=1.41 for the dermis layer. The simulations were performed on SGI Origin 2000 computer.

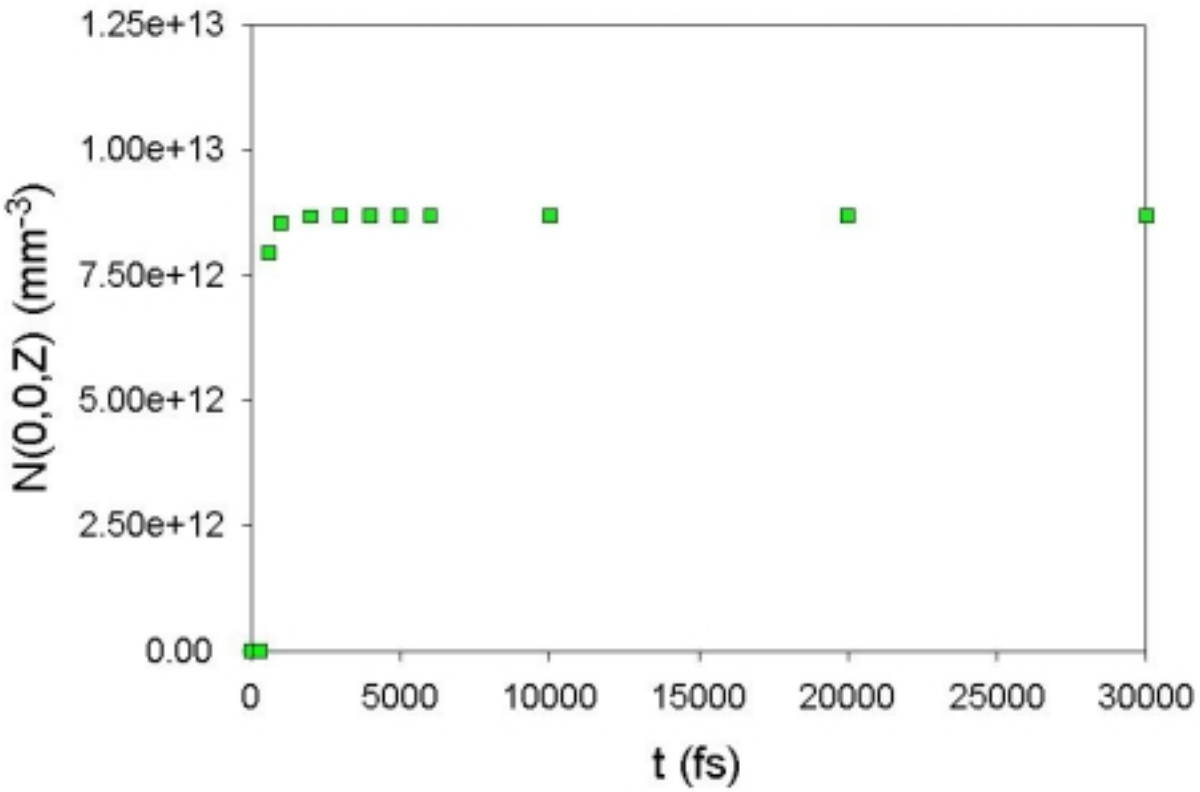

Fig. 35: The time evolution of photon number on the z-axis at z=0.1mm, where the epidermis-dermis junction is located. The total tracked number of photons was kept the same in all results and given by $N_0 = 3.8\times10^8$. The tissue configuration is the same as Fig. 34. The simulations were performed on SGI Origin 2000 computer..

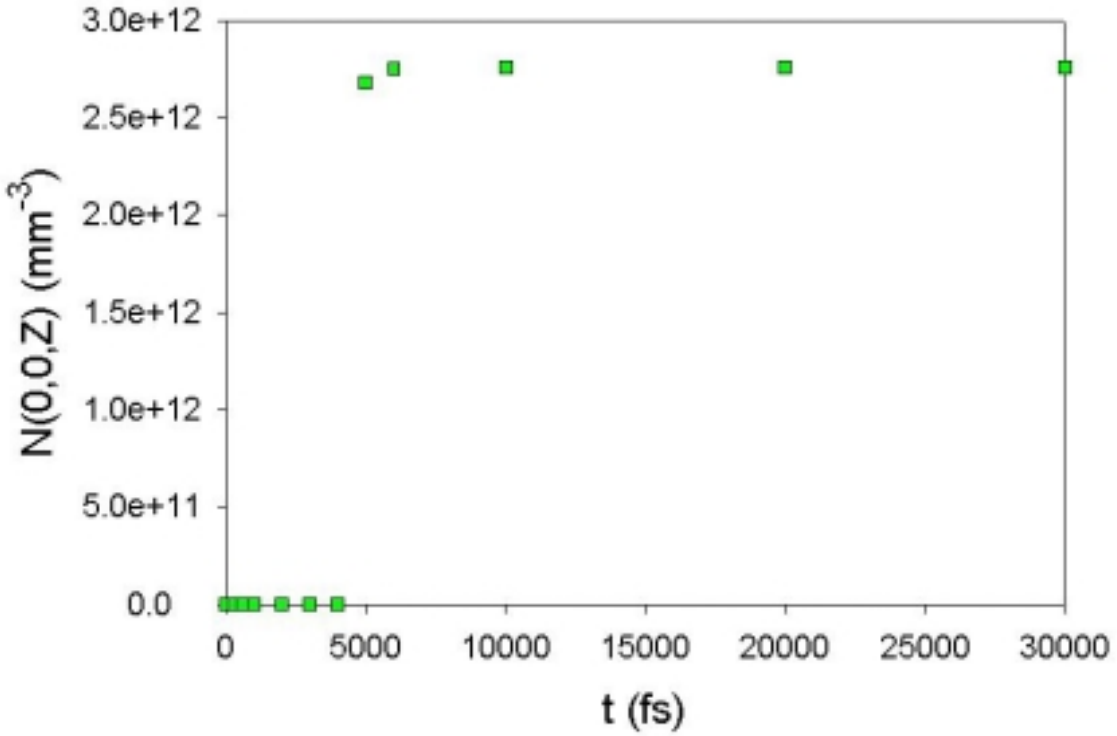

Fig. 36: The time evolution of photon number on the z-axis at z=1.0mm. The total tracked number of photons was kept the same in all results and given by $N_0 = 3.8\times10^8$. The tissue configuration is the same as Fig. 34. The simulations were performed on SGI Origin 2000 computer.

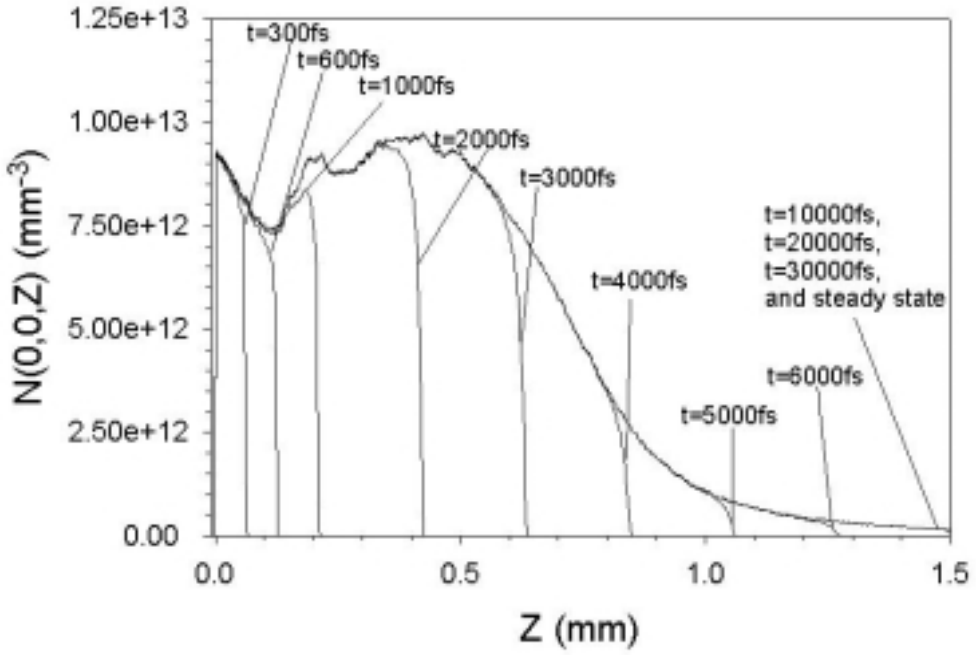

Fig. 37: The time-resolved distribution of photon density N along the z-axis in a linear plot for different time point after the photon is injected at a constant rate starting from t=0fs. The total tracked number of photons was kept the same in all results and given by $N_0 = 3.8\times10^8$. The configuration for tissue layers is $\mu_s = 6mm^{-1}$, $\mu_a = 5.0mm^{-1}$, g = 0.9 and n=1.45 for the epidermis layer, and $\mu_s = 4mm^{-1}$, $\mu_a = 0.5mm^{-1}$, g = 0.9 and n=1.41 for the dermis layer. The simulations were performed on SGI Origin 2000 computer.

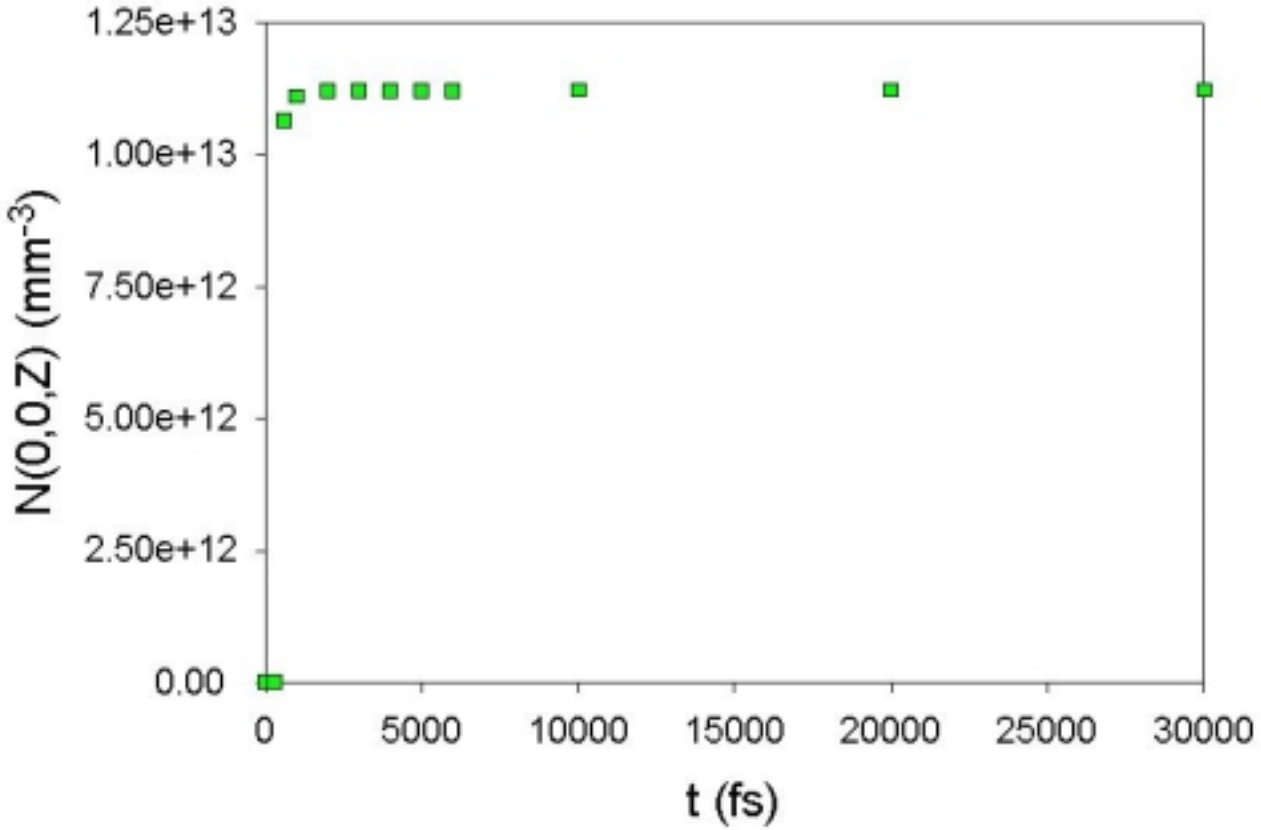

Fig. 38: The time evolution of photon number on the z-axis at z=0.1mm, where the epidermis-dermis junction is located. The total tracked number of photons was kept the same in all results and given by $N_0 = 3.8\times10^8$. The tissue configuration is the same as Fig. 37. The simulations were performed on SGI Origin 2000 computer..

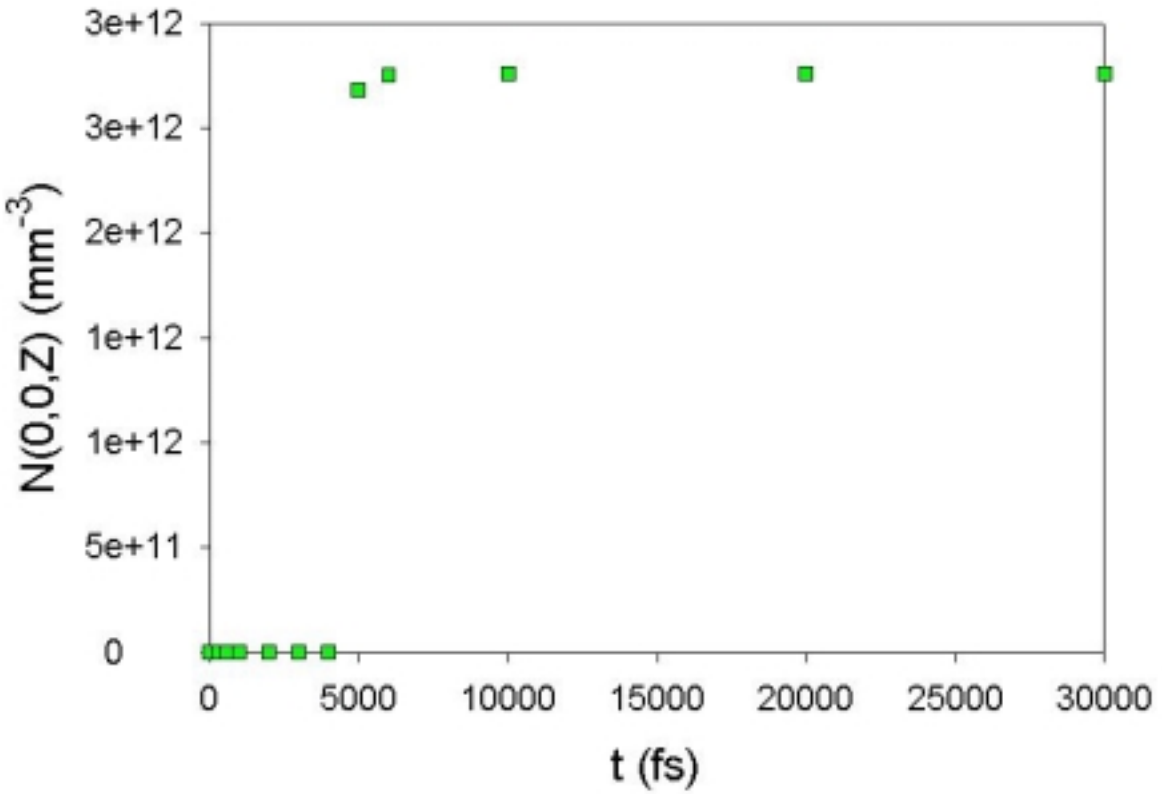

Fig. 39: The time evolution of photon number on the z-axis at z=1.0mm. The total tracked number of photons was kept the same in all results and given by $N_0 = 3.8\times10^8$. The tissue configuration is the same as Fig. 37. The simulations were performed on SGI Origin 2000 computer.

Table 1: The comparison of execution time and standard deviation of the different random number generators selected from Numerical Recipe and IMSL commercial library.

RNG	Type	Execution Time (s)	Period	Sample Number	Standard Deviation
Ran0()	LCG	125	$2.1x10^{9}$	10^{8}	9.949783866999322
Ran1()	LCG	113	$2.1x10^{9}$	10^{8}	9.955107031067019
Ran2()	LCG	184	$2.3x10^{18}$	10^{8}	10.184392667213890
Ran3()	-	141	-	10^{8}	10.195487531256170
Ran4()	LFG	299	-	10^{8}	11.576109363685190
IMSL	LCG	135	$2^{31}-1$	10^{8}	9.942529054521289

References

1. Anderson, R., and Hu, J., "Optical Radiation Transfer in the Human Skin and Applications in *in vivo* remittance spectroscopy," in *Bioengineering & the Skin*, ed. by Marks, R., and Payne, P. A., MTP Press, 253-265 (1981).
2. Anthony, C. and Thibodeau, G., *Anatomy & Physiology*, The C. V. Mosby Company, 76-85 (1983).
3. Chandrasekhar, S., *Radiative Transfer*, Oxford University Press, London (1950).
4. de Buffon, G. C., "Essai d'arithmetique morale," Supplement a l' Histoire Naturelle, Vol. 4, (1777).
5. de Laplace, M. P., "Theorie Analytique des Probabilites," Livre 2, in *Oeuvres Completes de Laplace*, de L'Academie des Sciences, Vol.7, part 2, 365-366 (1886).
6. Dong, K., Song, Z., Hu, X. H. and Lu, J. Q., "Monte Carlo Simulation of Converging Laser Beams Propagating in Skin Tissue Phantoms," Vol. 3590, SPIE Proceeding, being published (1999).
7. Dym, H. and McKean, H. P., *Gaussian Process, Function Theory, and the Inverse Spectral Problem*, Academic Press, 71-74 (1976).
8. Fisherman, G. S., *Monte Carlo: Concepts, Algorithms and Applications*, Springer-Verlag, (1996).
9. Forster, R. A. and Godfrey, T. N. K., "MCNP-A General Monte Carlo Code for Neutron and Photon Transport," in *Methods and Applications in Neutronics,*

Photonics and Statistical Physics, ed. By Alcouffe, R., Dautray, R., Forster, A., Ledanois, G. and Mercier, B., Springer-Verlag, 33-47 (1983).

10. Garcia, N., and Stoll, E., "Monte Carlo calculation for electromagnetic wave scattering from random rough surfaces," Phys. Rev. Lett., Vol. 52, 1798-1801 (1984).
11. Gardner, C. M., Jacques, S. L. and Welch, A. J., "Light Transport in Tissue: Accurate Expressions for One-Dimensional Fluence Rate and Escape Function Based Upon Monte Carlo Simulation," *Lasers in Surgery and Medicine*, Vol. 18, 129-138 (1996).
12. Golomb, S. W., *Shift Register Sequences*, Holden-Day, (1967)
13. Graaff, R., Dassel, A. C. M., Koelink, M. H., de Mul, F. F. M., Aarnoudse, J. G. and Zijlstra, W. G., "Optical properties of human dermis *in vitro* and *in vivo*," *Appl. Opt.*, Vol. 32, 435-447 (1993).
14. Guttorp, P., *Stochastic Modeling of Scientific Data*, Chapman & Hall, 5-12, 282-283 (1995).
15. Hammond, B. L., Lester, W. A., Reynolds, P. J., *Monte Carlo Methods in Ab Initio Quantum Chemistry*, World Scientific, (1994).
16. Henyey, L. G. and Greenstein, J. L., "Diffuse radiation in the galaxy," *Astroph. J.*, Vol. 93, 70-83 (1941).
17. Hu, X. H., "Efficient use of Q-switched lasers in the treatment of cutaneous lesions," in *Lasers in Surgery: Advanced Characterization, Therapeutics, and Systems V*, ed. by R. R Anderson, *SPIE Proceedings*, Vol. 2395, 586-591 (1995).
18. Ishimaru, A., *Wave Propagation and Scattering in Random Media*, Vol. 1, Academic Press (1978).

19. Jackson, D. J., *Classical Electrodynamics (Second Edition)*, John Wiley & Sons, (1975).

20. Jacques, S.L., "Time Resolved Propagation of Ultrashort Laser Pulses within Turbid Tissues," *Appl. Opt.*, Vol. 28, 2223 (1989).

21. Jenkins, F. A. and White, H. E., *Fundamentals of Optics*, McGraw-Hill, (1976).

22. Johnson, C.C., "Optical diffusion in blood," *IEEE Trans. Biomed. Engineer.*, Vol. 17, 129 (1970).

23. Kalos, M. H. and Whitlock, P. A., Monte Carlo Methods, Vol. 1, John Wiley & Sons (1986).

24. Keijzer, M., Jacques, S. T., Prahl, S. A. and Welch, A. J., "Light distributions in artery tissue: Monte Carlo simulations for finite-diameter laser beams," *Lasers Surg. Med.*, Vol. 9, 148-154 (1989).

25. Lord Kelvin, "Nineteenth Century Clouds Over the Dynamical Theory of Heat and Light," *Phil. Mag.*, Series 6, Vol. 2, 1, (1901).

26. Kendall, M., and Stuart, A., and Keith, J., *Kendall's Advanced Theory of Statistics*, Oxford University Press, 308-309 (1987).

27. Knuth, D. E., *The Art of Computer Programming Vol. 2: Seminumerical Methods (Third Edition)*, Addison-Wesley: Reading, (1998).

28. Kulkarni, V. G., *Modeling and Analysis of Stochastic Systems*, Chapman & Hall, 7-11 (1995).

29. Lewis, T. G. and Payne, W. H., "Generalized Feedback Shift Register Pseudo-random Number Algorithms," *Journal of the ACM*, Vol. 20, 456-468, (1973).

30. Lehmer, D.H., “Mathematical Methods in Large-scale Computing Units,” in *Proc. 2nd Symposium on Large Scale Digital Calculating Machinery*, Harvard University Press, 141-146 (1949).
31. Lu, J. Q., Hu, X. H., Song, Z. and Dong, K., “Simulation of Light Scattering in Biological Tissues: the Coherent Component,” Vol. 3601, SPIE Proceeding, being published (1999).
32. Maradudin, A., Michel, T., McGurn, A., Mendez, E., “Enhanced backscattering of light from a random grating,” Ann. Phys., Vol. 203, 255-307 (1990)
33. Marchesini, R., Clemente, C., Pignoli, E. and Brambilla E., “Optical Properties *of in vitro* Epidermis and Their Possible Relationship with Optical Properties of *in vivo* Skin,” *J. Photonchem. Photobiol. B.: Biol*, Vol. 16, 127-140 (1992).
34. Marsaglia, G., “Generating exponential random variables,” *Ann. Math. Stat.*, Vol. 32, 899-900 (1961).
35. Marsaglia, G., “A Current View of Random Number Generators,” in *Computing Science and Statistics: Proceedings of the XVIth Symposium on the Interface*, 3-10, (1985).
36. Metropolis, N. and Ulam, S., “The Monte Carlo Method, ” *J. Am. Statistical Association*, Vol. 44, 335-341 (1949).
37. Metropolis, N., “The beginning of the Monte Carlo method, ” *Los Alamos Science*, Vol. 15, 1987.

38. Miller, I. D. and Veitch A. R., “Optical Modeling of Light Distributions in Skin Tissue Following Laser Irradiation, ” *Lasers in Surgery and Medicine,* Vol. 13, 565-571 (1993).

39. Moschella, S. L., and Hurley, H. J., *Dermatology*, W. B. Saunders Company, 16-17 (1992).

40. Ostle, B. and Mensing, R. W., *Statistics in Research (Third Edition)*, The Iowa State University Press, 27-45 (1945).

41. Press, W. H., Teukolsky, S. A., Vertterling, W. T. and Flannery, B. P., *Numerical Recipes in FORTRAN (Second Edition)*, Cambridge University Press, (1992).

42. Lord Rayleigh, “On James Bernoulli's Theorem in Probabilities,” *Philosophical Magazine*, Vol. 47, 246-251 (1899).

43. Schatzlein, A. and Cevc, G., “Non-uniform cellular packing of the stratum corneum and permeability barrier function of intact skin: a high-resolution confocal laser scanning microscopy study using highly deformable vesicles (Transfersomes), ” *British Journal of Dermatology*, Vol. 138**,** 583-92 (1998).

44. Schmitt, J. M., Zhou G. X. and Walker E. C., “Multilayer Model of Photon Diffusion in Skin,” *J. Opt. Soc. Am. A.*, Vol. 7, 2141-2153 (1990).

45. Song, Z., Dong, K., Hu, X. H. and Lu, J. Q., “Monte Carlo Simulation of Converging Laser Beams Propagating in Biological Materials,” *Applied Optics*, Vol. 38, 2944-2949 (1999).

46. Stanley, W. D., Dougherty, G. R. and Dougherty, R., *Digital Signal Processing (Second Edition)*, Reston, (1984).

47. Stone, H. S., *High-Performance Computer Architecture*, Addison-Wesley, (1987).

48. Tausworthe, "Random Numbers Generated by Linear Recurrence Modulo Two," *Math. Comp.*, Vol. 19, 201 (1965).

49. Tran, P. and Maradudin, A., "Scattering of a scalar beam from a two-dimensional randomly rough hard wall: enhanced backscattering," *Phys. Rev. B.*, Vol. 45, 3936-3939 (1992).

50. Tran, P. and Maradudin, A., "Scattering of a scalar beam from a two-dimensional randomly rough hard wall: Dirichlet and Neumann boundary conditions," *Applied Optics*, Vol. 32, No. 15, 2848-2851 (1993).

51. Tran, P. and Maradudin, A., "Electromagnetic scattering from a two-dimensional randomly rough, perfectly conducting surface: iterative methods," *J. Opt. Soc. Am. A.*, Vol. 11, No. 5, 1686-1689 (1994).

52. Ulam, S., Richtmeyer, R. D. and von Neumann, J., "Statistical methods in neutron diffusion," LAMS-551, Los Alamos National Laboratory, (1947).

53. van Gemert, M.J.C., Jacque, S.L., Sterenborg, H.J.C.M. and Star, W.M., "Skin optics," *IEEE Trans. Biomed. Eng.*, Vol. 36, 1146-1154 (1989).

54. Wan, S., Anderson, R. R. and Parrish, J. A., "Analytical Modeling for the Optical Properties for the Skin with *in vitro* and *in vivo* Applications," *Photochem. Photobiol.* , Vol. 34, 493-499 (1981).

55. Wang, L. H., Jacques, S.L. and Zheng, L.Q., "MCML - Monte Carlo modeling of light transport in multi-layered tissues," *Comp. Meth. Prog. Biomed.*, Vol. 47, 131-146 (1995).

56. Wang, L. H., Jacques, S.L. and Zheng, L.Q., “CONV - Convolution for responses to a finite diameter photon beam incident on multi-layed tissues,” *Comp. Meth. Prog. Biomed*., Vol. 54, 141-150 (1997).

57. Wilson, B. C. and Adams, G., “A Monte carlo model for the absorption and flux distributions of light in tissue,” *Med. Phys*., Vol. 10, 824-830 (1983).

58. Yoon, G., Welch, A. J., Motamedi, M. and van Gemert, M. C. J., “Development and Application of Three-Dimensional Light Distribution Model for Laser Irradiated Tissue,” *IEEE Journal of Quantum Electronics*, Vol QE-23(10), 1721-1733 (1987).

Appendix A: Flow Chart for Single Layer Skin Model

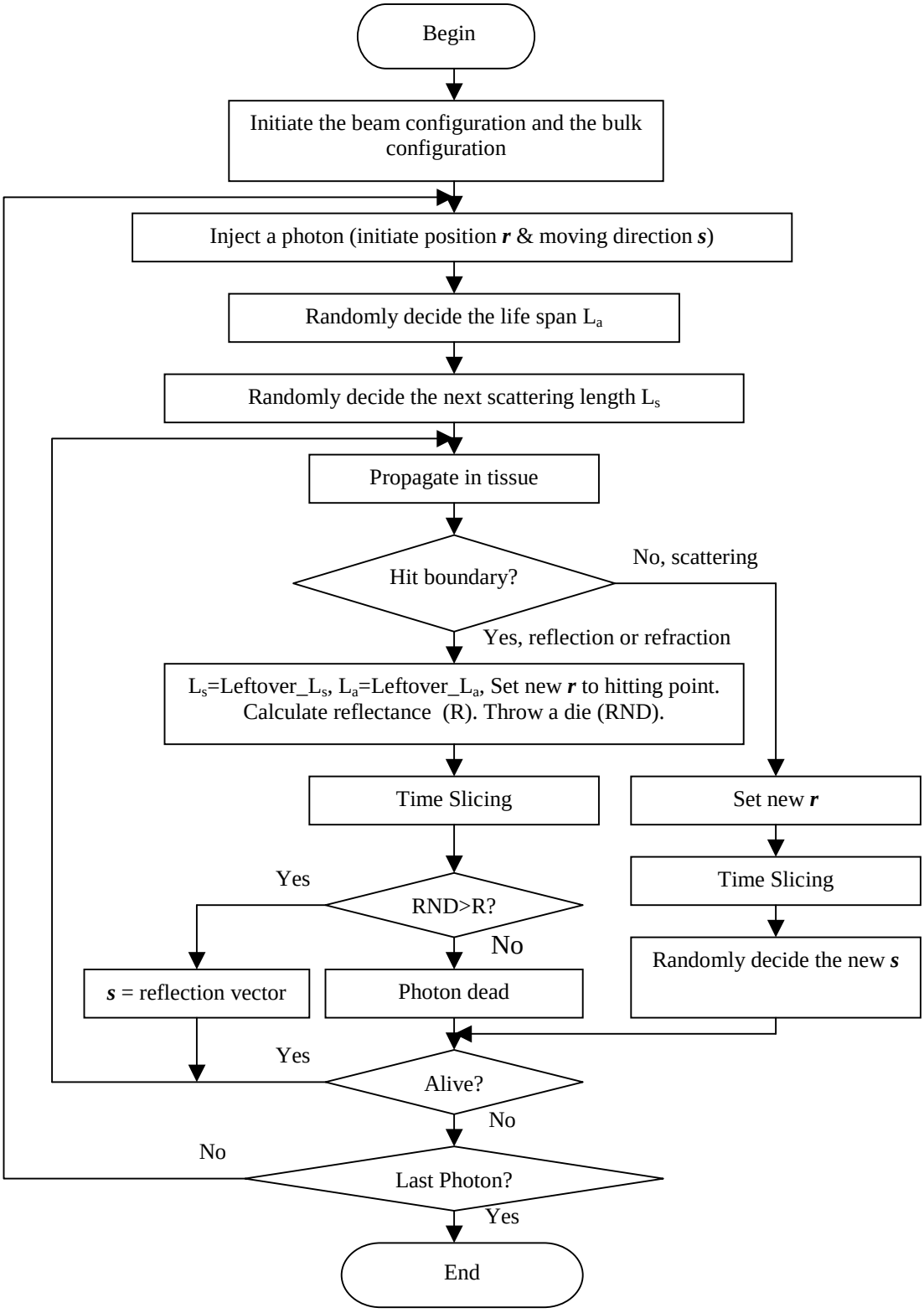

Appendix B: Flow Chart for Multi-layer Skin Model